



POLITECNICO DI TORINO

Master degree in Energy and Nuclear Engineering

Master degree thesis

**Characterization
of a proton beam delivery line
with Monte Carlo simulation**

Supervisors

Prof. Gianni COPPA (DET)

Dr. Faiza BOURHALEB (I-See Computing s.r.l.)

Candidate

Domenico NICOTRA

ACADEMIC YEAR 2017-2018

*Alla mia famiglia,
Mauro, Anna, Simone
A Domenico N.
(1919-2006)*

Sommario

Sin dalla fine dell'Ottocento, l'applicazione di radiazioni in ambito medico è stata studiata costantemente, portando ai giorni nostri alla sua diversificazione in varie discipline. Una tra le più promettenti pratiche radioterapiche è la *protonterapia*. Questo lavoro vuole mettere in luce i vari aspetti fisici legati all'applicazione dei protoni in campo clinico e l'uso di codici di calcolo Monte Carlo per la definizione della distribuzione di dose nella regione di trattamento.

Attraverso il codice Geant4, si utilizza il modello della linea di trasporto protoni del *CNAO*(Centro Nazionale di Adroterapia Oncologica), per paragonare i diversi profili di dose per varie tipologie di particelle. Infine si procede con la generazione di due database con i profili di deposizione di dose relativi a due diverse configurazioni del fascio, utili per la definizione dei piani di trattamento per la protonterapia.

Abstract

Since the end of nineteenth century, radiation application in medical field has been studied, leading now to its diversification in various branches. One of them is the *Proton therapy*, important for its diffusion and relevant results.

This work highlights the various physical aspects associated with the use of proton beams in medical field, and studies the Monte Carlo methodology for the definition of dose distribution inside the treated volume.

By means of Geant4 code, the CNAO proton beam line model is used to compare different dose profiles for various particle species. Finally, this work proceeds with the generation of two databases of dose depositions relative to two different beam configurations. These data sets are useful for the proton therapy treatment planning system.

Acknowledgements

It is very important for me, to express with only few words my best appreciation for the collaboration and the teachings of Dr. Bourhaleb, that with kindness, helped me in the realization of this work.

Furthermore I want to refer my acknowledgements to Prof. Coppa, and to all the teaching staff of DENERG for the great life lessons taught me and experienced in these years.

A special "thanks" goes to the research group of LNS-INFN of Catania, for the opportunity to attend the *V International Geant4 School*.

At last, but not least, my truly and lovely greetings go to my family, that no matter what happens gives me the best support to build my own life.

Contents

List of Tables	7
List of Figures	8
1 Introduction	13
1.1 Historical evolution of radiation application	13
2 Particle therapy	17
2.1 Scope of particle therapy	17
2.2 Ionizing radiation classification	22
2.3 Energy deposition profile	25
2.4 Dose delivery techniques	28
2.5 Transport equation for proton therapy	29
2.6 The Fokker-Planck approximation	30
2.7 Stopping power theory	31
3 Monte Carlo Simulations	35
3.1 Deterministic Model Vs Monte Carlo method	37
3.2 Sampling: Composition method	39
3.2.1 Example: Composition method for protons beam	40
3.2.2 Combination of Rejection and Composition methods	40
3.2.3 MC Error	41
3.3 Code <i>GEANT4</i>	42
3.4 Geant 4 Simulations	45
3.4.1 Applications of DataGen-iSee	50
3.4.2 Energy deposition profile	51
3.5 Protons Vs Heavy ions	56

3.6	Dose profiles superposition	59
4	Monte Carlo databases for proton therapy	61
4.1	Database for Proton therapy	64
4.2	Database with original settings	66
4.2.1	Dependence Energy-Computational time	72
4.3	Database without <i>Ripple filter</i>	73
4.4	The role of a <i>Ripple Filter</i>	77
5	Discussion and Conclusions	81
A	Superposition of dose distributions	89
B	Fluence	91
C	Database with Ripple Filter	93
C.0.1	Profiles and projections for 70MeV proton beam	93
C.0.2	Profiles and projections for 250MeV proton beam	96

List of Tables

2.1	Classification of damages and interactions radiation-biological matter; [15]	18
2.2	Example of particles classification[7]	23
3.1	Table with the components described in the MC model, with dimensions and relative constituent materials	46
3.2	Simulations used for the demonstration of the superposition principle	59
4.1	Depth-Dose database for the water equivalent system	66
4.2	Depth-dose database, for the water equivalent system in the set-up without the RF	74

List of Figures

1.1	Radioactive cosmetics advertising, from Curie Museum of Paris; (Image courtesy of G.Coppa)	13
2.1	Classification of cancer treatments and particles for radiotherapy . .	18
2.2	Damages from radiation interactions[32]	20
2.3	Time scale of radiation damages [23]	20
2.4	Example of response curves for tumour control probability and healthy tissue damage probability	21
2.5	High LET Vs Low LET particles in damages density at DNA scale [17]	23
2.6	RBE definition; (red)= ion curve, (blue)=X-rays curve[28]	24
2.7	Qualitative comparison in dose deposition profiles of High-LET and Low-LET particles (adapted from [34])	24
2.8	Energy deposition profiles for Proton beams simulated by <i>GEANT4</i> with 10^4 events.	26
2.9	Energy deposition profiles for carbon ions beams simulated by <i>GEANT4</i> with 500 events.	26
2.10	1D energy deposition for $160MeV$ protons beams simulated by <i>GEANT4</i> with 10^5 events	27
2.11	2D energy deposition for $160MeV$ protons beams simulated by <i>GEANT4</i> with 10^5 events	27
2.12	Scheme of the two dose delivery techniques, <i>Passive scattering</i> and <i>Active scattering</i> [3]	28
2.13	Protons interactions phenomena: (a) Energy loss for elastic Coulomb scattering. (b) Deviation of protons due repulsive Coulomb force. (c) Non elastic nuclear interaction. [2]	33
2.14	Stopping power of liquid water in function of proton energy[25] . . .	34

3.1	Scheme of the MC method	35
3.2	MC method[18]	36
3.3	Probabilistic(on the right) Vs Deterministic model(on the left) (adopted from[18])	38
3.4	Geant4 hierarchycal subdivision	42
3.5	Succession order of Geant4 tracking	44
3.6	Detector model from Geant4 simulation	45
3.7	Position of CNAO beams components[30]	47
3.8	3D view of CNAO passive scattered dose delivery device[30]	47
3.9	Section and parameters of the ripple filter of CNAO proton beam line [3]	48
3.10	Water phantom test apparatus at LNS-INFN CT	48
3.11	Source position distribution	49
3.12	Summary of preliminary simulations	51
3.13	1D proton energy deposition pdf (10^4 particles simulated).	52
3.14	1D proton energy deposition profile, (10^4 particles simulated).	52
3.15	2D protons energy deposition ($E = 100MeV$, 10^5 particles simulated).	53
3.16	2D proton energy deposition, ($E = 250MeV$, 10^5 particles simulated.)	53
3.17	Projection of Energy deposition on x axis @20mm 100MeV protons, in the plateau region.	54
3.18	Projection of Energy deposition on x axis @69mm(Bragg Peak) 100MeV protons.	54
3.19	Projection of Energy deposition on x axis @90mm 250MeV protons, in the plateau region.	55
3.20	Projection of Energy deportation on x axis @366.04mm(Bragg Peak) 250MeV proton.	55
3.21	Energy deposition profiles comparison between heavy particles beams and protons ones at $70MeV/(u.m.)$	57
3.22	Energy deposition profiles comparison between heavy particles beams and protons ones at $250MeV/(u.m.)$	57
3.23	MC simulations relative error function of the number of events	58
3.24	1D dose distribution for the superposition of protons beams at $100MeV$, $140MeV$ and $160MeV$	60
3.25	2D dose distribution for the superposition of protons beams at $100MeV$, $140MeV$ and $160MeV$	60

4.1	Target volume scheme and representation[8]	62
4.2	Scheme of WET method[2].	63
4.3	Scheme of a SOBP,	65
4.4	Graph of the total dose deposition for all the simulations for the database with the Ripple Filter	68
4.5	Graph of the total particles fluence for the database with the Ripple Filter	69
4.6	Detailed view of the deposition of proton beam with 70MeV, 140MeV, 250MeV, for the database with the Ripple filter	71
4.7	Detailed view of the total particle fluence for the database with the Ripple Filter	71
4.8	Detailed view of the neutron fluence for the database with the Ripple Filter	72
4.9	Dependence of computational time from proton energy (10^5 events)	73
4.10	1D dose deposition distribution for 70MeV and 120MeV proton beam, with and without the Ripple Filter	75
4.11	Graph of the dose deposition for all the simulations from 20–250MeV for the database without the Ripple Filter	76
4.12	2D dose deposition on XZ plane, with the ripple filter	77
4.13	1D dose deposition for 70MeV proton beam, with and without RF	78
4.14	1D dose deposition for 230MeV proton beam, with and without RF	78
4.15	Projection at BP point, for 70MeV proton beam, with and without RF	79
4.16	Projection at BP point for 230MeV proton beam, with and without RF	79
4.17	Scheme of a SOBP with (right) and without (left) Ripple Filter[3]	80
5.1	Bragg Peak energy deposition as function of the beam energy for both set-ups, with and without RF	82
5.2	Difference ($\sigma_{xyBP1} - \sigma_{xyBP2}$) of the Gaussian fit as function of the beam energy	83
5.3	1D dose distribution with doubled error-bars for 100MeV proton beam, for 10k and 100k particles	84
5.4	1D dose distribution with doubled error-bars for 160MeV proton beam, for 5k and 100k particles	85

5.5	1D dose distribution with doubled error-bars for $250MeV$ proton beam, for 10k and 100k particles	85
-----	---	----

Chapter 1

Introduction

1.1 Historical evolution of radiation application

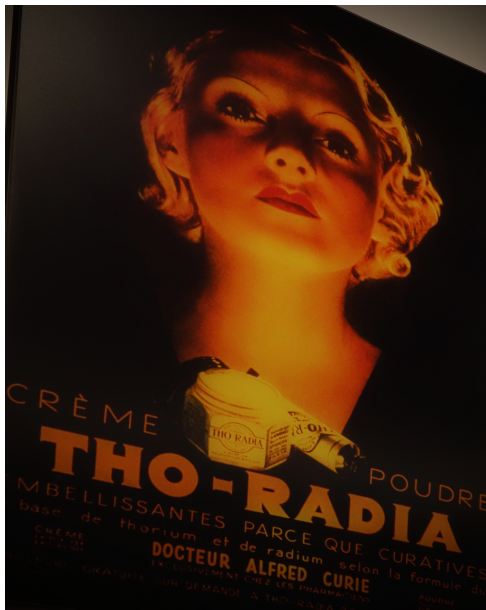


Figure 1.1: Radioactive cosmetics advertising, from Curie Museum of Paris; (Image courtesy of G.Coppa)

Since the last decade of the nineteenth century, during the discovery of *X-Rays* by W.Roentgen, scientists noticed inflammation effects and damages on skin after a prolonged exposure to radiations. Then, by mean the studies of Emil Grubbe, Leopold Freund and Eduard Schiff the idea of a medical use of *X-rays* was born. In the meanwhile Niels Finsen underwent to investigation, the effects of *X-rays*, and *UV-rays*, on human skin, concluding that they could have therapeutic effects, founding in this way the *phototherapy*[15].

This pioneering age continued with the discovery of Radium radioactivity, by Marie Curie, and its use on lupus, trying many methods of applications.

Unfortunately this period was also characterized by a misusing of the word "radioactive" in an advertising way for commercialization purpose: e.g. activated water, radioactive cosmetics and so on.

From the beginning, historical evolution of radiation application was made basically by a direct testing method, without any further investigation or deep understanding of physical and biological phenomena involved.

Finally, after 1935, research took the right direction with the *Coutard method*, of fractionated *X-ray* dose administration, and the use of radiated rods in brachytherapy. This period was called *Orthovoltage era*[15].

In these years there was the birth of the three main methodologies of radiation application in medical field:

- External beam radiation therapy (*EBRT*).
- Brachytherapy or sealed source radiation therapy.
- Systemic radioisotope therapy.

This division is related to the position of radiation source (external or internal to human body), and the extension of the treated volume. Each of these has been developed until nowadays, becoming now consolidated treatments.

This multidisciplinary and interdisciplinary evolution gave birth to a new branch of physics: *medical physics*, involving many different figures, like engineers, physicists, physicians, technicians and so on.

The next important period, from 1950, was called *Mega Voltage era*[15], characterized by a huge research on innovative radio-therapeutic procedures, in order to treat deeply located tumours, with the introduction of γ - ^{60}Co in teletherapy. Since those years radiotherapy was recognised as a medical discipline.

The continuous developing of photon-therapy, in the '70s-'80s, was sided by the introduction of proton therapy, with new devices for dose delivery. In the late 1970s, computer-assisted accelerators were successfully applied on oncology treatments.

After that, the research was never stopped, but it was extended including new tools: in the '90s, more computing power was available, allowing the adoption of a 3D conformal radio-therapeutic device. The *stereotactic radiation therapy (SRT)*, is able to reach an high accuracy in dose distribution, together with the adoption of Monte Carlo techniques in treatment planning. In the new millennium, there was the affirmation of *SRT*, especially with the image-driven radiotherapy (*IGRT*),

allowing a continuous replanning and optimization of the treatment.

New approaches in this field were made in the last two decades, with applications of available new technologies and more computing power with high performance GPU based on algorithms for radiotherapy.

Chapter 2

Particle therapy

The expression *Particle Therapy* means using the interactions between ionizing radiations and biological matter, in order to cure oncological illnesses. The word particle refers every kind of charged or uncharged particles, like α , n , p , β , *ions*, etc., used for medical treatments. Ionizing photons, like X – rays and γ – rays, can be also used for the same purpose but their application is well known as the *Conventional Radiation Therapy*.

The Fig.(2.1) shows the many kind of approaches for oncology treatment, and nowadays, with new promising technologies, more opportunities have been improved for cancer and similar syndromes therapy.

Among the various treatments, this work is focused on *External Beam Radiation Therapy*, with its calculation methods. Then an analysis of a proton beam delivery system is performed by mean MC simulations, for the case of the *proton beam therapy*.

Nowadays, *Proton therapy* has been developed and used in a wide range of oncology applications, showing remarkable results. This spreading is due to an easier access to accelerators and dose delivery devices given by a continuous multidisciplinary research.

2.1 Scope of particle therapy

In any material, a ionizing particle loses energy that is deposited inside matter, with a specific distribution for each radiation species and material properties.

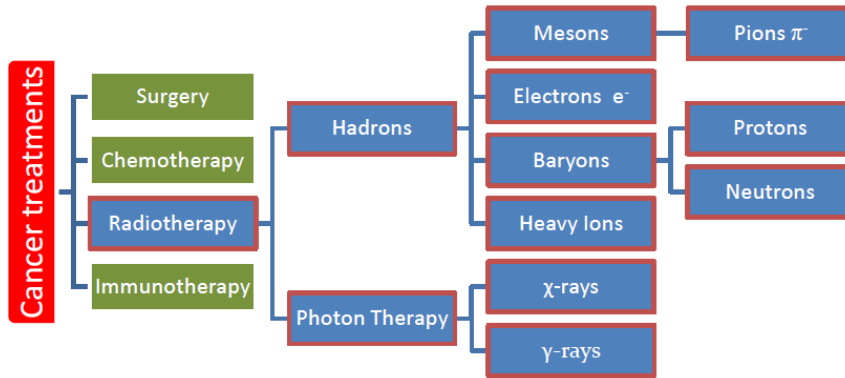


Figure 2.1: Classification of cancer treatments and particles for radiotherapy

The ultimate goal of any kind of therapy is to treat a disease and, in the case of radiation application, the tumour tissue, causing less damage as possible to the healthy one, as *ALARA* principle prescribes.

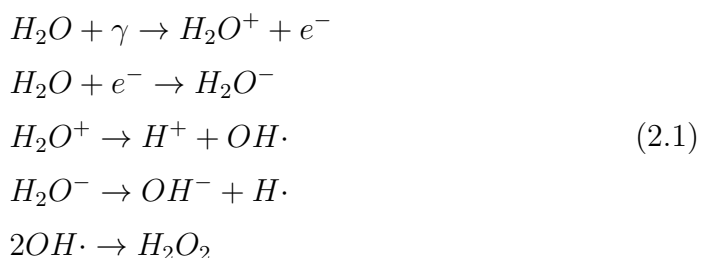
To understand how it is possible to cure a tumour by means of radiations is fundamental to understand the ways in which particles and/or photons interact with biological matter. In Tab.(2.1) the main effects are listed.

Type of effects	Consequences
Physical	transfer and absorption of energy
Biophysical	ionization, excitation
Physical-Chemical	direct alterations of atoms and molecules, production of free radicals
Chemical	breaking bonds, polymerization, de-polymerization
Biochemical	molecular alteration
Biochemical-biological	damage to DNA, RNA, cytoplasm, enzymes
Biological	aberrations of cellular components, morph-functional and metabolic lesions, damage to genetic material

Table 2.1: Classification of damages and interactions radiation-biological matter; [15]

As it shown in detail in Tab.(2.1), the effects are many, but all can be classified shortly in two main final consequences[7][10]:

- **Direct damage:** Particles or radiation (and their secondary radiations), in the energy deposition process, can break directly chemical bonds and structures of biological macromolecules and cell DNA. Damages so created can be repairable or irreparable. The last case leads to cell death. The most important outcome is the *Double Strand Breaks-DBS*[10], where the nucleic chain becomes totally and permanently separated. The characteristic time for the ionization of macromolecules is of the order of $\approx 10^{-15}$ [s] instead, the fixation of a DNA-damage takes up to $\approx 10^{-6}$ [s] (see Figures(2.2) and (2.3)).
- **Indirect damage:** Particles or radiations (and their secondary radiations), ionize atoms in cell environment, producing free radicals, highly chemical reactive compounds. Radicals reactions create damages altering cells structures, giving at the end, cellular death. These kinds of damages are widely more frequent than the first ones, but this process has a shorter time scale of about 10^{-6} [s] (see Figures (2.2) and (2.3)).



The reactions of (2.1) are some mechanisms of free radicals production. Those highly reactive compounds, like hydrogen peroxide, or hydroxyl radical are extremely toxic for DNA, and so responsible for the cell death. The effectiveness of the dose deposition on malicious tissues is strongly affected by the hypoxia of the treated domain. Oxygen fixation process makes the damage permanent and unrepairable. Hypoxia causes the decreasing of tumour control probability.

The survival probability of malicious tissue (complementary of the killing probability) can be expressed by the *Linear Quadratic Model-LQ* [4]. The two components of cell killing, according to the classification in Tab.(2.1) are: $\alpha \cdot D$ related to lethal lesions, and $\beta \cdot D^2$ related to potentially lethal damages.

$$-\log(S) = \alpha \cdot D + \beta \cdot D^2
 \tag{2.2}$$

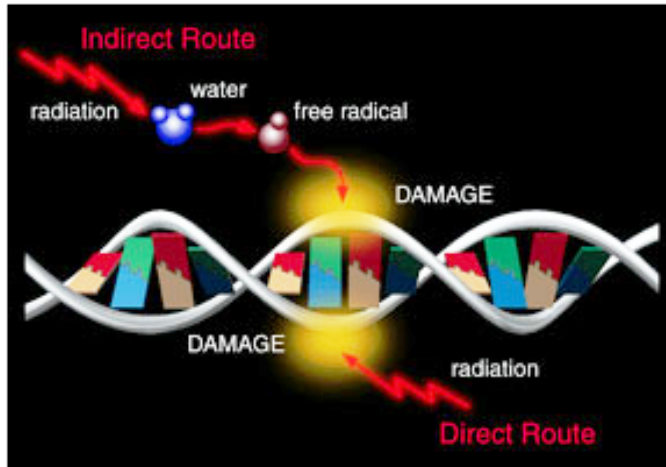


Figure 2.2: Damages from radiation interactions[32]

Radiation physics		Radiation chemistry			Radiation biology		
10 ⁻¹⁵	10 ⁻¹²	10 ⁻⁹	10 ⁻⁶	10 ⁻³	1	10 ³	10 ⁶
sec	sec	sec	sec	sec	sec	sec	sec
•Ionization •Excitation	•Radical formation •Dielectric relaxations		•DNA damage formation			•Repair •Replication •Cell death •Somatic mutations •Cancer •Heritable mutations	

Figure 2.3: Time scale of radiation damages [23]

The main concept of the discipline in object is the *Dose* and its spatial distribution. As it is shown in Eq.(2.3), the dose is defined as the energy absorbed per mass unit, especially on biological matter.

$$D = \frac{d\bar{E}}{dm} = \frac{J}{kg} = [Gy] \quad (2.3)$$

$$E = R_{in} - R_{out} + \sum Q \quad (2.4)$$

$$D = \frac{1}{\rho} \int_0^{\infty} \Phi(E) \cdot \Sigma_a(E) dE \quad (2.5)$$

where $\Sigma_a(E)$ [m^{-1}] is the absorption cross section of medium, ρ [kg/m^3] mass density, and Φ [$particles/m^2s$] is the flux of particles.

The Eq.(2.4) is a balance of energy on the examined volume, taking into account: all the energies of any ionizing particles entering and exiting the volume. The Eq.(2.4) considers also all the variations of the rest mass energy of nuclei and particles in any nuclear transformation that occurs in the domain.

From a general point of view, the dose in a material has a stochastic nature, meaning that for large volumes (and large masses treated), there is a predictable distribution, instead, for little volumes, there is the loss of predictability.

In other words, considering identical irradiations, for large volume (and large mass) E/m ratio results always the same, because the path length across medium becomes comparable with mean free path for radiation interaction.

This concept must be kept into account in the case of medical physics, because the working domain of a tumour tissue is of the order of $10^{-6}m^3$ or less, so the problem of radiation therapy becomes a probabilistic one. For that reason, there are two main stochastic quantities: the *tumour control probability*, TCP and the *normal tissues complications probability*, $NTCP$. In the Fig.(2.4) the characteristic trend of these two quantities is shown.

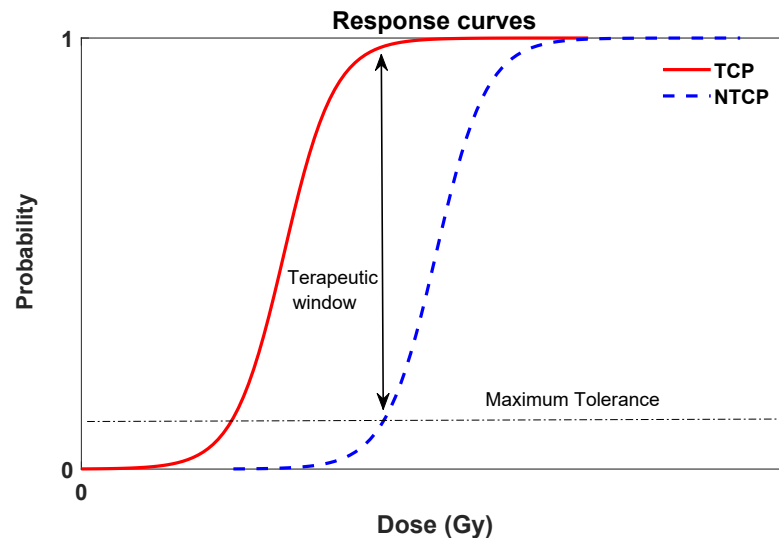


Figure 2.4: Example of response curves for tumour control probability and healthy tissue damage probability

2.2 Ionizing radiation classification

Dose delivery can be done by means of particles and/or photons. A primary distinction between radiations can be done looking the ionization phenomena involved:

- **Directly ionizing radiation** Charged particles deposit their kinetic energy and ionize in one step process, through Coulomb collisions. Some examples are electrons, ions, and the most important for this work, protons.
- **Indirectly ionizing radiation** Neutral particles and photons that deposit their energy, ionize at least, two step process:
 - a charged particle is released in absorber.
 - the released particle deposits energy through Coulomb collisions.

The most important classification can be based on the LET, according to the density of ionization produced in the absorber. LET or Linear Energy Transfer, is the quantity of energy linearly deposited in the stopping medium by the slowing down particle, commonly expressed as

$$LET = \frac{dE}{dx} = \left[\frac{keV}{\mu m} \right] \quad (2.6)$$

Hence the dose is expressed as:

$$D [Gy] = 1.6 \cdot 10^{-10} \cdot \frac{dE}{dx} \left[\frac{keV}{\mu m} \right] \cdot F [m^{-2}] \cdot \frac{1}{\rho} \left[\frac{m^3}{kg} \right] \quad (2.7)$$

With this criteria there are two main categories:

- **Low LET** or sparsely ionizing
- **High LET** or densely ionizing

Here below, a list of radiation used in radiotherapy is shown in Tab.(2.2).

Focusing on the purpose of this work, of High Let particles, like protons, the Fig.(2.5) of various radiation kinds is reported.

High-Let particles, clearly, are the most suitable choice for a medical application. They create a cluster of ionization, increasing the TCP.

Low LET	LET [keV/μm]	High LET	LET [keV/μm]
X-rays 250kVp	2	Electrons 1MeV	12.3
γ-rays ⁶⁰ Co	0.3	Neutrons 14MeV	10
X-rays 3MeV	0.3	Carbon Ions 100MeV	160
Electrons 10keV	2.3	Heavy ions	100-2000

Table 2.2: Example of particles classification[7]

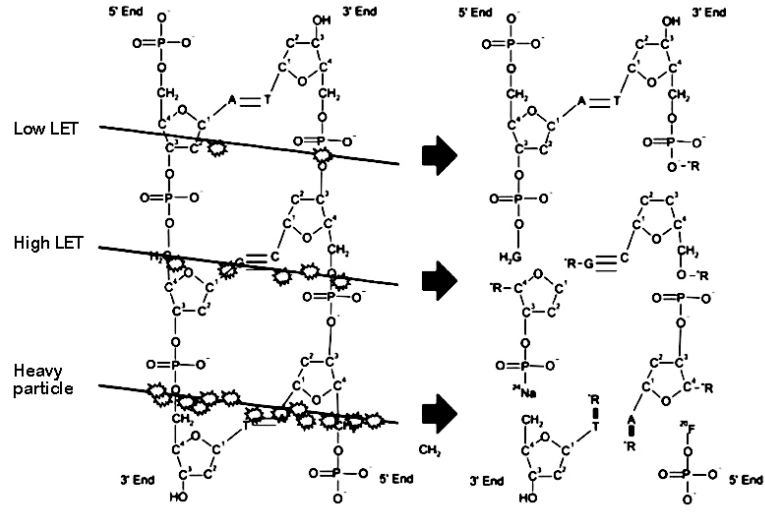


Figure 2.5: High LET Vs Low LET particles in damages density at DNA scale [17]

Each of the previous radiations in Tab.(2.2), has its own efficiency in cell killing. So it is possible to define the *Relative Biological Effectiveness-RBE*[27][28], a parameter that compares deposition of the radiation in exam with a reference one at constant survival rate. The Eq.(2.8), shows the definition for protons, but as well the RBE can be defined for any other ionizing particle. Usually the reference radiations are the X-rays (in Fig.(2.6), the RBE concept is visualized).

$$RBE_p = \left[\frac{D_{X-ray}}{D_p} \right]_{S_x=S_p} \quad (2.8)$$

Proton RBE definition, with *X-ray* dose as reference, $RBE_p \approx 1.1$

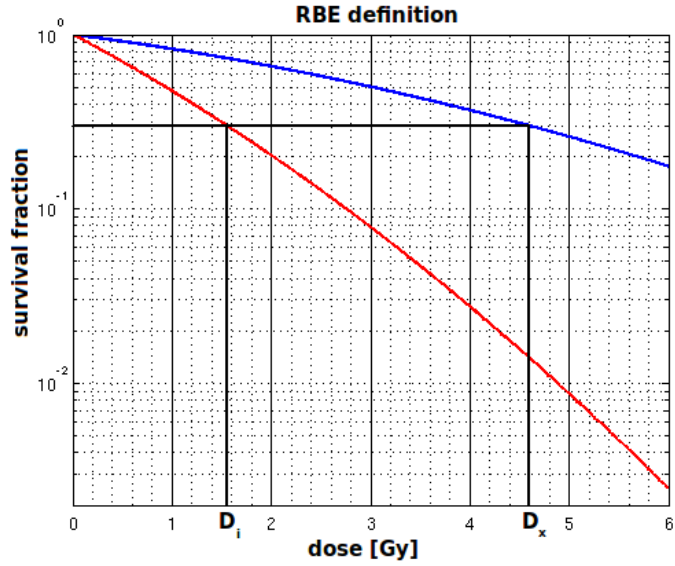


Figure 2.6: RBE definition; (red)= ion curve, (blue)=X-rays curve[28]

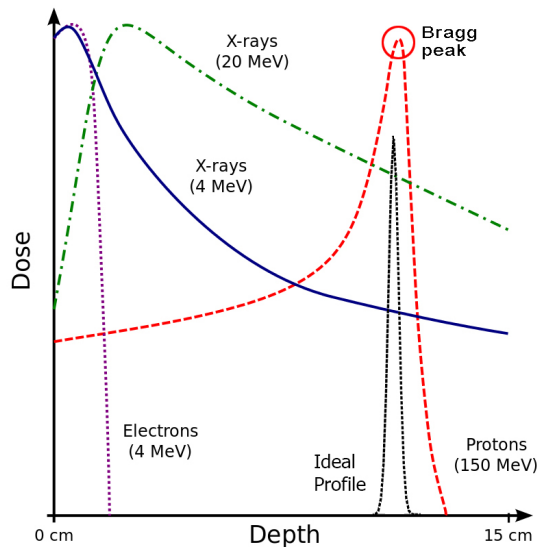


Figure 2.7: Qualitative comparison in dose deposition profiles of High-LET and Low-LET particles (adapted from [34])

2.3 Energy deposition profile

Proceeding with a comparison of the various dose deposition-profiles, the Fig.(2.7), shows a qualitative comparison among different energy deposition curves relatively to the main radiation species. It is noticeable, the proton curve with a peak, called *Bragg peak-BP*, situated at a depth that proportionally depends on the initial energy and medium. Also a similar characteristic profile is shown by heavier particles like carbon, helium and so on. The maximum of deposited energy is caused by many interactions with targeted tissues, due to an increase of the collision cross section with the decreasing of particle speed.

The proton energy deposition is proportional with the inverse of its velocity, so it is also justified the sudden drop of the curve and the stop of particle path (same behaviour for ions).

In Figures (2.8) and (2.9) are reported some examples of energy deposition profiles for protons and carbon ions, with typical values of energy used in medical applications.

Now, pointing out the behaviour of a proton beams, (shown in detail in Fig.(2.11)), there is a symmetric deposition on the planes $X-Z$ and $Y-Z$, due to the exactly collimated beams and the homogeneity of the water phantom (Z axis parallel with beam direction, X and Y are the width and height of water phantom).

On the plane $X - Z$ the profile is symmetrical with respect to the beam axis, (as shown in Fig.(2.11)) and analytically the profile can be modelled in the first approximation, by a Gaussian function, centred on the beam axis, with σ that varies along z axis[24], this aspect will be discussed in the following chapters.

Keeping looking the Fig.(2.11), the area of higher dose, results spreaded in the orthogonal plane to the beam direction. This phenomenon is caused by the *Multiple Coulomb Scattering-MCS* with target nuclei, causing the particle direction deflection, this lateral profile is called *lateral beam spread*.

In proton therapy the lateral profile broadening is very important, because it allows to cover the tumour volume. Spreading is also caused by numerous scattering collisions in materials in front of the patient (beam shaping devices, filters, air...) or also by collisions in interposed tissues between entering and stopping point. The lateral dose deposition, instead, is called *penumbra*.

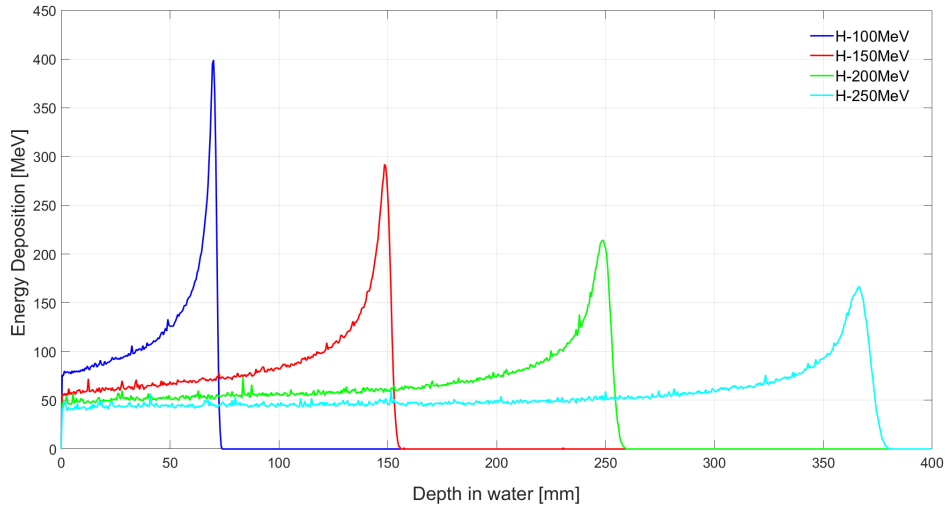


Figure 2.8: Energy deposition profiles for Proton beams simulated by *GEANT4* with 10^4 events.

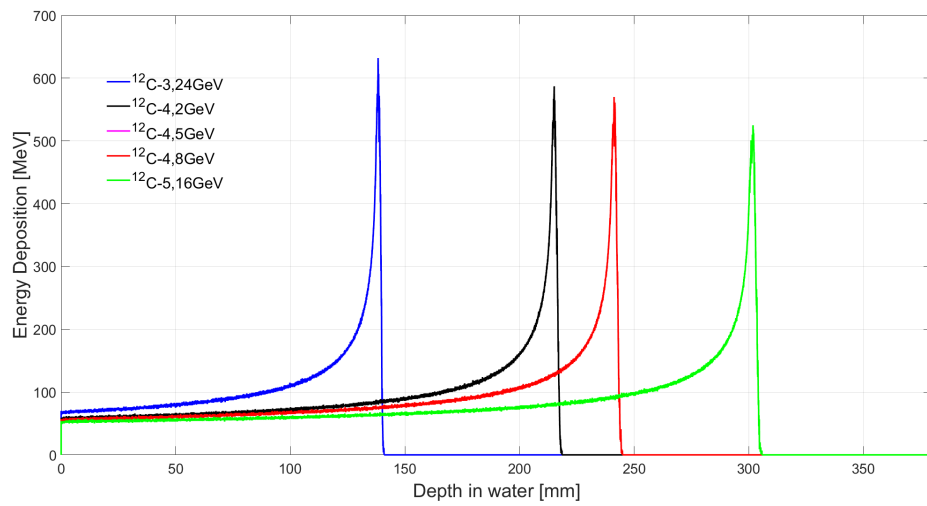


Figure 2.9: Energy deposition profiles for carbon ions beams simulated by *GEANT4* with 500 events.

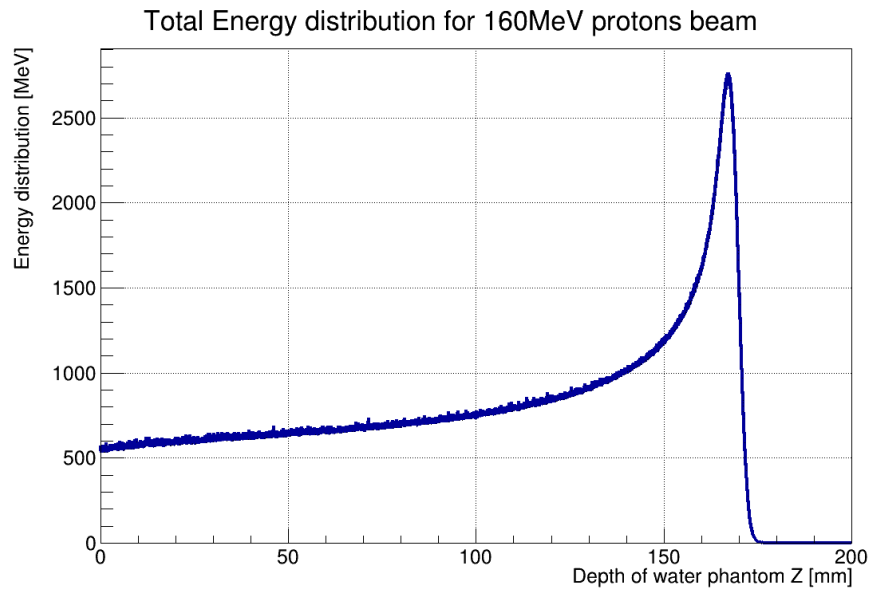


Figure 2.10: 1D energy deposition for 160MeV protons beams simulated by *GEANT4* with 10^5 events

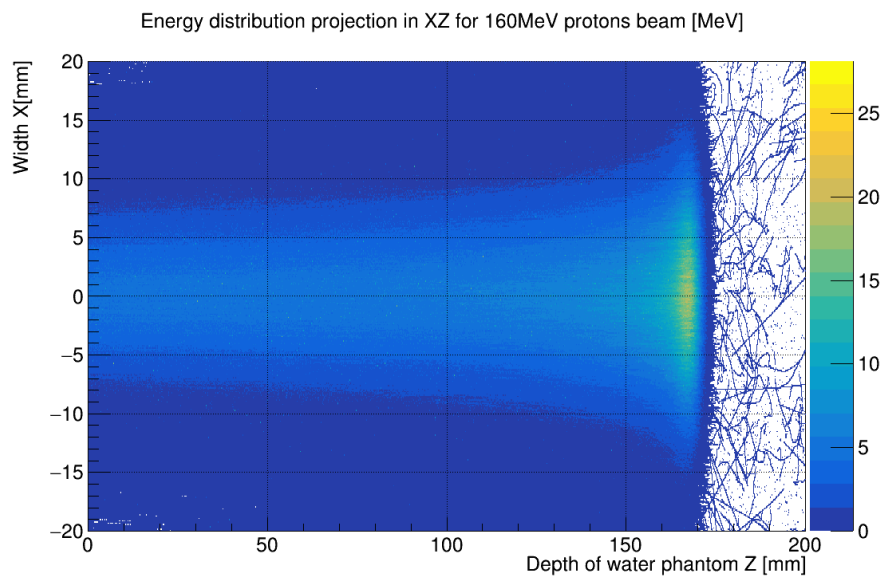


Figure 2.11: 2D energy deposition for 160MeV protons beams simulated by *GEANT4* with 10^5 events

2.4 Dose delivery techniques

Since the proton treatment is a ballistics problem, two different techniques can be used to deliver the exact amount of energy to the treated volume: the *Passive scattering technique*, and the *Active scattering technique*. The passive scattering system uses compensators, collimators and range shifters to reach the 3D dose conformation on the treated volume. Those devices fit a nearly collimated monokinetic particle beam from an accelerator into a 3D shape.

The components of the passive technique are difficult to design, and need continuous adjustments for the various geometry. Passive scattering is largely used for protons and C-ions[3]. This method is used mainly in the case where the particle accelerator is a cyclotron, since the particle energy is not adjustable in this kind of device.

The active technique is instead mostly used with synchrotrons, and linacs. In this case the regulation of the beam energy plays the major role: the depth of the deposition can be changed, the beam profile can be widened and modified by the action of the monitoring magnets to scan the treated volume[3]. In simple words, the system "paints the dose" on the volume. Unfortunately the beam energy regulation can be performed under certain constraints and interval of time. For these reasons, the active system requires scattering devices, like the *Ripple Filter*¹, to minimize the energy regulation.

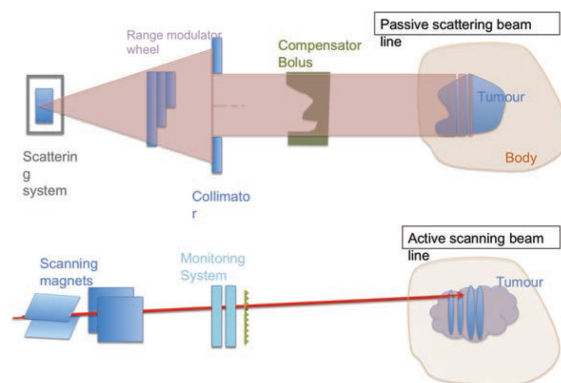


Figure 2.12: Scheme of the two dose delivery techniques, *Passive scattering* and *Active scattering*[3]

¹The Ripple Filter will be described in the following chapters

2.5 Transport equation for proton therapy

The application of a radiation treatment involves a complete and systematic evaluation of fluence and dose distribution in the whole human body. This is necessary to keep the maximum energy deposited under prescribed limits, which are different for each tissue. The Boltzmann Transport theory can be used to calculate these quantities, under the hypothesis of linear diffusion (proton density per unit of target volume of domain is orders of magnitude smaller than nuclear density). Practically, the linear Boltzmann transport equation (*LBTE*) is a pure particle balance in the phase space $(\vec{r}, \hat{\Omega}, E)$, where: $\vec{r} = (x, y, z)$ is the space position, $\hat{\Omega} = (\mu, \eta, \zeta)$ direction, and E is the kinetic energy of the particle.

Hence, with the hypothesis of linear interactions and steady state conditions, in cartesian coordinates, the *LBTE*[16][33][9][11] can be written as:

$$\hat{\Omega} \cdot \vec{\nabla} \Phi(\vec{r}, \hat{\Omega}, E) + \Sigma_{tot}(\vec{r}, E) \Phi(\vec{r}, \hat{\Omega}, E) = Q^{scat}(\vec{r}, \hat{\Omega}, E) + S_{ext}(\vec{r}, \hat{\Omega}, E) \quad (2.9)$$

$$\vec{r} \in V$$

This equation is written in terms of the angular flux (scalar) $\Phi(\vec{r}, \hat{\Omega}, E) = \vec{v} \cdot N(\vec{r}, \hat{\Omega}, E)$, with $N(\vec{r}, \hat{\Omega}, E)$ the angular density. The detailed meanings of the terms in Eq.(2.9) are shown in the following:

- $\hat{\Omega} \cdot \vec{\nabla} \Phi(\vec{r}, \hat{\Omega}, E)$ is the streaming operator. This term quantifies the net number of particles that come in the infinitesimal volume dV through domain border ∂V , with direction and energy which vary in the intervals $(\hat{\Omega} \pm d\hat{\Omega})$, $(E \pm dE)$. It must be highlighted that $j(\vec{r}, \hat{\Omega}, E) = \Phi(\vec{r}, \hat{\Omega}, E) \cdot \hat{\Omega}$ is the angular current. If it is expressed as, $j(\vec{r}, \hat{\Omega}, E) dAdEd\hat{\Omega}$, it represents the average number of particles that go through dA with energy and direction in $(E \pm dE, \hat{\Omega} \pm d\hat{\Omega})$, it is possible to denote that $|j| = \Phi$.
- $\Sigma_{tot}(\vec{r}, E) \Phi(\vec{r}, \hat{\Omega}, E)$ is the removal operator, which takes into account the particles lost by absorption.
 $\Sigma_{tot} = \sigma_t(\vec{r}, E) \cdot N(\vec{r}) = \left[m^2 \cdot \frac{\text{nuclei}}{m^3} \right] = [m^{-1}]$ is the macroscopic total cross section, that represents the probability of interaction between incident particles and target nuclei[11].
- $S_{ext}(\vec{r}, \hat{\Omega}, E)$ is the source of particles contained in V , useful only in the case of brachytherapy, where source is inside the treated domain. In the case of proton therapy, with external beam source, this term is null.

- $Q^{scat}(\vec{r}, \hat{\Omega}, E)$ represents the scattering source. The scattering process can change direction and energy of the particles, thus moving particles in the phase space.

A more exhaustive digression needs to explain the scattering source in Eq.(2.9):

$$Q^{scat}(\vec{r}, \hat{\Omega}, E) = \int_0^\infty dE' \int_{4\pi} \sigma_s(\vec{r}, \hat{\Omega} \cdot \hat{\Omega}', E' \rightarrow E) \Phi(\vec{r}, \hat{\Omega}', E') d\hat{\Omega}' \quad (2.10)$$

where $\sigma_s(\vec{r}, \hat{\Omega} \cdot \hat{\Omega}', E' \rightarrow E)$ is the macroscopic differential scattering cross section[11].

This quantity represents the probability of an incident particle with energy E and direction $\hat{\Omega}$ to change its energy in E' and direction in $\hat{\Omega}'$.

Scattering is the main process for the particle slow down. The term in Eq.(2.9) can be expressed in many ways. Among these the Legendre's polynomials assume an important approximation on the scattering angle, considering only the entering and exiting direction $\mu_0 = \hat{\Omega} \cdot \hat{\Omega}'$. This assumption reproduces very well the behaviour of the particles, but it is not enough for the case of charged ones.

2.6 The Fokker-Planck approximation

The *LBTE* is especially suitable for neutral particles, such as neutrons, but the transport problem need to be adapted in the specific case of charged particles, like protons.

In proton therapy applications, the beam energy range is between $70 - 250 MeV$ [1]. With these values, protons suffer from a small deviation angles during scattering events, with a peaked distribution in the scattering function, (Eq.(2.10)) along the incident direction (with $\mu_0 \approx 1$). Protons, in this energy interval, need a huge amount of interactions for slowing down, so it is meaningful to suppose a continuous slow down process. Under these conditions, and with no source, the *LBTE* can be modified into the following *Boltzmann-Fokker-Planck approximation-BFPTE*: Eq.(2.11) :

$$\begin{aligned} \hat{\Omega} \cdot \vec{\nabla} \Phi(\vec{r}, \hat{\Omega}, E) + \Sigma_{tot}(\vec{r}, E) \Phi(\vec{r}, \hat{\Omega}, E) = & \frac{\alpha}{2} \left(\frac{\partial}{\partial \mu} (1 - \mu^2) \frac{\partial}{\mu} \Phi(\vec{r}, \hat{\Omega}, E) + \right. \\ & \left. + \frac{1}{1 - \mu^2} \frac{\partial^2}{\partial \phi^2} \Phi(\vec{r}, \hat{\Omega}, E) \right) + \frac{\partial}{\partial E} S(\vec{r}, E) \cdot \Phi(\vec{r}, \hat{\Omega}, E) \end{aligned} \quad (2.11)$$

where:

- α is the momentum transfer cross section, (hard to compute). It represents the average angular deflection of the protons per unit travelled distance. This parameter has a strong dependence with the energy of the incident particle.
- The terms ϕ and $\mu = \cos(\theta)$ represent the direction in spherical coordinates (θ the polar angle and ϕ the azimuthal one).
- S represents the stopping power, that corresponds to the quantity of energy lost per unit of path length, dependent on energy and material properties. This quantity needs hard calculation but is available on databases (like "Pstar" of NIST[25]). The trend of the stopping power in liquid water can be seen in Fig.(2.14). This physical quantity plays an important role better discussed in the following section (2.7).

After this brief digression on the main physical model for the particle transport problem, it is clear that the grade of the mathematical model is too high, and also the medium heterogeneity makes it more complex. From a mathematical point of view the problem has 7 dimensions. Even if a discrete approach was possible, the problem would have a too high computational effort also taking into account the interested interval of values.

However, for some physical application the *BFPTE* is still a good but approximate representation of the solution, e.g. large scale problems with known geometry and materials. Unfortunately, for medical applications, the accuracy needed is very high and unreachable with an analytic approach. The difficulties are related to the human body heterogeneity, different tissue dose tolerability, and also some additional complexity related to patient mobility[26].

2.7 Stopping power theory

Considering now a major distinction between photons and charged particles can be considered the most important families of ionizing radiations. They have differences not only on the nature of particles, but also on the interaction mode with matter. The list below describes the interaction phenomena for the main ionizing radiations used in medical field:

-
- **Photons**, like γ -rays, X -rays, are absorbed usually by medium, after occurring a photoelectric effect, or pair production, or as well they can be replaced by their secondary after a Compton scattering event, and travel in a different direction.
 - **Charged particles** are characterized by a much larger cross section, than the photon one, about $10^4 - 10^5$ times greater. Due to the electrical charge, a low energy beam goes to zero almost immediately, for the number of interactions with medium nuclei. Each interaction creates a very light decrease of the initial particle energy. (Averagely the energy lost per interaction is $60[eV]$).

So, for charged particles, in relation to the average energy loss per interaction, it is possible to define the *Stopping Power*, like the mean energy loss per unit of path length. Firstly, it was defined only for α and β but now, it has been extended to every kind of ions.

The Stopping Power depends on the material properties, type and energy of radiation. This quantity is the cumulative result of the major three causes of interaction in matter:

- (a) **Electron Collision Stopping power**, S_e , coming from coulomb interactions between orbital electrons and projected particles.

For protons case, due their larger mass respect to electron one $m_p/m_e \approx 10^3$, the effect of Coulomb interaction is very little, so the energy loss is small for each event, also the trajectory remains almost unperturbed[2]. On the other hand, in the interactions with proximal nuclei, protons experience an *elastic coulomb interaction*, that deviate their velocity and initial trajectory due to the larger mass of nucleus.

- (b) **Radiation Stopping power**, S_r , mainly caused by Bremsstrahlung effect between absorber nuclei and charged particles. This phenomenon gives appreciable energy loss only for light radiations, $\Delta E \propto M^{-2}$, (M mass number).

For proton beam this mechanism is always possible, but in the typical energy range of proton therapy $70 - 250 MeV$, it is a very rare event, and so it can be considered negligible.

- (c) **Nuclear collision stopping power**, S_n , this term depends only on the *Non-elastic* nuclear interaction between projectile and target nuclei. The produced

effect is very important, the projectile enters in a target nucleus, that emits a secondary particle (p, D, T, n) often with a γ photon.

In proton therapy, nuclear collision, although it is rare, but possible, in the therapeutic energy window, the effects can be considered negligible in a first approximation.

The Equations (2.12) and (2.13) describe the concepts:

$$S(E) = \frac{-dE}{dx} = \sum_i N_i \sum_n \Delta E_{ni} \sigma_{ni}; \quad (2.12)$$

$$\begin{aligned} S: \text{Stopping power [J/m]}; & \quad N: \text{nuclear density [m}^{-3}\text{]}; \\ \sigma: \text{cross section [b]} = [10^{-28} \text{m}^2]; & \quad E: \text{particle energy [J]}; \\ \frac{S}{\rho} = \frac{S_e}{\rho} + \frac{S_r}{\rho} + \frac{S_n}{\rho}; & \quad (2.13) \end{aligned}$$

$$\begin{aligned} S/\rho : \text{Mass Stopping} & \quad \rho: \text{mass density [kg/m}^3\text{]}; \\ \text{power [Jm}^2\text{/kg]}; & \end{aligned}$$

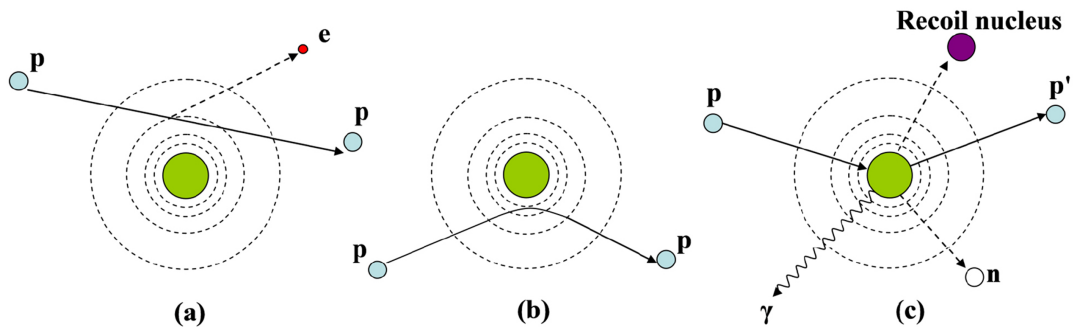


Figure 2.13: Protons interactions phenomena: (a) Energy loss for elastic Coulomb scattering. (b) Deviation of protons due repulsive Coulomb force. (c) Non elastic nuclear interaction. [2]

As reference, the definition of the stopping power, can be explained by two historical approaches:

- *Bohr's approach* founded on the classical physics and based on the impact parameter between particle trajectory and targeted nucleus.
- *Bethe's approach*[19][2] founded on the quantum mechanics, more complete than Bohr's one, based on the quantization of momentum loss from particle

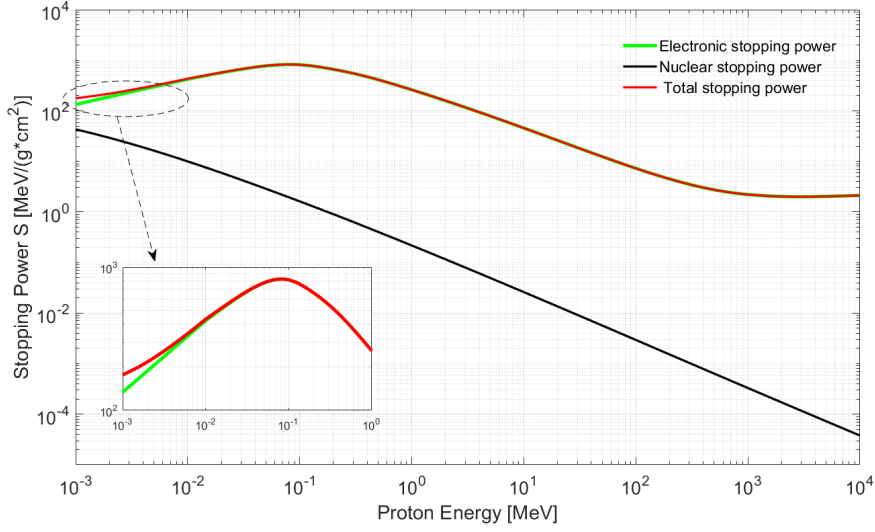


Figure 2.14: Stopping power of liquid water in function of proton energy[25]

to medium. This model is used especially in the calculation of positrons and electrons stopping power, see Eq.(2.14)[2].

$$\frac{S}{\rho} = -\frac{dE}{\rho dx} = 4\pi N_A r_e^2 m_e c^2 \frac{Z z^2}{A \beta^2} \left[\ln \frac{2m_e c^2 \gamma^2 \beta^2}{I} - \beta^2 - \frac{\delta}{2} - \frac{C}{Z} \right] \quad (2.14)$$

N_A : Avogadro's number;	A : Target mass number;	C : shell correction term;
r_e : electron radius;	c : Speed of light;	δ : remote electron density shielding term;
m_e : electron mass	$\beta = \frac{v}{c}$;	I : target average excitation energy;
z : projectile charge	v : projectile speed;	
Z : Target charge	$\gamma = (1 - \beta^2)^{-1/2}$;	

In Eq.(2.14), the two correction terms C and δ , are based on relativistic theory. They are very important in the cases of very high on very low particle energy[2]. It is noticeable that projectile properties (that for this case is proton) rule the phenomena of energy loss (deposition), with no dependence with the particle mass. It is also relevant that the target material play an important role in the energy loss rate due to the product $N_A \rho Z/A$, representative for the electrostatic interactions. Referring now to the case of proton therapy (with $z = 1$), the ratio Z/A can vary from 0,5, for biological tissue(H,C,O as main nuclei), to 0.42 for beam line components made by high-Z materials.

Chapter 3

Monte Carlo Simulations

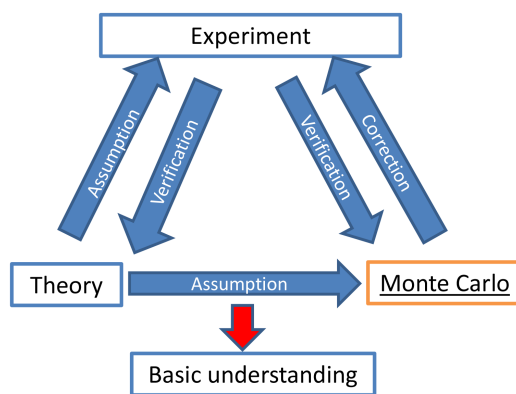


Figure 3.1: Scheme of the MC method

The idea of simulating experiments using statistics was firstly applied by Comte de Buffon (1777) and Laplace (1786). Then, in 1940s, Metropolis and Ulam suggested the name *Monte Carlo methods*(MC) to indicate stochastic approaches to solve the Boltzmann equation for neutron diffusion. Originally this kind of resolution was firstly applied by E. Fermi at Rome University in the late 1934 to his work on transport problem, but never published. This method is a powerful tool applicable to integral-differential equations and not

only. The core of a MC method, as statistical algorithm, is based on the sampling mechanism and then the deduction. More in details this algorithm retrieves data from known statistical distributions. Then, the sampled information is interpreted by mean of a deduction process, in order to obtain the physical quantity of interest.

Since the early days MC method was mainly used on random processes, such as radiation transport, and then applied successfully to many other fields.

A MC simulation helps in the validation of a physics model, or in the development and confirm of an experiment.

In comparison with classical statistics where the samples are taken by direct observation, in MC methods these are simulated by a computer algorithm. The solution of a mathematical problem is decomposed by one (or more) estimator of a parameter distribution.

As any kind of algorithm, MC method introduces a statistical error to the systematic ones, that the algorithm could intrinsically have.

Statistical deviation of the estimator, and however global uncertainties, can be reduced by increasing the sample size, but with an higher computational cost.

The general scheme for a Monte Carlo algorithm application follows the next steps:

1. Formulation of a mathematical model for a physical phenomenon.
2. Statistical interpretation of the problem highlighting the interested quantity in terms of parameter distribution.
3. Develop an algorithm for sampling the distribution.
4. Derive estimators for the parameter and uncertainties. In radiation transport often called Tallies.
5. Optimization of the algorithm to reduce computing time.
6. Sample is generated sufficiently large to achieve the desired level of accuracy.
7. The parameters and uncertainties are estimated using the sample.

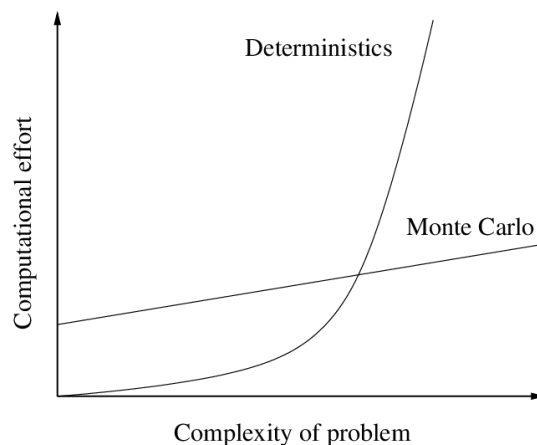


Figure 3.2: MC method[18]

In the most general point of view the convergence criteria of a Monte Carlo computing is strictly function of the requested accuracy.

3.1 Deterministic Model Vs Monte Carlo method

A deterministic mathematical problem models a physical phenomenon where input parameters are well defined and the solution in output is addressed in a unique way. The models can be linear or non-linear, depending on the representative equation, and can always be solved by discretization and numerical approximation.

The major difficulty lies on the dimension of the problem space, i.e. many physical problems are characterized by a 3D space. In then case of the the LBTE, the transport problem becomes even more more complicated, since the dimensions are more than 3.

The most common ways to solve numerically a 3D spatial problem:

- Finite Difference (FD).
- Finite Element(FE).

These methods give a good results if the phenomena is steady state, but in the case of a time dependent problem, some approximations can be performed like:

- Time series of steady state.
- Dynamic model.

With a Monte Carlo approach, it is possible to simulate the physical problem behaviour by its elemental phenomena.

In this way a unique input (the pdfs-probability density functions of the elemental phenomenon) can lead to different outputs for each simulation run. A single execution gives only one result, that is one of the possible outcomes. Hence it needs multiple runs to retrieve a distribution as result(see Fig.(3.3).

Stochastic systems can be described by different types of processes such as Markovian process, Poisson process, Brownian one etc.

The choice to use an analytical approach or a MC simulation is driven by the characteristics of the system under investigation, such as:

- Space Dimensionality of the system (1D, 2D or 3D).

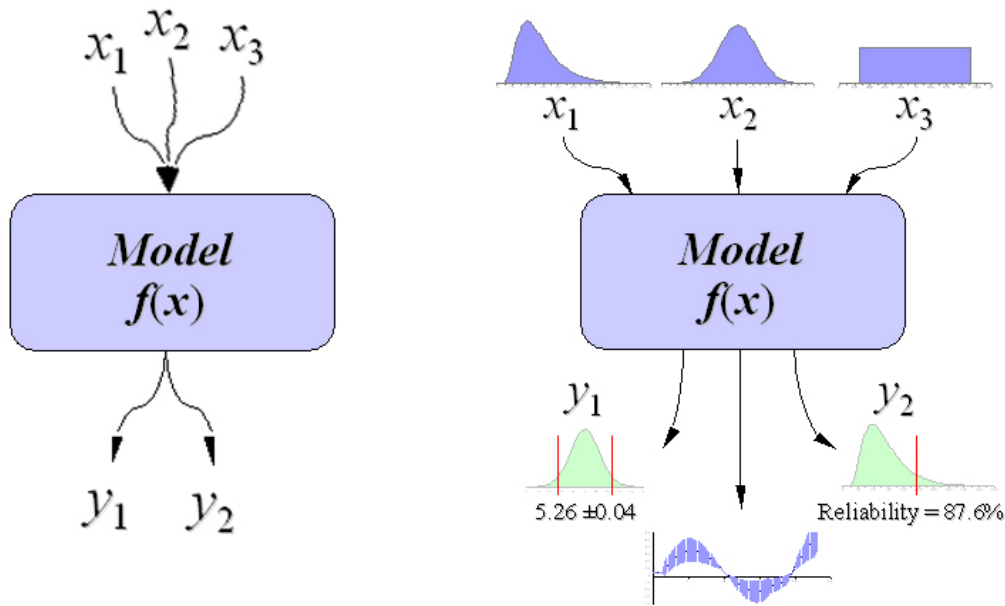


Figure 3.3: Probabilistic(on the right) Vs Deterministic model(on the left) (adopted from[18])

- Time dependence.
- Physics of the process.
- Path or memory dependence of the process.
- System parameter strongly dependant on the state of the system.
- Homogeneity vs Heterogeneity of medium.
- Availability of computational time.

In conclusion, it is possible to say that deterministic models are usually adopted for system with few dimensions, describing the system behaviour on physical laws. In a live radiation transport system (in a domain like the human body), a totally deterministic model can be too restrictive because does not include dynamic random effects or uncertainties; it has a 7-D phase space where the parameters are strictly affected by uncertainty and energy dependence. Therefore a Monte Carlo method is more appropriate to describe such complex system.

3.2 Sampling: Composition method

As described in previous sections, the main part of a Monte Carlo approach is the sampling mechanism: generate numbers according to a probability distribution. The most important method is the *Inverse transform method*[33], the simplest and fastest way to generate numbers according to a *pdf* (probability density function) $f(x)$. However, the corresponding *cumulative density function-cdf*, $F(x)$, must exist, and it should be invertible. In other words:

Let a random variable X have a continuous non-decreasing cumulative distribution $F(x)$, that is invertible. If the inverse of the cumulative distribution is called F^{-1} , the variable X can be generate, starting from U , uniformly distributed in $U \in (0,1)$, such as $X = F^{-1}(U)$

The advantage of this method is the speed, or in other words the generation efficiency,(each U gets a X). Anyway, the existence of an invertible cdf is the main disadvantage, because it is not always available.

In order to overcome these difficulties it is possible to use other sampling mechanisms like, the *Composition method*[33].

Assuming now that a cdf $F(x)$ can be expressed like a sum of other cdfs: F_1, F_2, F_3, \dots , each of these with an associated weight, p_1, p_2, p_3, \dots , such that:

$$F(x) = p_1 F_1(x) + p_2 F_2(x) + p_3 F_3(x) \dots \quad (3.1)$$

with $\sum_i p_i = 1$ (at the same way it is possible to express the pdf $f(x)$ of $F(x)$ like sum of pdfs).

Algorithm:

- Generate J from uniform distribution in $(0,1)$, such that $P(j = J) = p_j$;
- Retrieve X with the cdf F_j , so X is generated independently from j ;

This method is very useful in transport problem, where the particle interaction mode, J , is selected by the probability p_j . Then for this interaction is associated a corresponding statistical distribution for the possible state of the particle after the interaction.

Obviously the method is consistent only if the distributions involved cover all possible outcomes.

3.2.1 Example: Composition method for protons beam

Recalling the concepts in section (2.7), each interaction can be associated with the corresponding probability of occurrence, (e.g the cross section of a reaction Σ_i) . Let consider now a proton in the state x , before the interaction, in the easiest form, x can be an energy value, or a direction of flight; so let it be:

$$\begin{aligned} f_{tot}(x \rightarrow x_1, x_2, x_3, \dots) = & p_1(x)f_1(x \rightarrow x_1, x_2, \dots) + \\ & + p_2(x)f_2(x \rightarrow x_1, x_2, \dots) + p_3(x)f_3(x \rightarrow x_1, x_2, \dots) + \dots \end{aligned} \quad (3.2)$$

The (eq.3.2.1) represents the probability for the particle to go from the state x into x_1 after the collision, by mean three different ways, respectively with probability p_1, p_2, p_3 :

- p_1 : Coulomb interaction probability.
- p_2 : Bremsstrahlung probability.
- p_3 : Nuclear collision probability.

Obviously the algorithm, firstly samples the kind of interaction, then the state of particle by mean the relative pdf.

In this way, it is possible to cover any interaction type and any related successive state, knowing only all the events probabilities for protons (or any other particle). Particle transport phenomena can be easily represented by a succession of statistical independent events, the process is memoryless and can be assumed *Markovian*. The reason is that the particle next state is function only of the present state, forgetting all the previous life.

3.2.2 Combination of Rejection and Composition methods

In particle transport is very rare to have an easy invertible cdf for sample random numbers. So it needs a combination of sampling methods: *Rejection and Composition methods*[14]. If x is sampled from the pdf $f(x)$ defined on the interval $[x_1, x_2]$, and it is possible to express $f(x)$ as[6][13]:

$$f(x) = \sum_{i=1}^n N_i \cdot f_i(x) \cdot g_i(x) \quad (3.3)$$

with $N_i > 0$; $f_i(x)$ normalised in $[x_1, x_2]$, and $0 < g_i(x) < 1$ is the rejection function. So, it is possible to retrieve x by mean the following algorithm:

- choose $i = \{1,2,3...\}$ according to the probability N_i
- select x_0 according to $f_i(x_i)$
- accept or reject x_0 by mean the evaluation of $g_i(x_0)$, if rejected restart.

This method is efficient if the f_i and g_i can be easily evaluated. The average number of trials in order to obtain x_0 is $\sum N_i$.

From the definition of the algorithm in eq.(3.3) is possible to see that if all $g_i = 1$, is the case of a pure "composition", otherwise if $n = 1$ is a pure "rejection method"[6], with a function $g(x)$.

3.2.3 MC Error

The output of a Monte Carlo method is always an approximation of the exact value of the exact solution of a physical problem, and therefore is always associated by an error.

The error associated to a Monte Carlo output value is always related on the number of trials performed.

If ξ is the exact value of a certain quantity, by mean a *data-generating mechanism* [21] is possible to generate independent data, collecting a sample $\{X_1, X_2, ..X_N\}$. The algorithm gives $\bar{\xi}_N$ as an approximation of ξ . So the error related to ξ_N is:

$$Err(\bar{\xi}_N) = \frac{\sqrt{\sigma^2(\bar{\xi}_N)}}{\sqrt{N} \cdot \bar{\xi}_N} \quad (3.4)$$

With σ^2 is indicated the variance of the distribution $\{X_1, X_2...X_N\}$, and $Err(\xi_N)$ will be the relative error for the MC approximation. Looking at the Eq.(3.2.3), the major parameter that can discriminate the accuracy of the result, is the dimension of the sample, N . If $N \rightarrow \infty$, the error goes to zero and the ξ_N tends to the exact value ξ .

3.3 Code *GEANT4*

The goal of this work is to analyse the dose deposition profile of a proton beam. In order to fulfil this job, a computer code is used to elaborate the transport phenomenon, particle by particle, and event by event.

One of the most applied codes in this field is *GEANT4*[14] (GEometry And Tracking code). This is an object oriented open-source code, based on C++, firstly developed by CERN and then its use and development are made by an international support community.

The fields of application of Geant4 are many and wide, from particle accelerators, to space applications, study of high energy physics, nuclear experiment, radiation protection and obviously medical physics, including applications of microdosymetry (*GEANT4-DNA*).

This code have a Monte Carlo core based on a combination between rejection and composition methods (see sec.3.2.2). A simulation is divided hierarchically in elemental units, as shown in the graph 3.4:

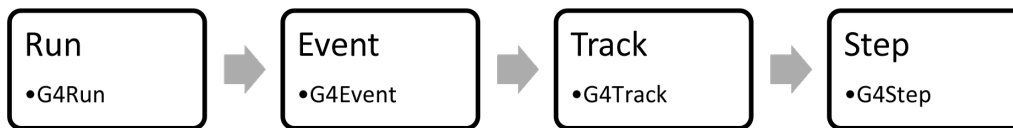


Figure 3.4: Geant4 hierarchycal subdivision

- A **Run**[14] is a collection of identical events (same particles shoot).
- An **Event**[14] contains the information on particles generation and tracking, with the hit collection.
- A **Track**[14] is a representation, of the particle motion in the detector environment.
- A **Step**[14], the smallest unit, contains and updates the particle properties(energy). Also it contains the spatial information of the beginning and end of step, with the relative position.

In order to create a MC simulation for an experimental set-up, it is mandatory to implement at least:

- Main file: sets user interface, declares user classes, manages output data and sets the run manager.
- Sources files.
- Header files: definition files.
- *Mandatory Action Classes*[14]:
 - PrimaryGeneratorAction*: controls the generation of particles, e.g. G4ParticleGun.
 - DetectorConstruction*: defines isotopes, materials, geometry and sensitive detector.
 - PhysicsList*: defines physics packages and particles, depending on the process simulated.

The code can simulate the path of the defined particle, tracking the released energy on the detector and all the others quantities of interest. G4Event simulates also the path of the secondary particles and photons generated by interactions. To perform a complete run, GEANT4 proceeds from *Bottom to Top and Top to Bottom*(Fig.(3.5)).

Firstly the code develops the primary particle path, from the source to the end. Then it proceeds with the evaluation of all the "branches" of secondary particles or photons.

For the materials used in detector construction, Geant4 can use the *NIST-Material database*, but as well it is always possible the definition of a new material starting from each constituent element, and then declaring the material composition and density. This introduction on Geant4 is useful to understand the following sections, where this code has been used to create the databases for the treatment planning system.

Root In this work, most of the data analysis has been performed by means the software *ROOT*[5]. Root is an object oriented data analysis tool-kit, based on C++. It has been developed by CERN, and designed specifically for particle transport analysis, moreover it is the preferred format for the Geant4 output.

Objectively it is not intuitive as other data analysis software especially for the beginner user, but it provides a great open-source tool, extremely useful for big data handling. If Root were compared with other similar software, it would show

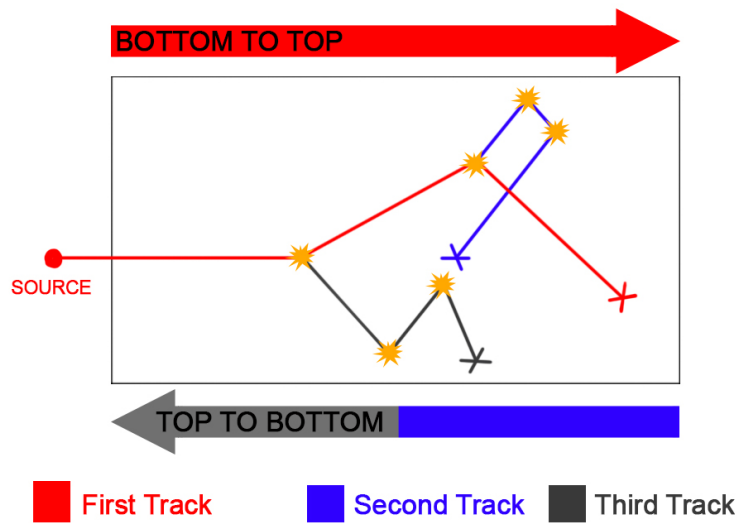


Figure 3.5: Succession order of Geant4 tracking

more calculation speed. The tool-kit can be integrated with other languages such as R or Python, but for the purpose of this work the language code used is C++. The software shows some interesting features for the statistical analysis, visualization and storage of data. The other remarkable characteristic of ROOT lies on the very accurate methods for curve fitting, with an helpful graphical user interface.

3.4 Geant 4 Simulations

The MC tool-kit of the previous section, has been used for the evaluation of the energy deposition profile of Figures(3.14) (2.9). During this investigation, several particles species have been simulated, with different energies, in order to compare their behaviour with the proton one. The code is called "*DataGen-iSee*", a fully Geant4 implementation.

The simulation apparatus, in Fig.(3.6), is a representation of the beam delivery system of *CNAO*¹[30].

The Geant4 model includes all the components of the dose delivery system (Tab.(3.1)), from the exiting window of the particle accelerator, to the sensitive detector, also keeping dimensions, materials, and position of the parts in the same scale.

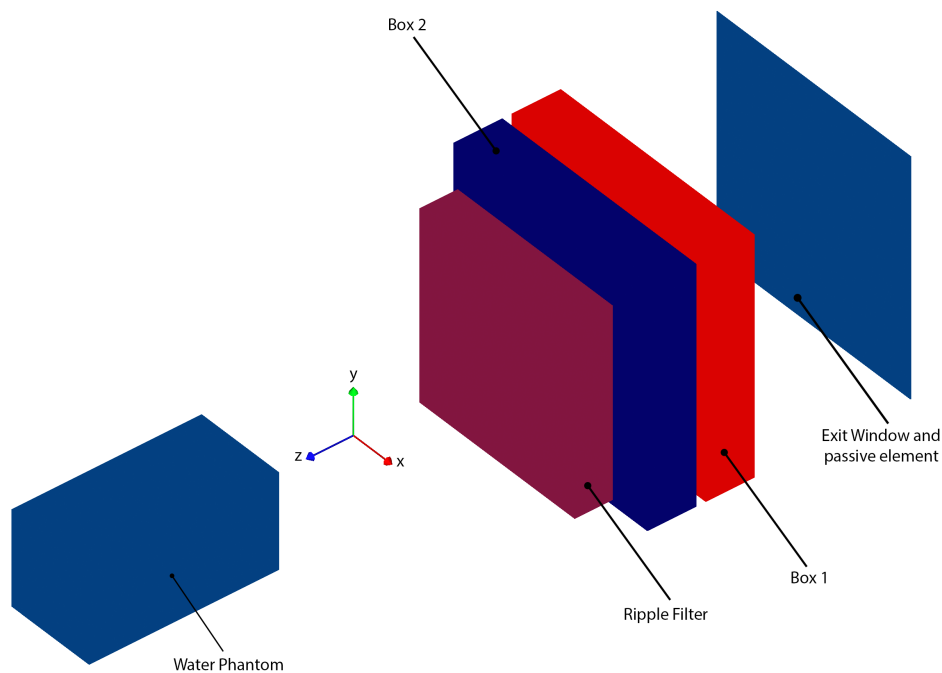


Figure 3.6: Detector model from Geant4 simulation

¹CNAO: Centro Nazionale di Adroterapia Oncologica in Pavia, specialized facility for treatment of deep seated tumour, with proton and heavy ions beam. The particle accelerator is a synchrotron.

Volume	Dim.(w,h,t)[mm]	Material	Composition	Density[kg/m^3]
World	(600,600,2000)	Air	$0.79N_2,0.21O_2$	1.29
BEP	(500,500,40)	Glass fiber	$C_2H_4O-CH_2$	1546
Ridge Filter	(500,500,40)	Perspex	$C_8H_{10}O_2$	1190
Box 1	(500,500,103)	Mylar	$C_5H_4O_2$	1390
Box 2	(500,500,103)	Mylar	$C_5H_4O_2$	1390
Ripple filter	(200,200,3)	Perspex	$C_8H_{10}O_2$	1190
Phantom	(200,200,400)	Water	H_2O	1000
S.D.	(40,40,400)	Water	H_2O	1000

Table 3.1: Table with the components described in the MC model, with dimensions and relative constituent materials

System description The whole apparatus is contained in a *world volume*, a 3D space, filled with air, where the Monte Carlo process is performed.

The particle enters in the world from the exit window² of the accelerator, passing through a *ridge filter* and a passive element, made respectively, of perspex and composite glass fiber.

Continuing the path, there is the *BOX1*, where sensible areas are placed with anodes and cathodes, used as diagnostic system for the beam.

With the blue colour in Fig.(3.6), is indicated the *BOX2*, also made of mylar and inside anodes and cathodes are situated, with the same function of *BOX1*.

The monitoring system present in *BOX1* is composed by two set of "strip" ionization chambers for the measurement of the position of the beam in (x-y), and a detector for the integral fluence. Instead in *BOX2* is placed a "pixel" detector for the beam positioning, and a second detector for the integral fluence.

The system is redundant for safety reason and interfaced with the control subsystems of the accelerator and with the scanning magnets system in order to set and check position and fluence of the beam.

The last object on the particle path is the *Ripple Filter-RF*(see Fig.(3.9)) or *Range Shifter*, entirely made in perspex, with a ridges pitch of 2mm.

The last component in the particle path is the *Water phantom*. Inside this test volume, in the code, is implemented the region where is collected the energy deposition.

The so called *Sensitive Detector* is declared like a series of very thin slices (0.01mm

²In Fig.3.7 it is called "Carbon shutter"

thick) with height and width equal to 40mm , exactly centred on the beam axis. In the following Figures (3.7) and (3.8), the layout of the components described is shown, with a water phantom in use at LNS-CT in Fig.(3.10).

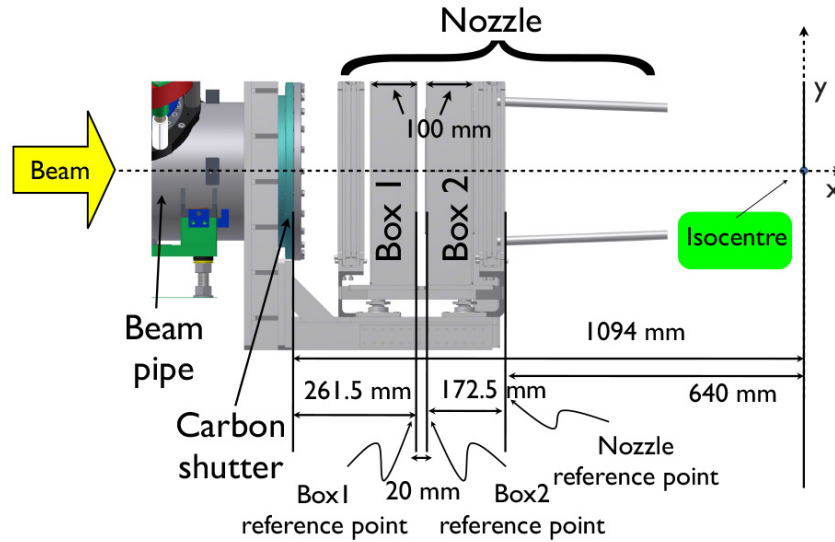


Figure 3.7: Position of CNAO beams components[30]

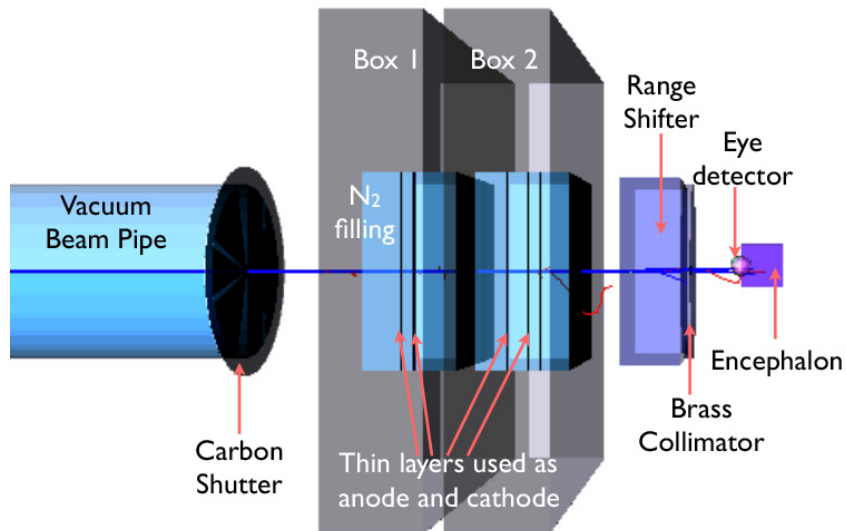


Figure 3.8: 3D view of CNAO passive scattered dose delivery device[30]

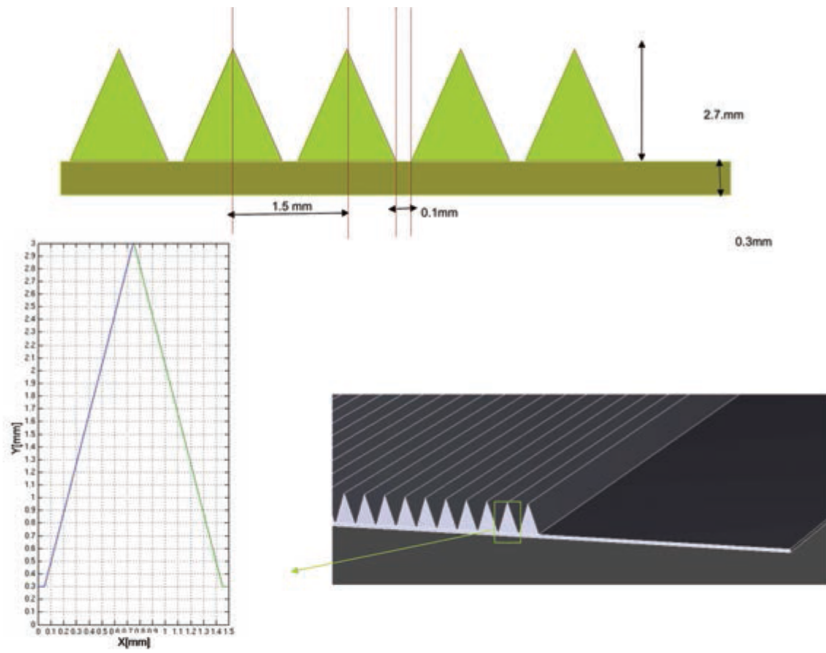


Figure 3.9: Section and parameters of the ripple filter of CNAO proton beam line [3]

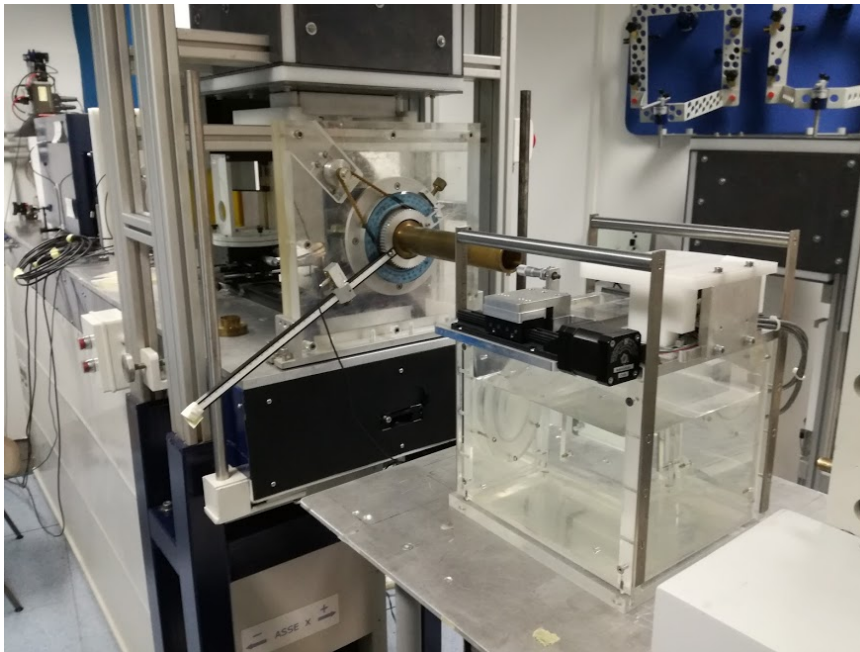


Figure 3.10: Water phantom test apparatus at LNS-INFN CT

Source definition In *DataGen-iSee*, the particle definition is made by declaring their characteristics (charge, atomic and mass numbers). The source implementation, in this case, is made by *G4ParticleGun*, specifying position, energy, and emitting direction.

In details, the source emission has a Gaussian distribution, for the position at $(x, y, z = 0)$ with a standard deviations $\sigma_x = \sigma_y = \sigma = 2.553mm$, and mean values $\mu_x = \mu_y = 0mm$. (see (Eq.(3.5)) and the graph in Fig.(3.11).

$$f(x, y) = \frac{1}{\sqrt{2\pi\sigma_x^2}} \exp\left[-\left(\frac{x^2}{2\sigma_x^2}\right)\right] \cdot \frac{1}{\sqrt{2\pi\sigma_y^2}} \exp\left[-\left(\frac{y^2}{2\sigma_y^2}\right)\right] = \frac{1}{2\pi\sigma^2} \exp\left[-\left(\frac{x^2 + y^2}{2\sigma^2}\right)\right] \quad (3.5)$$

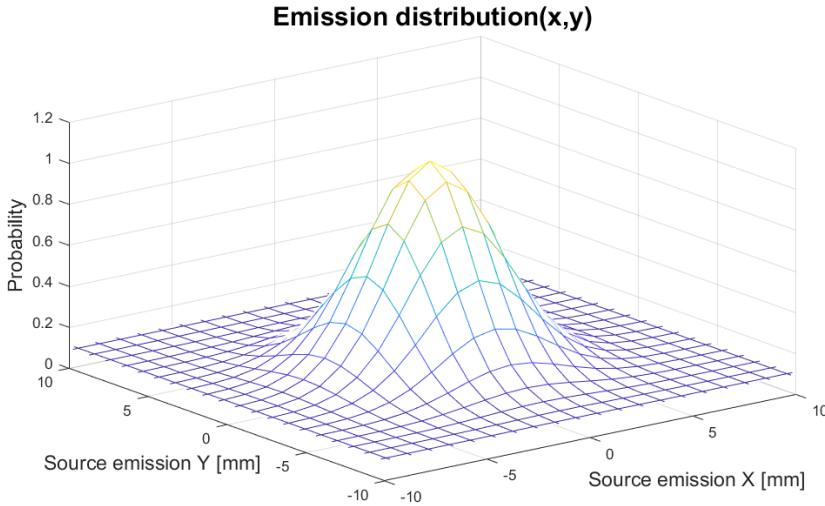


Figure 3.11: Source position distribution

In the same way in *PrimaryGeneratorAction*, there is the definition of the momentum vector at the emission, in order to define the beam angular spread. The direction distribution at the initial state is modelled with a very narrow Gaussian distribution around z . This simulate a good Z collimated beam, with director vector $(x, y, z = 1)$, $\sigma_{xM} = \sigma_{yM} = 10^{-5}$, $\mu_x = \mu_y = 0$ (similar to Eq.(3.5)). All of these parameters are extremely consistent with the real CNAO accelerator.

The last characteristic is the energy profile of the source, that in the case studied is perfectly mono-kinetic, with a different value for each simulation.

Accuracy parameters The Geant4 model needs the definition of some accuracy parameters, mainly dictated by the scale of the problem. One of these parameters is the *Cut-Length*, which represents the path length travelled by a whatever particle, or radiation, under the approximation of continuous slowing down. In protontherapy, the uncertainty associated with a deposition profile must be very low. In order to achieve this, the *Cut Length* is constrained to $1mm$. As a consequence, if a particle could travel a distance less than the cut length, the code neglects its tracking. The other important parameter is the *Step Max*. It is the maximum path length allowed to a particle between two consecutive interactions. In this case the value is dependent to the voxel dimension, $Step_{max} = 0.1 \cdot L_{voxel}$.

3.4.1 Applications of DataGen-iSee

The interaction mode with the code is by mean macro file where the user can tune the simulation parameters, such as: particle type, beam energy, graphic output and the result format. In this way, the various simulations have been executed. In Tab.(3.12) a summary of the parameters setted in the macro files for the simulation performed in this work is reported.

This code was built and run in a virtual machine with *Ubuntu 18.04*, with two processors assigned @3,40GHz and 3GB of RAM. Each simulation with different parameter takes different execution time, depending on the particle energy and type, and overall on the event number. For this academic elaborate, a maximum of 10^5 events has been imposed by the hardware performance.

The results are reported in the following histograms. They has been elaborated using Matlab for the 1D dose distribution, while for the 2D distribution ROOT was used. In the graphs of Fig.(3.13) and Fig.(3.14), the energy deposition is expressed in $[MeV]$ and as normalized pdf, in order to show qualitatively the trend. A quantitative analysis would have requested an higher amount of processed events.

Particle	Energy [MeV]	N° of events	Energy/u.m. [MeV/u.m]	Particle	Energy [MeV]	N° of events	Energy/u.m. [MeV/u.m]
p/H	70	10000	70	C-12	840	500	70
p/H	100	10000	100	C-12	3000	500	250
p/H	150	10000	150	C-12	3240	1000	270
p/H	200	10000	200	C-12	3240	500	270
p/H	250	10000	250	C-12	4200	500	350
He-4	280	1000	70	C-12	4500	500	375
He-4	600	1000	150	C-12	4800	500	400
He-4	1000	1000	250	C-12	5160	500	430
He-4	1400	1000	350	Ar-40	2800	1000	70
Ne-20	1400	1000	70	Ar-40	5000	1000	125
Ne-20	5000	1000	250	Ar-40	10000	1000	250

Figure 3.12: Summary of preliminary simulations

3.4.2 Energy deposition profile

Focusing on the proton dose deposition profile, below in Figures(3.13, 3.14,3.15,3.16), some histograms are reported with the energy deposition in the water phantom in 1D and 2D. The pdfs reported in fig.3.13 are very useful, because, at a certain point, the deposited energy can be easily calculated, multiplying the pdf by the total energy of a proton beam giving the exact amount of energy deposited in a certain point. In Fig.(3.13), the position of the Bragg peak can be seen varying the beam energy. With high energy value the maximum is shifted on the left, but its height decreases. The reason is that, the most part of dose is already dispersed on the previous path, in the plateau region. A particularity can be found on the drop after apex. At minimum energy the curve is almost vertical, otherwise begins a slightly tilt.

Spreading phenomena, on orthogonal plane and on beam directions can be seen very often on light nuclei, because they are more influenced by elastic electrostatic scattering with target nuclei (Fig.(3.15) and Fig.(3.16)). In Figures (3.17) and

(3.18), there are the projections of dose profiles on x axis (on BRS-beam reference system), those graphs are made taking an interval of 0.80mm around the interested z coordinate and then fitted by a Gaussian function.

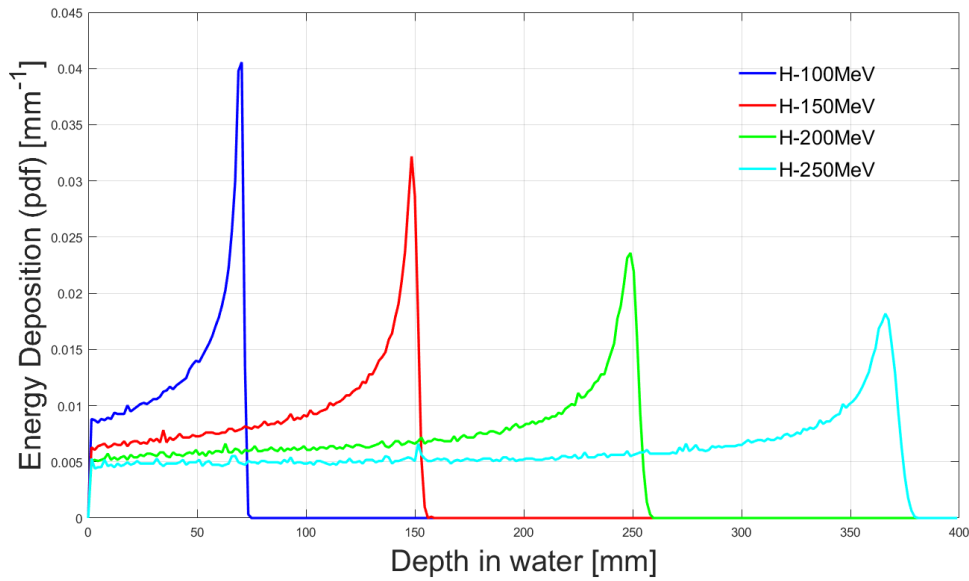


Figure 3.13: 1D proton energy deposition pdf (10^4 particles simulated).

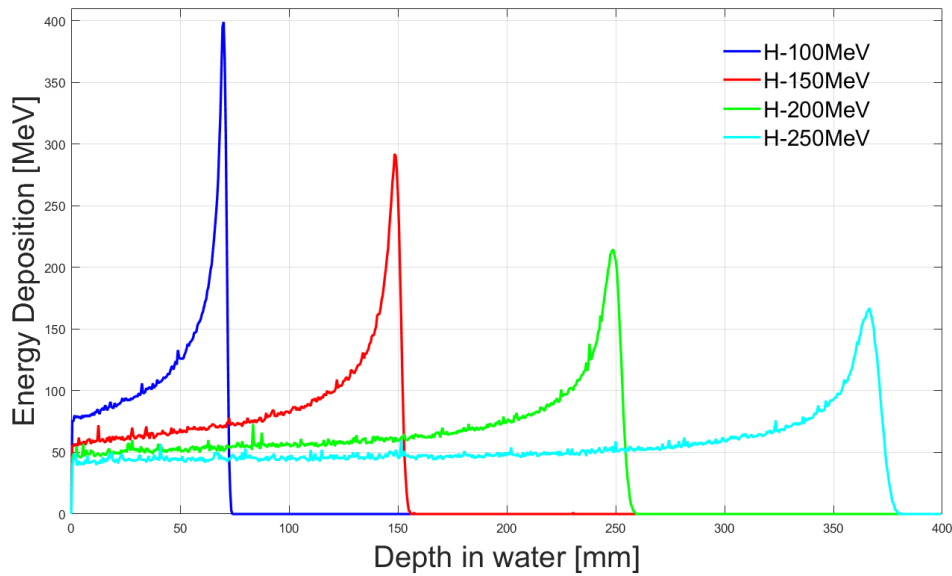


Figure 3.14: 1D proton energy deposition profile, (10^4 particles simulated).

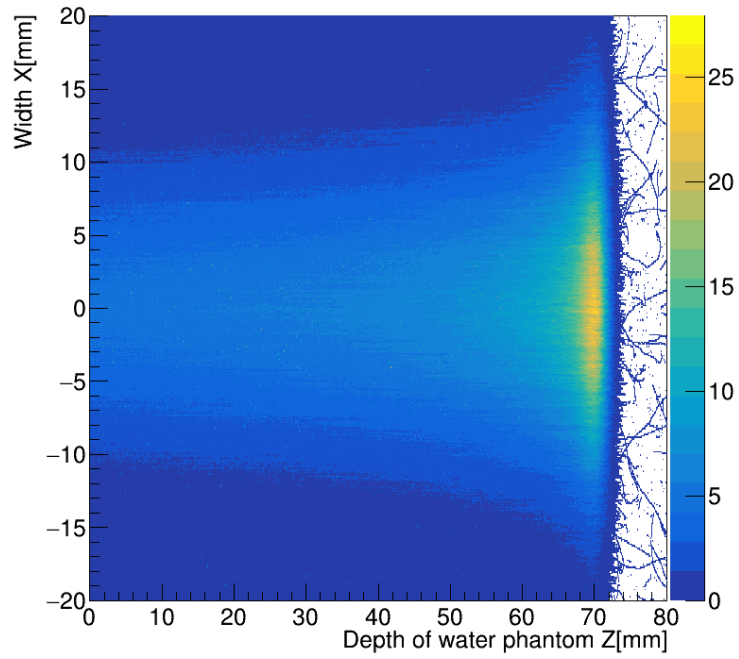


Figure 3.15: 2D protons energy deposition ($E = 100\text{MeV}$, 10^5 particles simulated).

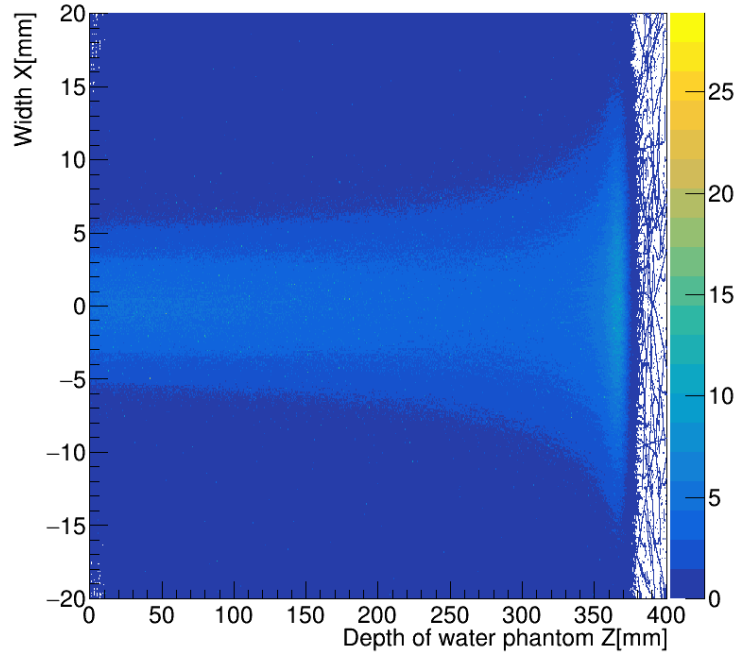


Figure 3.16: 2D proton energy deposition, ($E = 250\text{MeV}$, 10^5 particles simulated.)

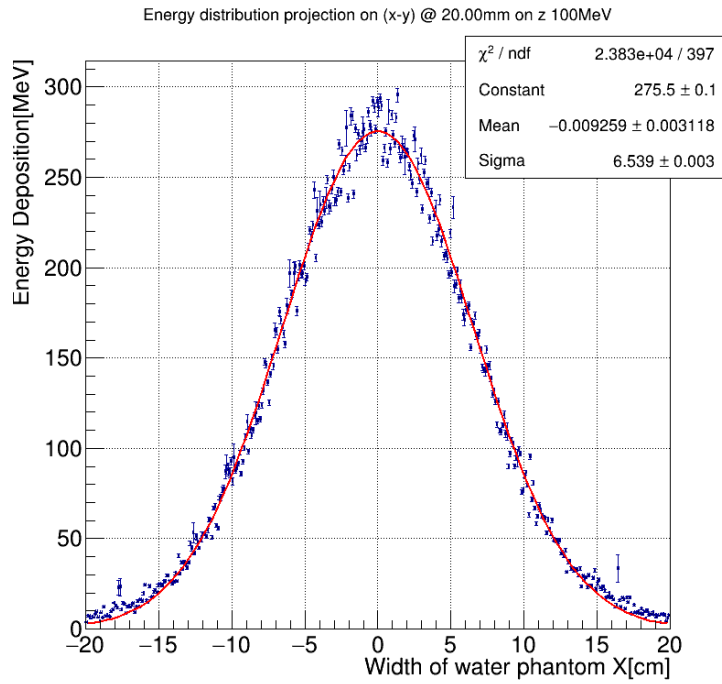


Figure 3.17: Projection of Energy deposition on x axis @20mm 100MeV protons, in the plateau region.

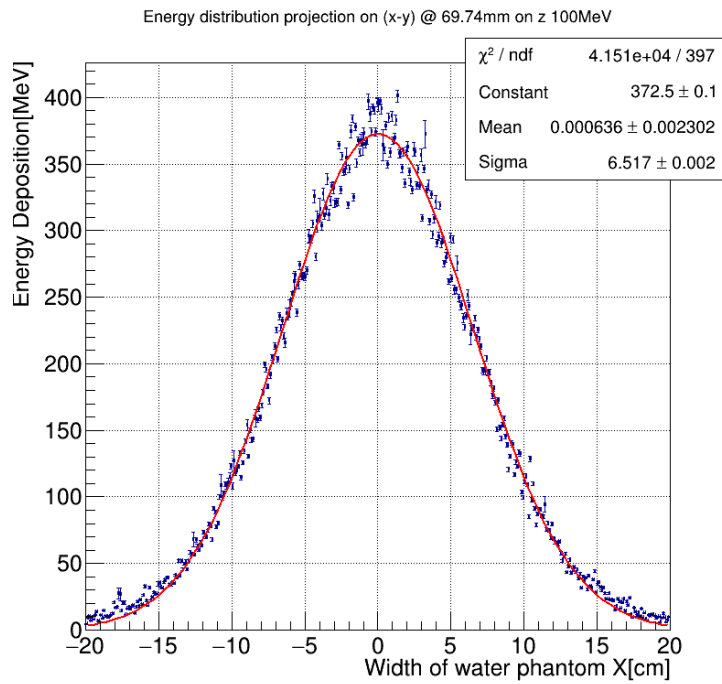


Figure 3.18: Projection of Energy deposition on x axis @69mm(Bragg Peak) 100MeV protons.

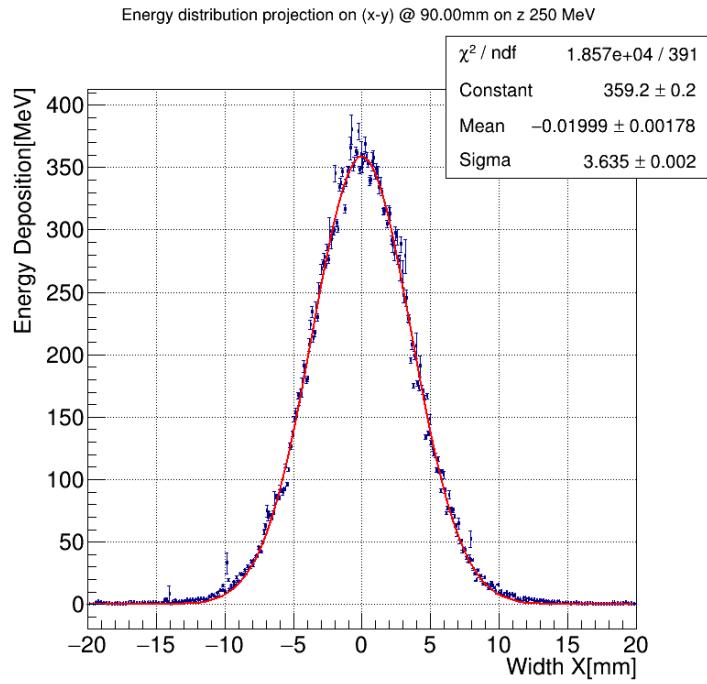


Figure 3.19: Projection of Energy deposition on x axis @90mm 250MeV protons, in the plateau region.

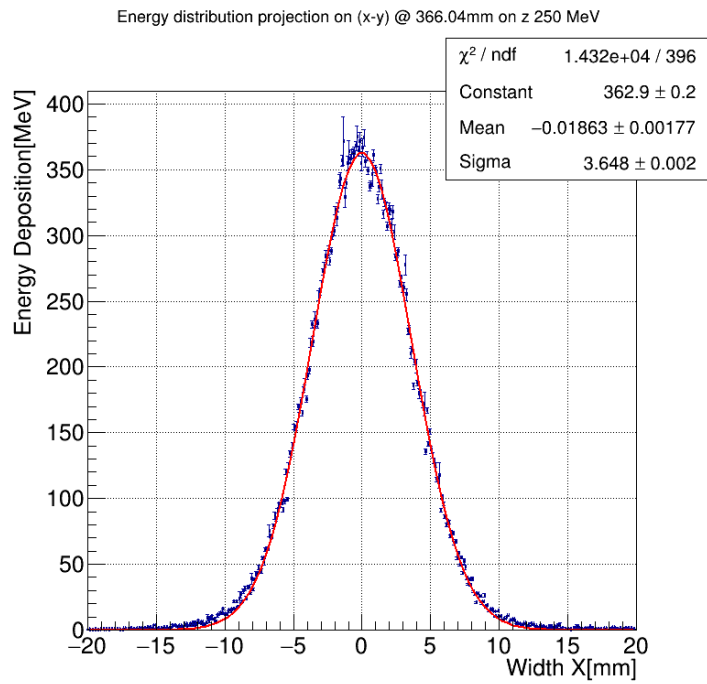


Figure 3.20: Projection of Energy deportation on x axis @366.04mm(Bragg Peak) 250MeV proton.

3.5 Protons Vs Heavy ions

With the various simulations performed, (in Tab. (3.12)) the different behaviour of various particles species can be seen. The comparison concerns only charged nuclei, because for γ -rays, X-rays or other *low LET* particles do not have the penetrating power to pass through filters and monitoring systems, hence the sensitive detector does not collect any deposition.

Comparing directly the profiles from detection raw data is an hard job, because the simulations are performed with different values of initial events. The only way to compute a parallelism is to look at the pdf of the dose deposition for the geometry simulated. The probability density function for each particle tells the quantity of dose deposited in the interval dz per unit of energy in input to the system. In other words, it is the probability to have a deposition in a certain neighbourhood of z .

In Figures (3.21) and (3.22) the trends for various particles are reported, from the lighter like protons or helium, to the heavier like Neon or Argon. The tested nuclei are chosen according to the most common in the hadron-therapy field, keeping the same specific energy per unit of atomic mass.

Starting from the proton profile at $70MeV$, it shows a very deep penetrating power and a smaller Bragg peak, than others one. Also in the first portion of path it has an almost constant deposition, very similar to the helium one.

On the contrary the heaviest nucleus, Ar , at low energy, presents a peak at the beginning of the detector, due to the strong Coulomb interactions with detector nuclei. It is the demonstration that bigger is the projectile shorter will be its path inside the medium, because it loses very fast its energy by mean collision with the smaller atoms of water.

Carbon and Neon ions show an intermediate behaviour, between light and heavy nuclei.

The analysis continues looking on the opposite side, with an higher specific energy of $250MeV/(u.m.)$ (fig.(3.22)). The stopping point is increased for all species, and the heavier nuclei begin to show a very sharp Bragg peak, its height decrease with the projectile mass. A particular note concerns the helium profile, increasing the energy, it shows the maximum in the same region of the proton peak, becoming also sharper.

In the graph analysed, the demonstration of the goodness of proton therapy is shown, especially for deeply seated tumour, and also the lightest mass gives the

opportunity of using a more affordable particle accelerator, like *Linacs*, *Cyclinacs*.

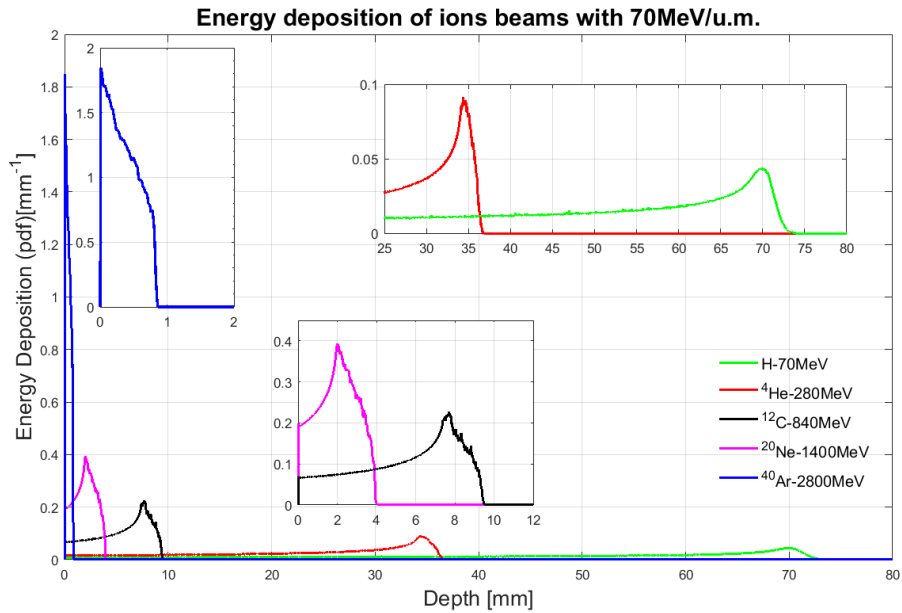


Figure 3.21: Energy deposition profiles comparison between heavy particles beams and protons ones at $70\text{MeV}/(u.m.)$

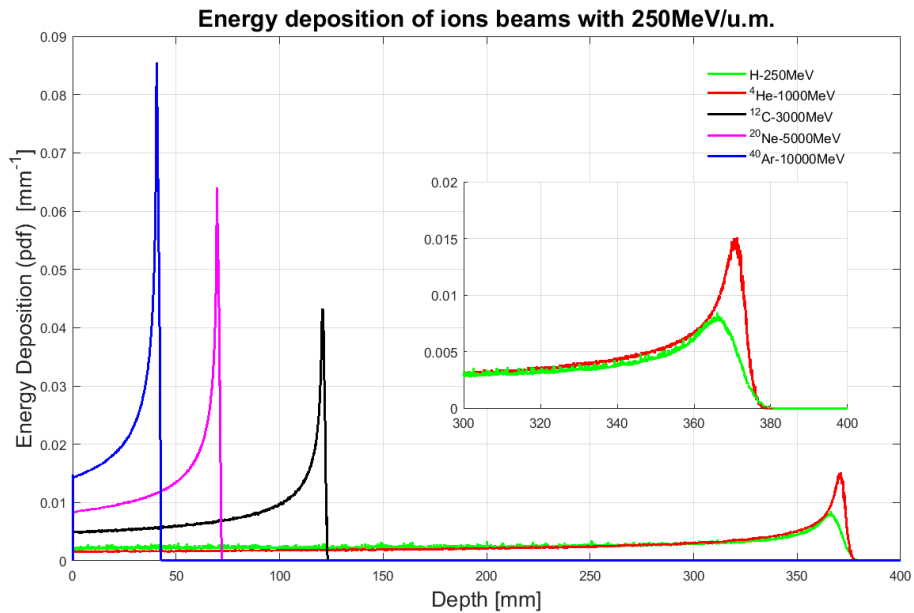


Figure 3.22: Energy deposition profiles comparison between heavy particles beams and protons ones at $250\text{MeV}/(u.m.)$

Convergence test Recalling the section 3.2.3, for the simulation of proton beams is been performed a converge test, to prove the decreasing trend of the relative error associated with the distribution.

This test is done for proton beams with an energy of $160MeV$ and $250MeV$, considering a different number of events, from 500 to 10^5 . From the code output have been obtained the mean value of the distribution, $\bar{\xi}_D$ and the standard deviation δ , so it is very simple the evaluation of the relative error $Err(\xi_N)$ (see Eq.(3.2.3)).

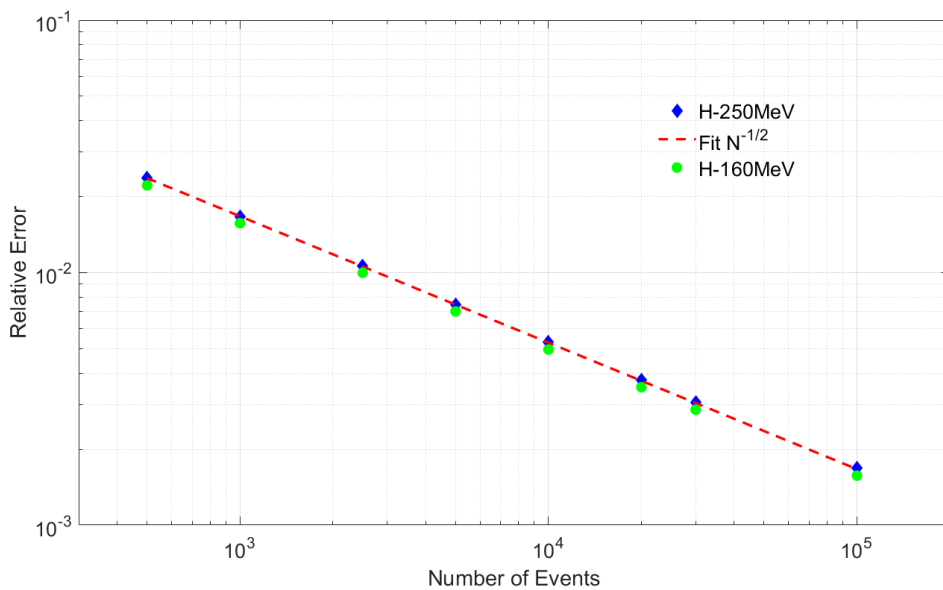


Figure 3.23: MC simulations relative error function of the number of events

In a clear way it is possible to see in Fig.(3.23), that the simulation error follows the curve $N^{-1/2}$, in a double logarithmic scale. The code convergence is very slow, in order to increase one order of magnitude the accuracy, it needs a thousand times more events.

3.6 Dose profiles superposition

One of the properties of the radiotherapy in general, and in particular of the proton therapy is the effects superposition.

This simple principle is very important, because by mean different beams projected from various angles, positions and terminal set-ups, the interest volume can be covered by the prescribed dose.

Analytically the principle can be applied summing up the *Dose-Depth Histograms*. These diagrams can be summed bin by bin, in order to obtain the resultant of a multiple beams superposition.

This principle can be used only in the case of sum of collimated beams. In the case of the projections from different angles the procedure would be wrong. Each beam would see a different path, hence it would needs a specific simulation for the new layout.

In Tab.(3.2), a summary of the simulation used for the super position is reported. In the following, there are some graphs with the 1D distribution and 2D profile of dose deposition.

The superposition of beams has been calculated for three energy values, always with the same complete model of Fig.(3.6).³

Particle	Energy [MeV]	N. Events
H	100	10^5
H	140	10^5
H	160	10^5

Table 3.2: Simulations used for the demonstration of the superposition principle

³The superposition of the other combinations are reported in appendix (A)

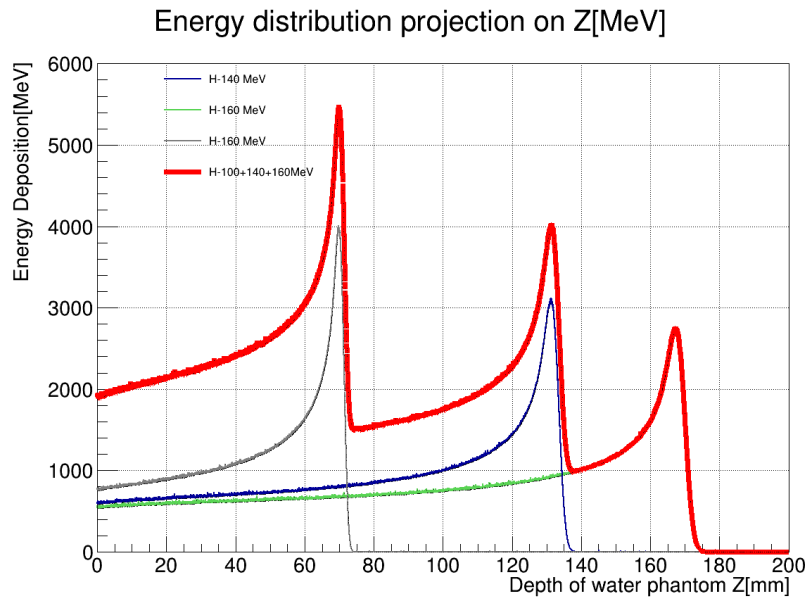


Figure 3.24: 1D dose distribution for the superposition of protons beams at 100MeV , 140MeV and 160MeV

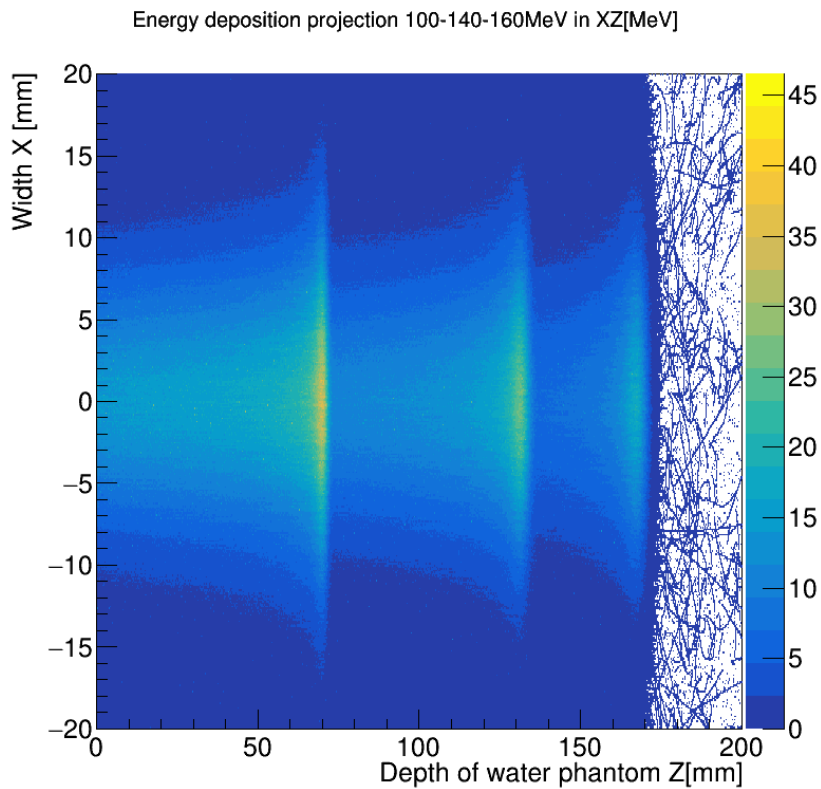


Figure 3.25: 2D dose distribution for the superposition of protons beams at 100MeV , 140MeV and 160MeV

Chapter 4

Monte Carlo databases for proton therapy

After the description of the different deposition profiles and of the method used for the calculation, a contextualization in the field of proton therapy is needed.

In oncology treatment an homogeneous and regular volume of interest, like the water phantom, is almost impossible to find. For this reason the delivery of the dose in a certain domain of the human body is a very complicated procedure, *called Treatment planning system*.

The *Treatment Planning System-TPS* is a process, based on the patient anatomy, that defines the number, direction and energetic profile for proton beams according with the volume to treat.[31][12]. The aim of this process is scanning the PTV, choosing and optimizing, the dose delivery according to prescribed dose.

At this point is useful to define the interest volumes in a radio-treatment. The domain in exam can be divided in[31]:

- *Gross Target Volume-GTV*[8]: it contains all macroscopically detectable portions of tumour tissues. It can be defined by visual or palpation detection, as well by clinical imaging.
- *Clinical Target Volume-CTV*[8]: it contains the GTV, and all possible undetectable tumour margins.
- *Planning Target Volume-PTV*[8]: it contains the previous two volumes plus all possible structures and healthy tissue in proximity, that can be interested by uncertainties, mispositioning and patient mobility.

- *Organ at Risk Volume-OAR*: in order to guarantee an adequate attention to healthy tissue, it is important to highlight the potentially exposed organs. In Analogy to PTV, OAR Volume needs to evaluate damages on healthy tissues, by mean a risk evaluation for secondary syndromes.

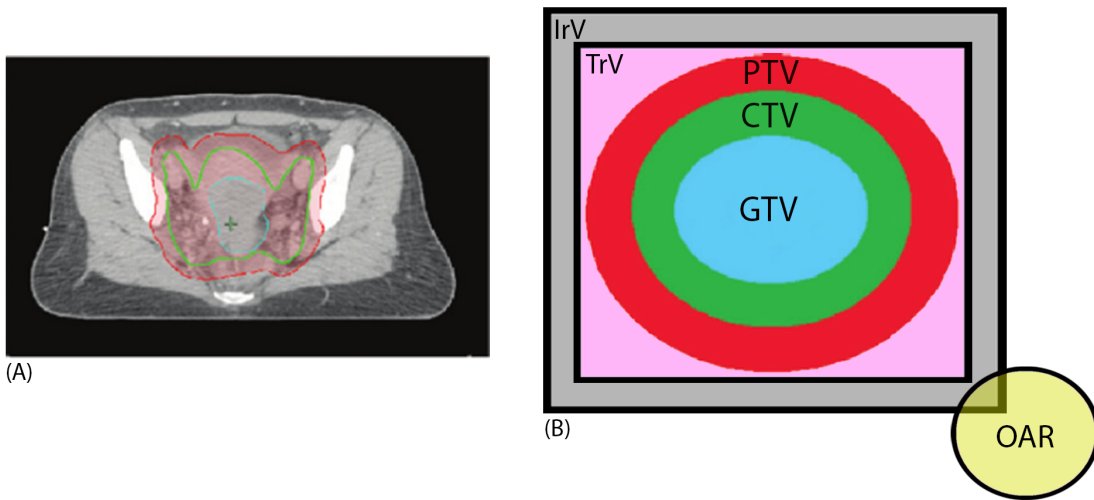


Figure 4.1: Target volume scheme and representation[8]

Each defined domain is discretized in *voxels*, a three dimensional unit of volume, and for each of those is also defined position and its physical properties in terms of stopping power, mass density and radiosensitivity coefficient (typical for each tissue). Also for each voxel is assigned a prescribed dose from the radiotherapist. From this point the *forward planning system* starts, associating for each voxel a beam, so if $\eta =$ voxel number, and $\lambda =$ proton beams: $\eta = \lambda$.

The method defines a proton beam that projects its Bragg peak at the centre of an elemental volume, this entire procedure is called *voxel scanning*.

Only as principle it is possible to use for the forward planning system a Monte Carlo simulation for each beam, but in practical terms it becomes unmanageable. It would take a too high computational time.

For instance, if it needs a single MC run for one voxel, the time spent would be on the order of $4h$. The solution that can be adopted, for this multidimensional proton transport problem, is taken from the conventional photon-radiotherapy, by

mean the *Water Equivalent Thickness-WET* method[2].

Knowing the position of the i-esim voxel on the beam reference system(BRS), t_m , that corresponds to a thickness of the analysed medium, it is possible to define a water equivalent thickness, t_w , as in Eq.(4.1). The other informations necessary are the mean stopping power¹ of the medium and water, and their densities[2].

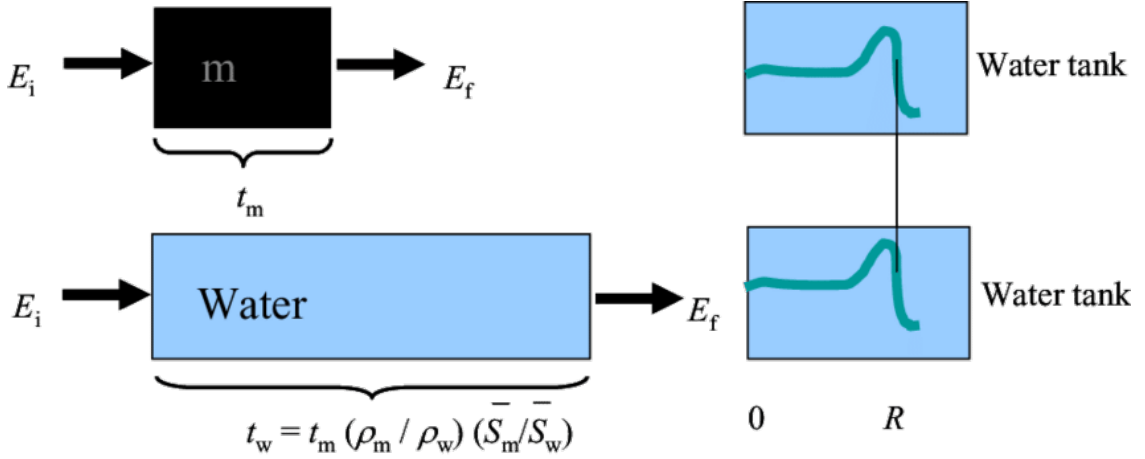


Figure 4.2: Scheme of WET method[2].

$$t_w = t_m \cdot \left(\frac{\rho_m}{\rho_w} \right) \cdot \left(\frac{\overline{S_m}}{\overline{S_w}} \right) \quad (4.1)$$

In this way the problem becomes referred in a water equivalent system, very similar to the one seen in chapter (3.4).

The WET have the advantage to shift an heterogeneous medium in an equivalent homogeneous one, sparing computational time and specific MC algorithms. On the other hand, WET-system introduce important simplification and so approximation on the results.

However MC simulations are still used in WET-method, because there is the necessity of a complete and precise set of data in the water-system containing the dose deposition profile for all the beam energies and also, for the dose delivery device set-up used. Commonly these databases are called *Look-Up Tables*. The next step in treatment planning is to calculate the kinetic energy of beam "k" to have the Bragg peak centred on the voxel "λ" of the water system. The calculation is a

¹ $\overline{S_m}, \overline{S_w}$, referred on the energy interval of interest.

simple linear interpolation between two consecutive beams from the look-up tables.

$$E_k(\eta, \lambda) = E'_k(\eta, \lambda) + (x_w(\lambda) - x'_{peak}(m)) \cdot \frac{E'_k(m+1) + E'_k(m)}{x'_{peak}(m+1) + x'_{peak}(m)} \quad (4.2)$$

$E_k(\eta, \lambda)$ = kinetic energy of the beam η for the voxel λ	$E_k(m)$ =kinetic energy of the "m" beam in tables.
$x'_{peak}(m)$ = coordinate of the Bragg peak of "m" beam in tables.	x'_w = coordinate of water equivalent system.

The forward planning system continues with the calculation of the dose delivered for each voxel of the treated volume, and a first optimization for the dose distribution.

A forward treatment planning system gives, as results, a set of proton beams with a certain energy profile and intensity, along with a first distribution of dose deposition on tissues.

This step can be performed by a dedicated software like "CarboProPlan" that can optimize the dose delivery to minimize the risk to exposed organs but also satisfy the prescriptions imposed.

A fully optimized treatment is achievable by mean the inverse planning system, that starting from the results of forward one performs the optimization of the dose delivery, scanning iteratively each voxel to ensure the correct deposition.

The optimization ends with a set of particle beams with a certain energy profile, intensity ($[particles/s]$ or $[nA]$, typical order of magnitude of the beam intensity for these applications), and direction, that guarantees the coverage of the PTV. A scheme of the final result is reported in Fig.(4.3), with a representation of the *SOBP-Spread Out Bragg Peak*.

4.1 Database for Proton therapy

As already introduced, a complete MC algorithm, to define and optimize a treatment planning, would be too expansive in terms of computational time($\approx 4 - 6h$); for now the best option remains using a depth-dose database, a fast and easy method for clinical use.

The *Look-Up Tables* are specific for each dose delivery system, and for each particle species. These MC databases should cover the whole energy spectrum of interest, (in the case of proton therapy is $70 - 250MeV$), with a discretization as fine as

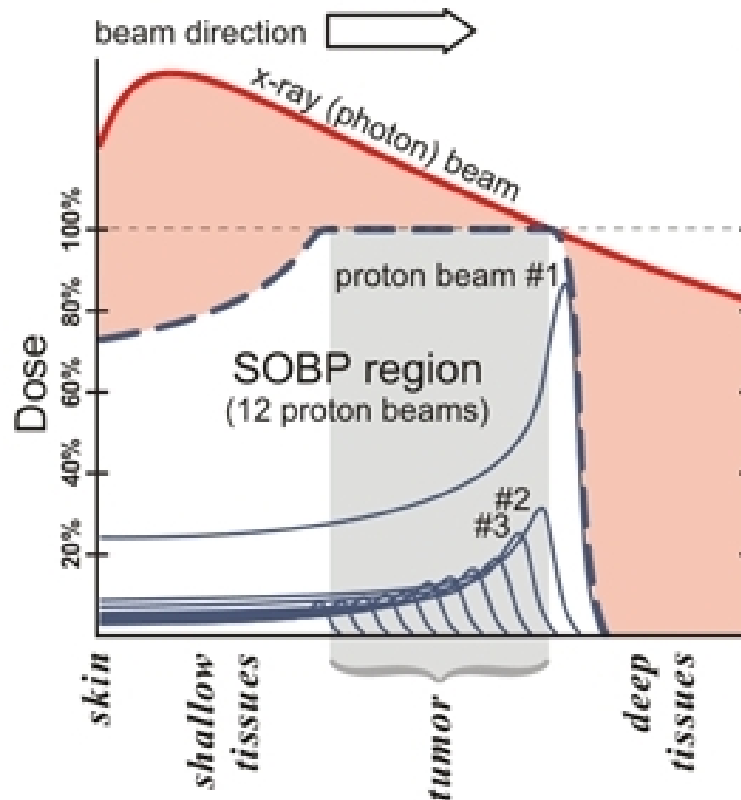


Figure 4.3: Scheme of a SOBP,

possible.

The other parameter of interest, that in the simulation must be defined, is the maximum step allowable; it is the longest path allowed for the particle between two consecutive interactions(see section(3.3)).

In the specific case of proton therapy the step max is setted $S_{max} = 0.1 \cdot L_{voxel}$ (for this work $L_{voxel} = 0.1mm$). Consequently decreasing the maximum step, the accuracy will increase, as well the computational cost.

For the purpose of this work, has been used the Geant4 software, "*DataGen-iSee*" to create two databases with the experimental set-up reported in chapter (3.4) and also with some modification on the beam delivery device.

For databases production, the various simulations must be performed with the same number of initial events. If this constraint is not satisfied, the dataset will be not homogeneous in terms of total energy input, and deposition in the sensitive detector.

4.2 Database with original settings

Here below in Tab.(4.1), the simulations performed are reported with the complete CNAO model of Fig.(3.6) without any variation.

All the simulations are independent runs, taking into account 10^5 initial events (initial number of protons), keeping the same accuracy parameters defined sec.(3.4). This value is limited by the hardware performance. Usually in the field, the number of simulations is approximately $\approx 10^8$, in order to achieve the requested error.

E_{beam} [MeV]	Z_{peak} [mm]	$Dose_{peak}$ [MeV]	σ_{peak} [mm]	E_{beam} [MeV]	Z_{peak} [mm]	$Dose_{peak}$ [MeV]	σ_{peak} [mm]
20	0.01	3	//	140	131.22	3106	5.04
30	2.53	3758	22.15	150	149.13	2925	4.89
40	8.54	4805	15.33	160	167.14	2753	4.66
50	15.81	5019	12.13	170	186.59	2593	4.47
60	24.38	4944	10.2	180	206.48	2450	4.33
70	34.15	4747	8.77	190	226.95	2307	4.17
80	44.99	4514	7.90	200	248.53	2178	4.07
90	56.95	4258	7.11	210	271.14	2083	4.05
100	69.74	3991	6.52	220	293.83	1951	3.90
110	83.82	3780	6.08	230	316.86	1855	3.84
120	98.79	3507	5.72	240	341.02	1743	3.76
130	114.54	3292	5.32	250	366.04	1648	3.65

Table 4.1: Depth-Dose database for the water equivalent system

The next step, after the conclusion of all the simulations, is a data handling procedure. For each energy deposition profile, the projection of dose is analysed on the orthogonal plane to the beam axis.

It needs the choose of 7 or more axial coordinates on the 1D profile and then use these points to evaluate the projection of the perpendicular axis using a neighbourhood of 0.8mm around the chosen point (80 bins around the interested point, each bin have the same thickness of the Sensitive Detector slice). The coordinates are selected taking into account the gradient of the 1D distribution. So in the plateau region(from entry point to the rise of BP) only few points are taken in consideration, then in the rise, Bragg peak, and fall-off regions are taken the majority, due

to increasing gradient of the 1D energy distribution. For each of these projections is performed a simple fit with a Gaussian function, in order to evaluate the later beam spread on the X-Y plane.

The sigma parameter of the Gaussian fit gives a measure of the amplitude of the spreading, (σ_{peak} value is reported on the table above, for the Bragg peak point projection).

A complete example of this step, with all the graphs is reported in appendix (C.0.1) and (C.0.2).

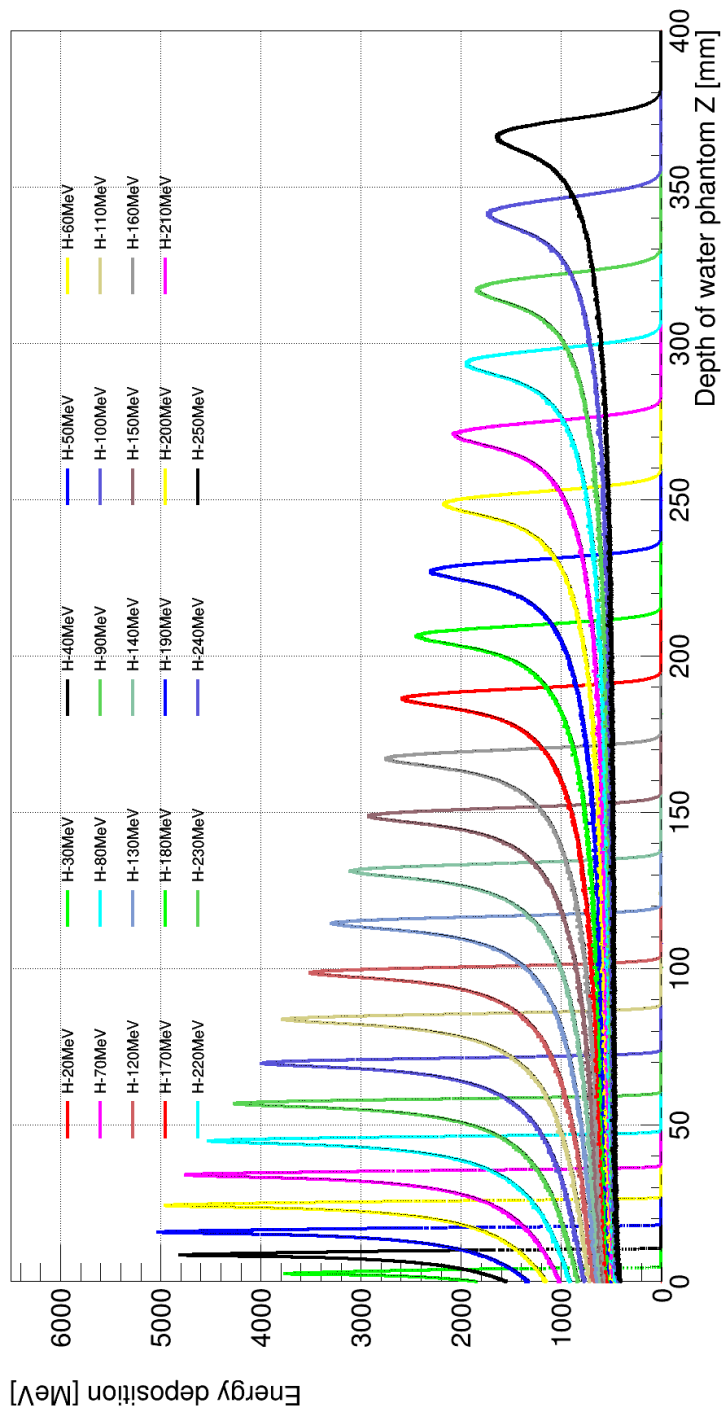


Figure 4.4: Graph of the total dose deposition for all the simulations for the database with the Ripple Filter

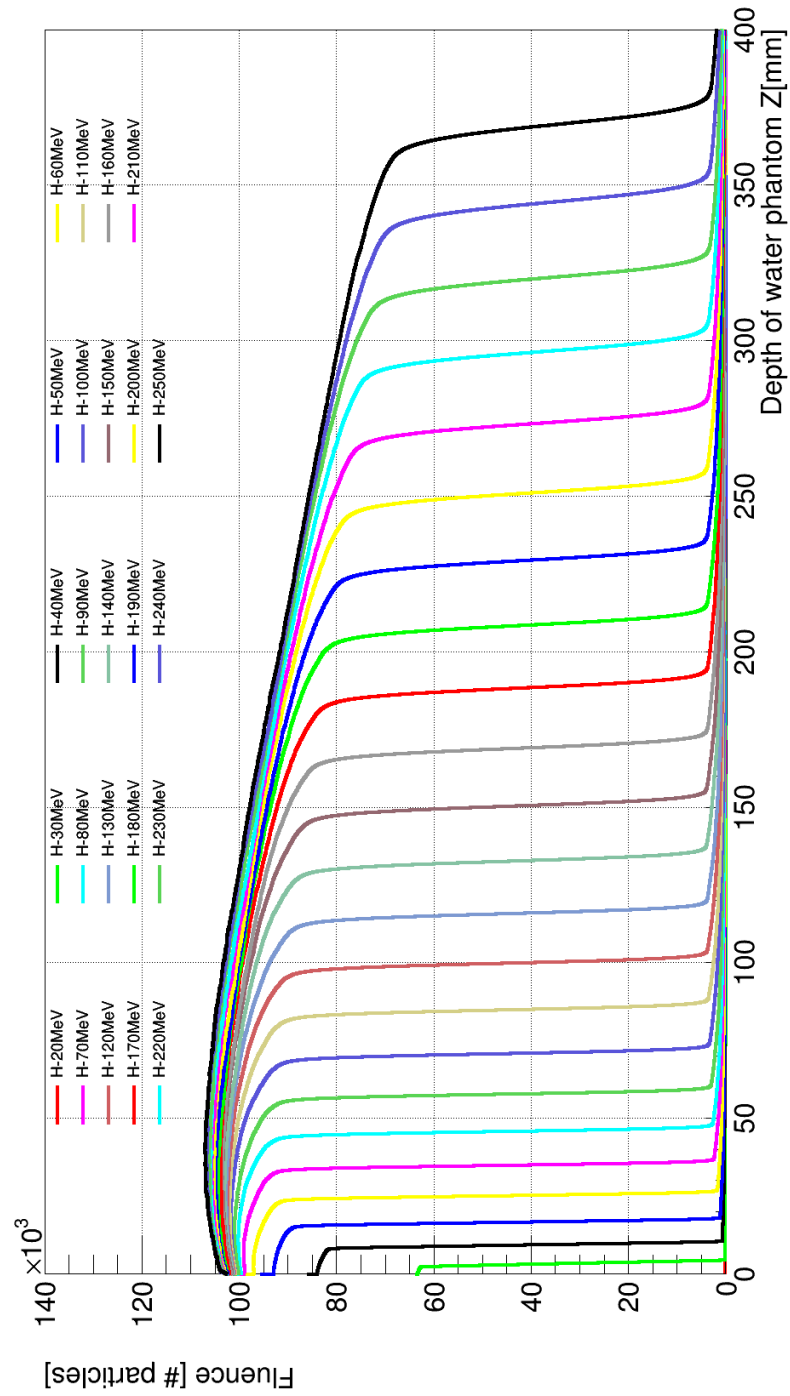


Figure 4.5: Graph of the total particles fluence for the database with the Ripple Filter

Particle fluence Vs Dose deposition The code "DataGen-iSee" is able to evaluate the fluence in the sensitive detector, but in this case it is not the usual fluence measured in $[\#Particles/(m^2s)]$, because the simulations are performed taking in exam one initial event at a time. So, it is simply the counted number of particles in the *i*-esim slice of the *Sensitive Detector*, or in other words, the integral of the angular fluence.

For what concerns the energy deposition, the results, reported in Fig.(4.2), show an rising of the range values along with the increasing of kinetic energy, but the maximum dose at the Bragg peak decreases.

Now comparing the two graphs of energy deposition in Fig.(4.6) and the total fluence in Fig.(4.7), it is shown that in the neighbourhood of the Bragg peak point, the fluence has an almost vertical fall, proving that most of the particles are absorbed in the maximum dose region.

In Fig.(4.7), the total particle fluence assumes a strange behaviour, from the value of 10^5 reach a maximum of $\approx 120 * 10^3$. This phenomenon is caused by nuclear fragmentation[29] of the target atoms, and also elastic scattering with the hydrogen nuclei of water.

The inelastic scattering events can be represented in general by reactions like the one described in Eq.(4.3) (the extracted particle/s can be neutrons, α or other fragments, usually together γ):



These reactions are nuclear processes where the target nucleus suffers a violent interaction with the production of fragments.

Another corroboration arises from the neutron fluence² in fig.(4.8,) where uncharged particles are produced by the interaction with water. Obviously neutrons are ejected from oxygen atoms (oxygen in water model is declared as the natural isotopic mixture).

A disadvantage of using a sensitive detector only inside the phantom is the loss of information regarding what occurs outside the water volume. This model neglects the neutral particles produced outside the detector that could give contribution in the dose profile.

The neutron fluence, at the highest energy, does not go to zero, and there is a current

²In appendix (B) the graph, of the neutron fluence for all the energies, can be found.

of neutral particles exiting from the water phantom. This fraction of particles, together with the ones produced in the acceleration line, represents one of the main issues for radiation protection in medical field³.

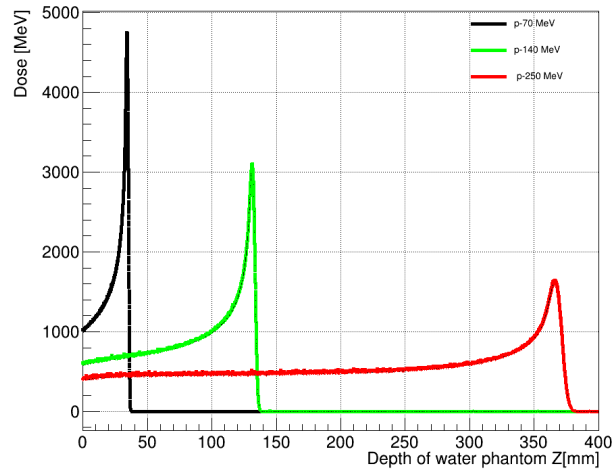


Figure 4.6: Detailed view of the deposition of proton beam with 70MeV, 140MeV, 250MeV, for the database with the Ripple filter

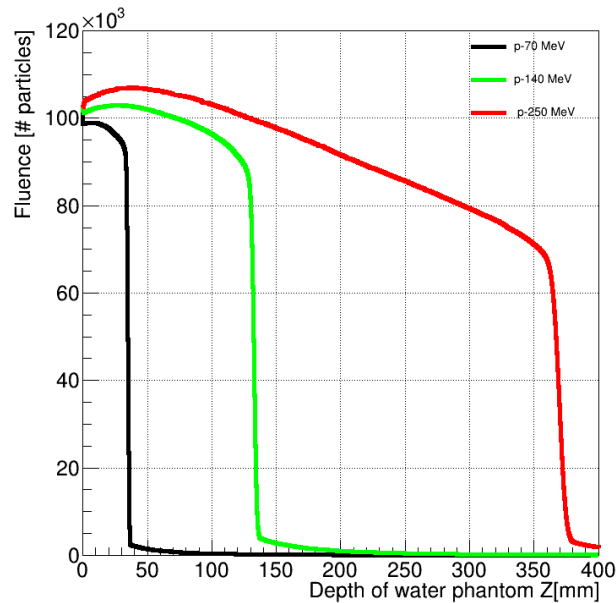


Figure 4.7: Detailed view of the total particle fluence for the database with the Ripple Filter

³The neutron fluence caused by the interactions between protons and beam line components, is proportional to the maximum energy beam present in the accelerator.

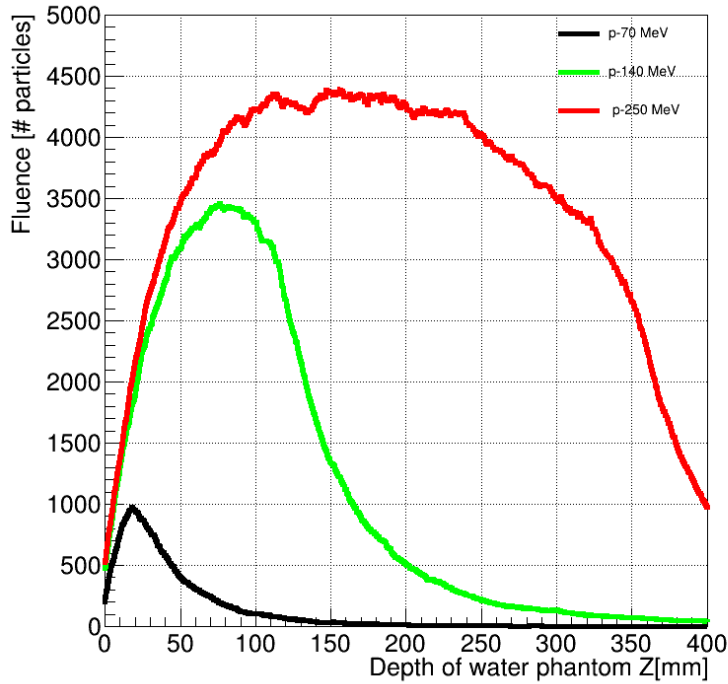


Figure 4.8: Detailed view of the neutron fluence for the database with the Ripple Filter

4.2.1 Dependence Energy-Computational time

In Fig.(4.9), the dependence between particle energy and execution time, it is possible to see the dependence between particle energy and execution time.

Keeping the same number of primary events (or primary particles) generated, there is an increase of the computational time, at first sight can be approximate to a linear increase.

The motivation of this behaviour lies on the quantity of interactions for each primary particle. As it has been said in previous sections, a proton loses a very small amount of energy for each interaction due to *MCS*. So increasing initial energy, particle takes a longer path and much more collisions until death. Moreover the daughter radiations number increases as well.

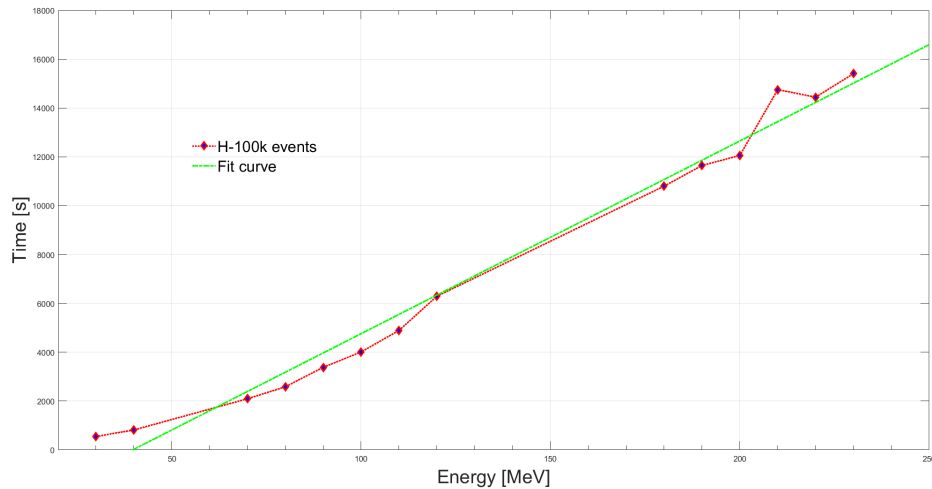


Figure 4.9: Dependence of computational time from proton energy (10^5 events)

4.3 Database without *Ripple filter*

In this section the dose delivery system model, has been modified (for reference see Fig.)), removing the *Ripple Filter-RF*. This component is also called *Range shifter*, due to its function of decreasing the position of the BP and so the proton beam range.

Consequently the whole system results modified and the previous set of *Look-Up tables* are no more consistent, with the actual set-up. Hence in this section, the same analysis is performed, in order to produce a second database coherent for the new apparatus. Another reason, for rebuilding the table, can be found looking at the Fig. (4.2), the lowest value of beam energy (20MeV) does not create any deposition in the detector, because protons are absorbed directly in the filter.

This device is made in perspex, with an atomic composition mainly composed by hydrogen and carbon. With these two elements, protons show a big scattering cross section, and so the ripple filter are also used to widen the Bragg peak.

In the real cases, Ripple Filters are also useful to create the *Spread Out Bragg Peak*, using different dimensions and materials.

Removing the filter from the Geant4 model is very simple, it needs the elimination, from the *DetectorConstruction*, of all the volumes(box, physical, and logical) related to the component, for example the various cathodes and anodes, windows and so

on.

In Tab.(4.2), the summary of the simulations performed with the new set-up is shown, keeping the same number of events (10^5 particles) and the same energy step of 10MeV , between 20MeV and 250MeV .

E_{beam} [MeV]	Z_{peak} [mm]	$Dose_{peak}$ [MeV]	σ_{peak} [mm]	E_{beam} [MeV]	Z_{peak} [mm]	$Dose_{peak}$ [MeV]	σ_{peak} [mm]
20	0.17	4717	/	140	132.77	3201	4.85
30	4.64	8364	19.24	150	150.16	2995	4.66
40	10.52	8245	14.45	160	168.73	2787	4.43
50	17.73	7445	11.41	170	187.70	2644	4.29
60	26.22	6576	9.63	180	208.04	2468	4.2
70	35.87	5828	8.35	190	228.58	2335	4.02
80	46.56	5277	7.53	200	250.29	2213	3.93
90	58.48	4744	6.76	210	272.22	2082	3.85
100	71.34	4320	6.23	220	294.61	1959	3.76
110	85.30	4002	5.78	230	318.65	1860	3.72
120	100.23	3683	5.47	240	342.94	1745	3.64
130	116.06	3435	5.11	250	367.73	1654	3.54

Table 4.2: Depth-dose database, for the water equivalent system in the set-up without the RF

For this set of *Look-Up Tables*⁴, the procedure is the same as the one performed for the previous system. So after the conclusion of all the simulations the data handling procedure starts using the same methodology already shown.

The last step, to use these databases, is a data handling procedure. For each 1D deposition curve it needs a non-dimensionalization respect to the Bragg peak coordinate (z_{peak} varies with energy). Finally the profiles can be used in a software for the forward treatment planning system.

After the simulation process all set of data collected must be verified by a real testing procedure on the proton delivery beam line. Obviously the test must be performed with the same set-up used in the MC models(hence with and without RF).

This process is the validation stage, before the direct application on a treatment

⁴The simulations at 240 and 250MeV have been performed merging 2 independent runs of 50k particles each, due to continuous crashes of the code with 100k events.

planning system, each database must be validate with the corresponding beam line in order to check the accuracy.

The procedure is useful to obtain the acceptability interval for the distributions found. Moreover the verification is also performed with heterogeneous medium that can mimics as well as possible biological tissues.

In this work the simulations are performed with only one run (with 10^5 events) per beam energy. In practical cases, multiple statistical independent runs are performed [30] for each beam energy, in order to guarantee a smaller deviation.

Regarding the uncertainties similar cases have been studied, for ocular treatments, in Rimoldi et al., but with only 4 energies examined, and a similar number of initial events ($2.5 \cdot 10^5$) giving consistent values of the Bragg Peak position.

As already specified, the iterations in a MC method is the key for a good approximation. But in the case studied, the exam covers an entire energy distribution on a water phantom, so there is not a single value to compare or to associate an error, but a distribution.

Both databases, that have been created for this elaborate, have already passed the validation procedure at the CNAO accelerator, and the apparatus simulated in the model is working already. The results are coherent with the measurements performed in an analogue real water phantom. The validation outcomes are reported in an internal private report: *"Internal report iSee for CNAO commissioning, 2013"*.

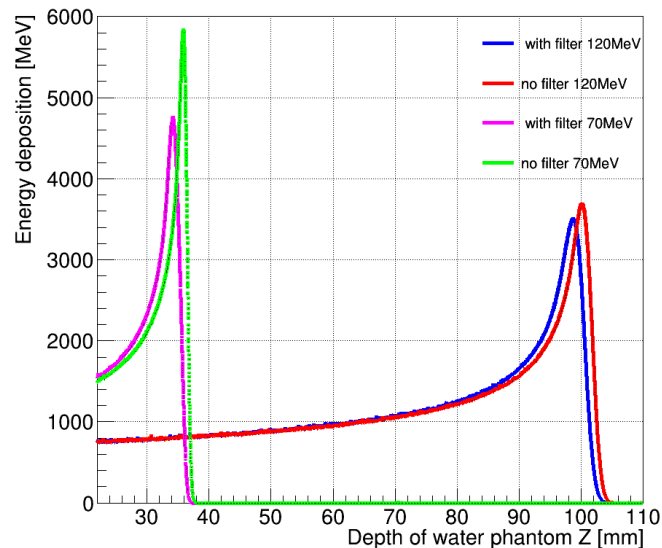


Figure 4.10: 1D dose deposition distribution for 70 MeV and 120 MeV proton beam, with and without the Ripple Filter

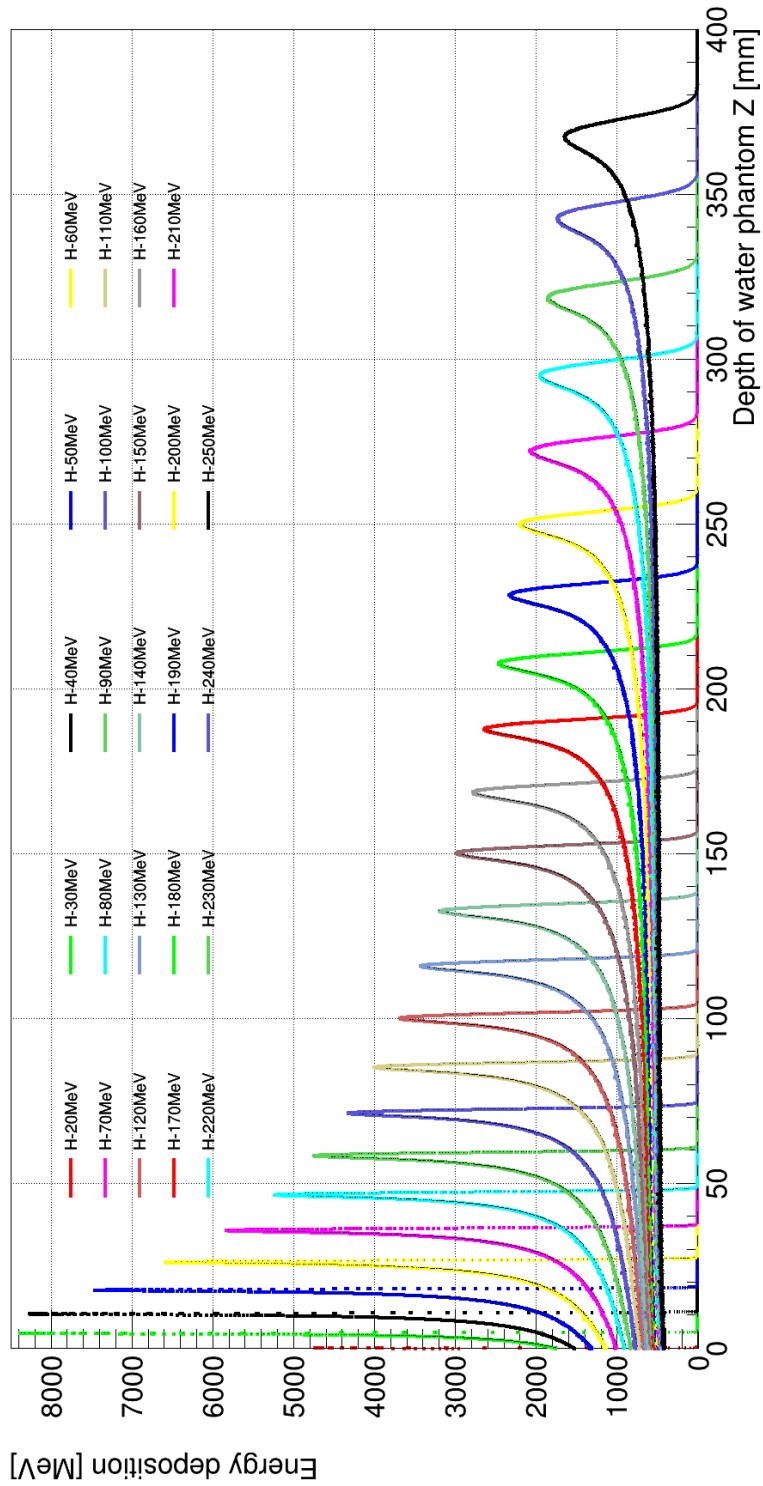


Figure 4.11: Graph of the dose deposition for all the simulations from 20 – 250 MeV for the database without the Ripple Filter

4.4 The role of a *Ripple Filter*

To highlight the behaviour of a proton beam in presence or not of a ripple filter, two simulations at 70MeV and 230MeV are reported as reference in Fig.(4.10), with the original settings and without the scatterer.

The device in the model and used at CNAO is designed only for protons. So it does not produce coherent results for other particle species.

In the graphs of Figures(4.10),(4.14) and (4.13), the 1D comparisons between the two system deposition are shown, considering three energy examples, in order to highlight the various differences.

Even if it is hard to see, the difference between both configurations is not only the shifting of the Bragg peak coordinate, but also the widening of the curve in the maximum region.(see Fig.(4.12))

The other main difference is related to the lateral beam spread,(in Figures (4.15) and (4.16)), the σ_{xyBP} is larger in presence of the filter. More scattering events in the particle path create a wider e smoother deposition curve.

Without a ripple filter the peak would be too sharp, so in order to create the SOBP (see Fig.(4.17)), it would need more beams setted with different energies. Consequently a smoother curve is helpful in order to use a smaller amount of beams and so less tuning on the beam energy, because each accelerator type has a characteristic time for the energy variation.

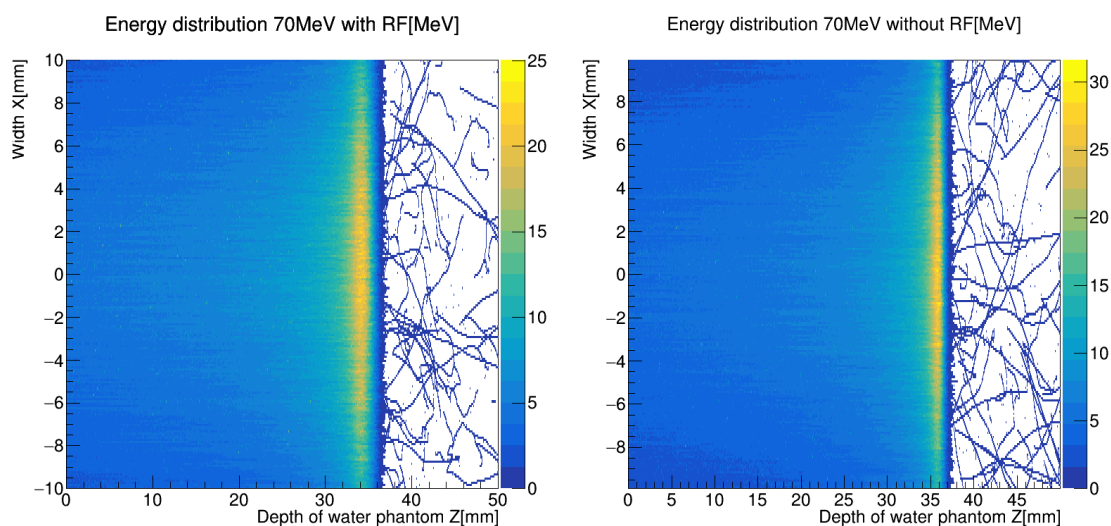


Figure 4.12: 2D dose deposition on XZ plane, with the ripple filter

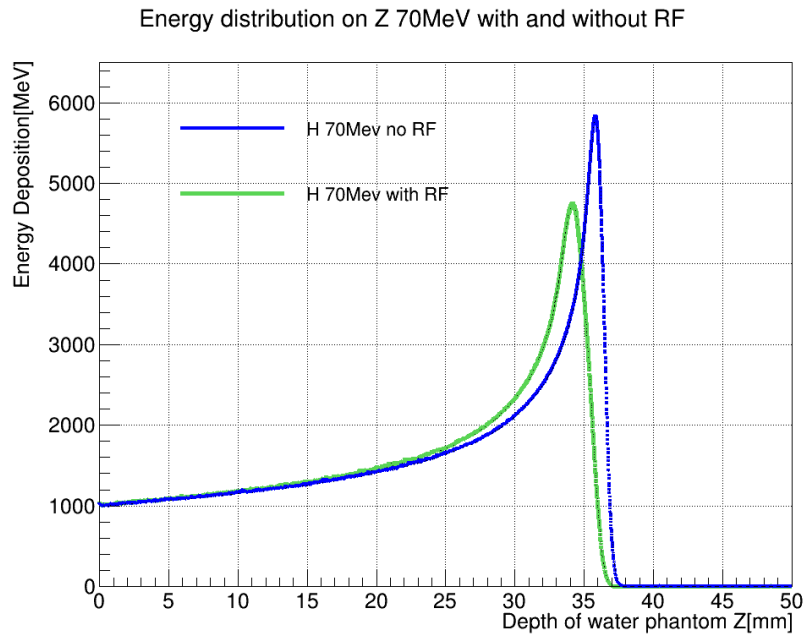


Figure 4.13: 1D dose deposition for 70MeV proton beam, with and without RF

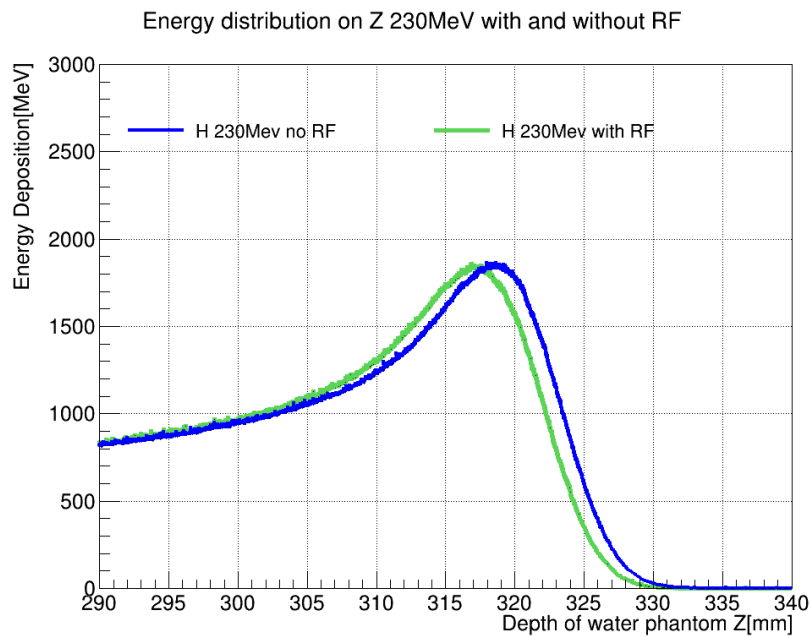


Figure 4.14: 1D dose deposition for 230MeV proton beam, with and without RF

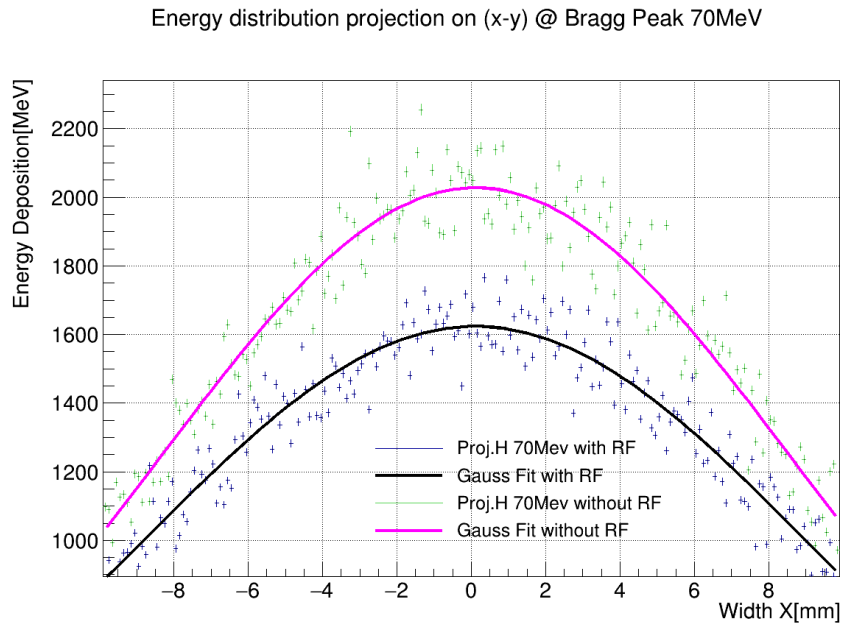


Figure 4.15: Projection at BP point, for 70MeV proton beam, with and without RF

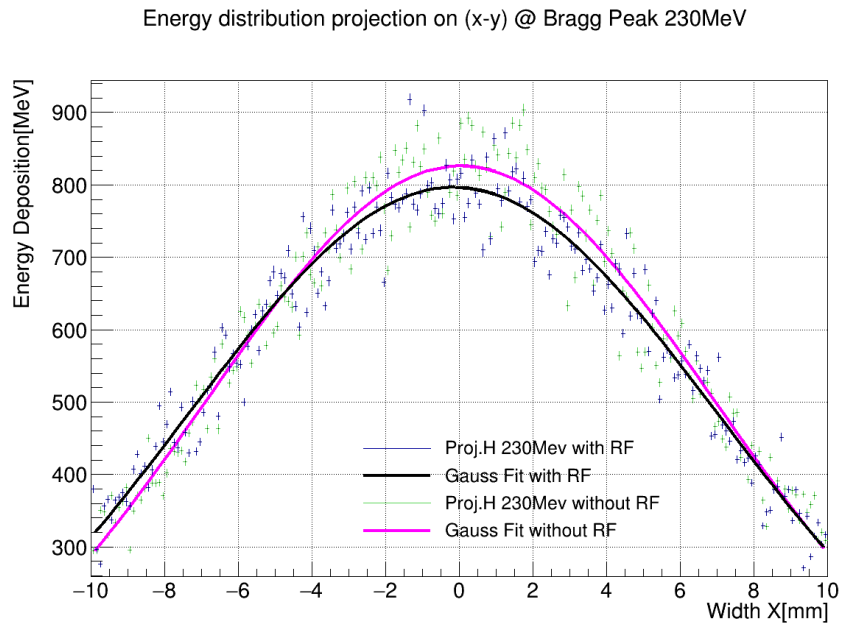


Figure 4.16: Projection at BP point for 230MeV proton beam, with and without RF

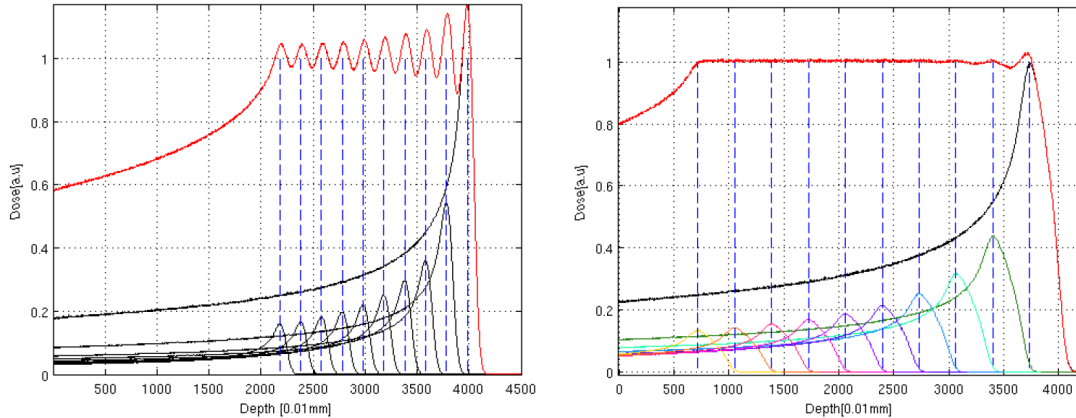


Figure 4.17: Scheme of a SOBP with (right) and without (left) Ripple Filter[3]

In the graphs above (Figures from (4.12) to (4.16)), the results of the comparison are reported, taking into account two different beam energy $70MeV$ and $230MeV$, both are representative values of the energy range used in proton therapy.

The effects of the ripple filter are more noticeable at low energy values, but increasing that parameter the differences between the two set-ups become more and more negligible.

In Fig.(4.17), the two possible SOBPs graphs are plotted, respectively with the RF and without, highlighting the irregularity on the profile in absence of the RF.

Even if this kind of simulation requires a fairly amount of CPU time, is a good way to help the design a component, evaluating directly the effects produced.

Obviously each device, after the design and simulation stage, must be validate by a direct test on the specific real accelerator, confirming or not the result obtained in the previous stage. In this case, the Ripple filter has already been verified at CNAO, and now in use in the dose delivery system. The validation outcomes are defined in the private report mentioned in the previous section.

Chapter 5

Discussion and Conclusions

The energy deposition of different types of hadrons was studied using a Monte Carlo method approach. From all the simulations performed, the behaviour of different kind of particles was characterized looking at their deposition profiles in a water phantom.

The graphs in Fig.(3.22) and Fig.(3.21) show a clear distinction between the characteristic deposition curve of light and heavy nuclei.

Concerning the light nuclei, helium and hydrogen show very similar profiles especially at high energy mainly due to their similar masses ($m_\alpha/m_p = 4$). It must be noted that the RF was used for both simulations, proving that this filter, designed specifically for protons, can be useful also for α particles.

For heavier ion beams, the RF effect is instead totally negligible; for nuclei with mass larger than $4u.m.$ the electrostatic interactions with water nuclei are predominant. The MCS events influence the hadron range: the particle path is much shorter than the hydrogen one, even if the energy per mass unit was setted at the same value.

For this reason, a rule can be extrapolated: nuclei, with an atomic mass larger than $4u.m.$, need much more specific energy ($E > 250[MeV/u.m.]$) than protons, in order to be applied in medical field. In hadrontherapy treatments the main goal is to use the penetrating power of a radiation to cure deeply seated tissues. An ion beam with more kinetic energy involves the adoption of a larger and more expensive accelerator in order to overcome the electrostatic barrier.

The carbon ions simulations have shown a the characteristic deposition very similar to the *Pristine Bragg curve*. According to Bourhaleb et al., the RF designed

for protons is not adequate for carbon ion transport, since it does not create any smoothing or widening on the profile.

With low specific energy values, the heavy ions are subject to the MCS in the entry region of the phantom, causing the change of their profile shape (Fig. (3.21)), losing the sharp fall-off after the BP.

The results of the simulations performed with the MC code were then used to produce two depth-dose databases with an energy step of 10MeV . The database production process is a long procedure and took $\approx 4 - 5h$ of elaboration per energy value. However this needs to be performed and validated only once for each set-up of the beam delivery line.

In real cases the *Look-Up tables* have a finer step than 10MeV , up to 1MeV , in order to reduce the interpolation error in the first assignment stage of a TPS. However the results obtained in this study are comparable with the already validated databases.

From the Look up tables, some useful information can be deduced: the 20MeV beam does not create any energy deposition in the water phantom for the complete apparatus since particles are completely absorbed in the RF. Then in the second table, the 20MeV deposition does not have the typical profile, but the dose is spreaded almost casually on the initial layers of the *Sensitive Detector*.

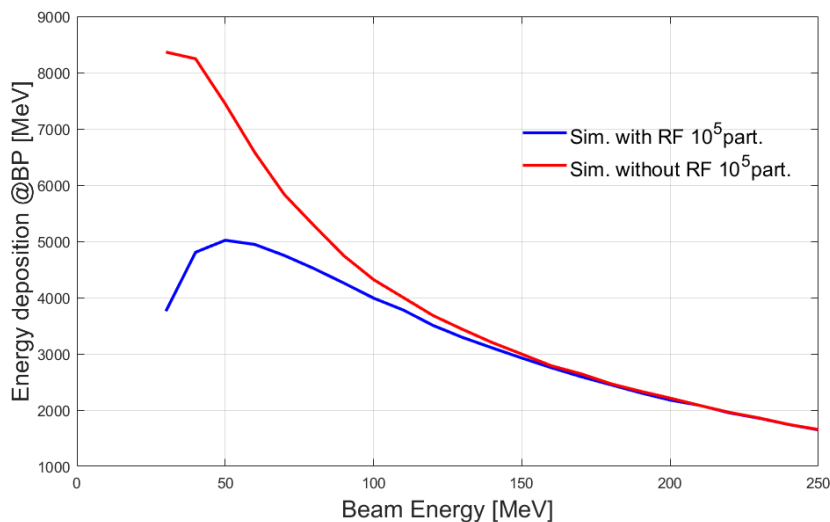


Figure 5.1: Bragg Peak energy deposition as function of the beam energy for both set-ups, with and without RF

Looking now at the next entries of the tables, the major inferable difference lies on the position of the Bragg peak point, which is backward shifted for the simulations with the RF. The backward shifting of the BP point is very small and almost constant on all the energy window considered, with a $\Delta Z_{BP} \approx 1.5mm$.

The graph in Fig.(5.1) reports the trend of the deposition at the BP point from $30MeV$ to $250MeV$ for the two configurations.

In Fig.(5.1), the effects of the scattering events in the range shifter are much more visible with low energy values than the highs. The main reason is that a low energy beam loses faster its kinetic content, since the interactions with the scatterer have a large impact on the height of the BP.

Instead, the analysing of the tail of the curves (in Fig.(5.1)) suggest that the presence of a RF is negligible at high energies. This result confirms that at high energies MCS cause almost no deviation to the beam. In this case the water phantom itself causes the spreading and the shifting of the BP, due to the large water thickness that a particle must go through.

After the 1D deposition analysis, the same conclusions can be retrieved from the 2D investigation on the orthogonal plane to the beam axis. In the graph in Fig.(5.2), the difference between the two σ_{xy} of the Gaussian fit (with and without the RF), is plotted.

Either in the orthogonal plane the ripple filter plays the major role only at low kinetic energy. The causes of this behaviour are the same for the 1D profile. (A visual reference can be found, looking at the projections of Figures (4.15 and 4.16))

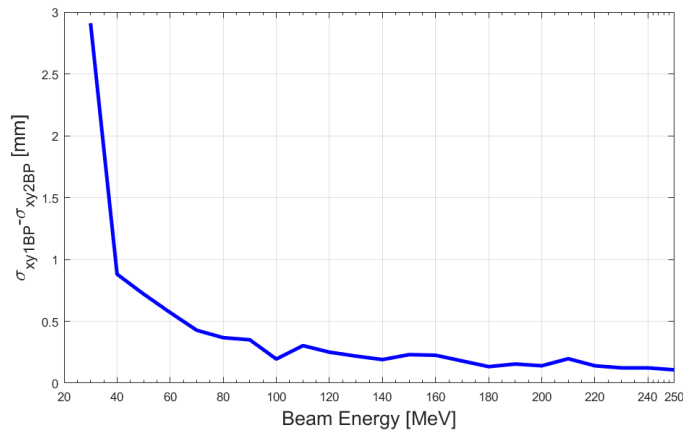


Figure 5.2: Difference ($\sigma_{xyBP1} - \sigma_{xyBP2}$) of the Gaussian fit as function of the beam energy

The *Ripple Filter* with high energy beams ($E > 180MeV$) does not produce any meaningful change or advantage, keeping almost unperturbed their deposition profiles.

An important problem during the application of a MC code is the evaluation of the uncertainties associated with the observed quantities.

In the various cases in analysis, the interested physical quantity was not only the dose released in certain point of the domain, but the whole dose distribution on the entire water phantom.

In the graph in Fig.(3.23), the relative error of the mean value of the distribution has been taken as reference, in order to highlight the proportionality with $N^{-1/2}$ (with N number of particles simulated). According to the convergence test, the deviation related to each value of the profile can be evaluated. Below in Figures (5.3), (5.4), (5.5), the error distributions, for three main examples, are shown. As well, a comparison between the deviation bands increasing the number of events is plotted.

The same behaviour of the error is present in all the simulations performed for both the databases. The error bars are not constant on the entire profile but, symmetrical respect to the mean value of the deposition in the point.

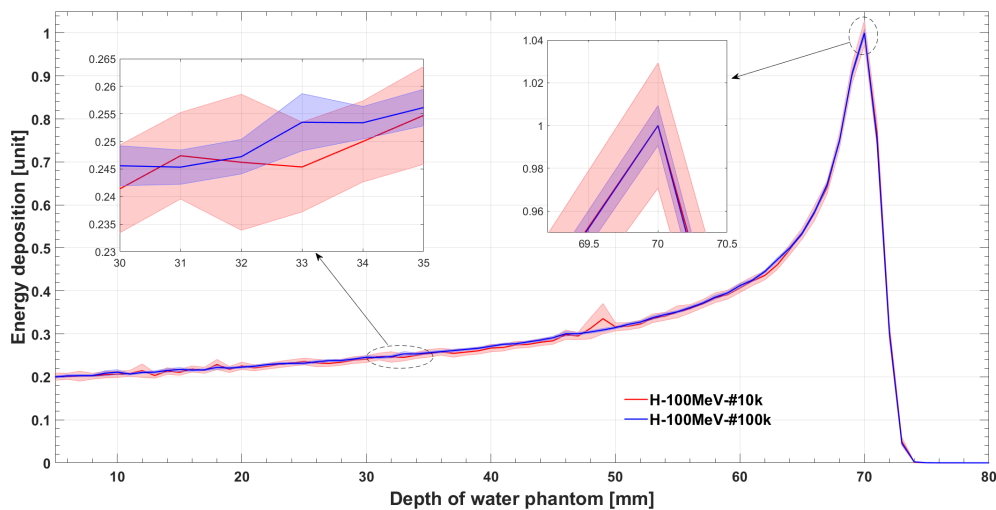


Figure 5.3: 1D dose distribution with doubled error-bars for 100MeV proton beam, for 10k and 100k particles

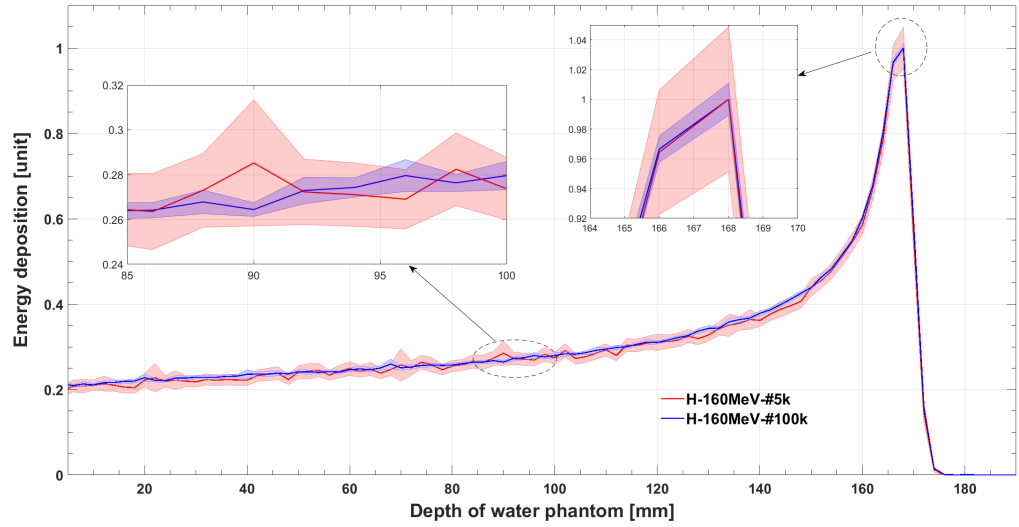


Figure 5.4: 1D dose distribution with doubled error-bars for 160 MeV proton beam, for 5k and 100k particles

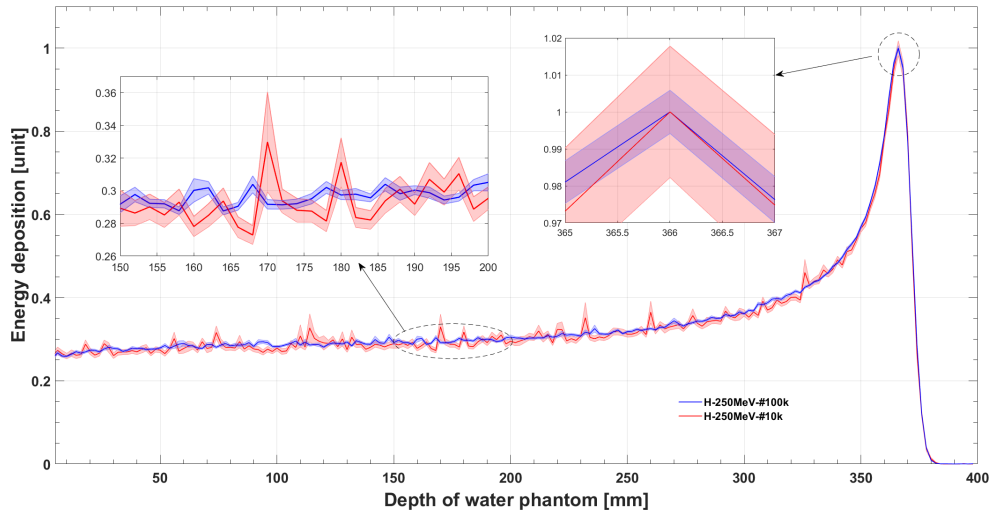


Figure 5.5: 1D dose distribution with doubled error-bars for 250 MeV proton beam, for 10k and 100k particles

The relative error is not constant along the z coordinate, and oscillates not regularly.

Comparing different runs with various iterations, it is possible to say that the amplitude of the oscillation is inversely proportional to the number of events.

In all the energies analysed, the relative error distribution is very similar. In the

plateau region (from the entry point to the rise of the BP) with 100k trials, the mean percentage error is below the $Err_{plateau} < 1.5\%$, (with only few peaks above $Err_{plateau} > 2,5\%$). In the neighbourhood of the Bragg peak, the oscillations become almost undetectable, keeping the error below $Err_{BP} < 1\%$. At last, in the fall off region the error increases to not consistent values. This behaviour is due to a very small *Signal-noise ratio-SNR*, because there is not any statical meaningful detection.

For example, the error, for a simulation at $160MeV$ with 1000 particles, becomes much higher with values $Err_{1k} \approx 5\%$. With the code DataGen-iSee, in order to reach an higher accuracy in a certain point, the only way is to increase the total number of particles simulated.

Any variance reduction method can not be adopted, like a survival biasing or other acceleration techniques. If hypothetically these procedures were adopted, they would cause loss of information on other points of the investigated domain. These techniques introduce a modification on the basic statistical principles of the problem, decreasing the variance in a point causes its increasing in the other regions.

The only limitation of using a complete MC approach from the characterization of the dose delivery system to the TPS, is the computational time. In the practical medical field only a limited time is available for a TPS definition, usually less than an hour and, for this reason the WET-system is commonly adopted.

By mean of the equivalent water system, the characterization of a set-up for the dose delivery system can be done only once in the life of the facility, saving time for each TPS performed.

On the other hand, the WET system introduces the interpolation error, and the approximation regarding the stopping power of the heterogeneous medium, taking only a mean value.

In order to reduce these approximations, the solution would be the application of a MC for each case studied, but the time needed should be decreased.

Speeding up the simulation process is a challenge. In order to apply directly a MC approach, from the beam line characterization to the treatment room, nowadays two possible ways are being studied:

- GPU-based Monte Carlo treatment planning.[20]
- Simplified Monte Carlo simulation-SMC.[22]

These methods approach the time problem from two different angles. The first

acts on a relatively new computational power, the GPU Graphic processor unit. Instead, the second one redefines the problem including some approximation.

The GPU is a computational system used for handling graphic information. It is designed for the direct elaboration of floating point number. Another advantage is the number of threads available in a GPU system; the combined processing power is able to overcome $1Tflpos$ (Flops=floating point operation per second). This speed is extremely larger than the usual clock frequency of a common CPU ($\approx 3GHz$). These machines use a very helpful computational philosophy, *single information-multiple data*. A GPU system can process data in parallel mode (in multi-threading mode).

A GPU-based simplified MC algorithm for TPS has been already tried, showing a calculation 12 times faster than CPU-based simplified algorithm. The disadvantage is the unavailability of cross section databases and physical models implemented in a compatible code language for these machines (e.g. CUDA).

Instead for the *Simplified Monte Carlo simulation*, the code is already available and Geant4 can be an example. By mean of this approach, the MC speed-up is not based on a different hardware performance, but on a lighter definition of the physics models involved in the transport phenomenon (and so on the physics packages used in the code).

In DataGen-iSee, no simplification has been used, because the code includes the complete physics packages of *G4Hadronics*, for elastic and inelastic interactions, together with the electromagnetic model. In few words, the electromagnetic model is very simple and it does not cause any waste of computational time. Practically it models one interaction type with only one cross section for all the energy spectrum. On the other hand, the hadronic physics model causes a very big computational effort. It includes every kind of nuclear elastic and inelastic interactions in the whole energy spectrum (their number is very large). On the contrary of the electromagnetic model, the hadronic one samples events from a very huge set of all possible interactions, even if the associated probability is almost negligible in the energy conditions of interest.

The proof of what just said can be found on the particle and neutron fluence graphs of Figures (4.7) and (4.8). These graphs highlight the production of secondary particles, caused by nuclear fragmentation reactions, and in general, by inelastic scattering. On a sample of 10^5 particles simulated, at high energy, the fraction of secondary fragments reaches about the 10% of the initial quantity. The same trends

is shown for the neutrons produced, with a peak of particles counted of about the 4% of the number of protons simulated.

Clearly the fragmentation phenomena have a probability to happen proportional to the energy of the incident particle, becoming considerable above 100MeV of kinetic energy.

This last examination confirms that using a simplified approach could lead to error in the estimation of the dose deposition, and the choice of the phenomena to be neglected must be taken carefully, especially for medical purpose.

The opinion of the author is that a full Monte Carlo code is the only way to obtain the accuracy requested for the applications in medical field, even if it requires a large amount of CPU time. Instead of simplifying the physics, the best solution would be a fast development of complete MC codes for GPU, decreasing the time needed but keeping the accuracy of the complete physics models.

The opinion just expressed is not based only on the error-problem, but it is founded either on the elasticity of a complete MC approach. This elaborate is the demonstration of the MC great versatility, where modifications on the detector, simulations with different particle species and energies, and even comparisons of the effects of a device are always possible changing only few code parameters.

This versatility, as well as the accuracy reachable are worth the high computational cost.

Unfortunately in nature rarely it is possible to see the adjectives "*fast and accurate*" together.

"Miracles are not allowed."

Appendix A

Superposition of dose distributions

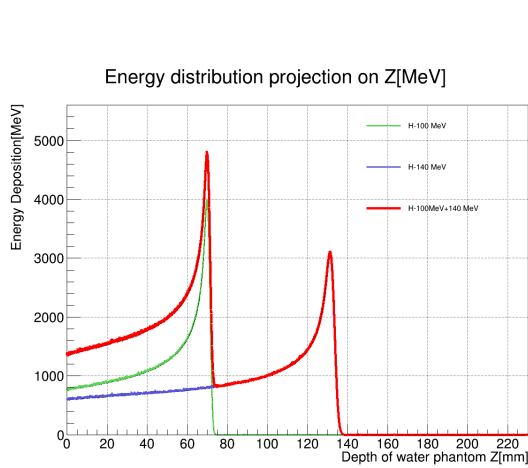


Figure A.1: 1D dose distribution for the superposition of proton beams at 100MeV and 140MeV

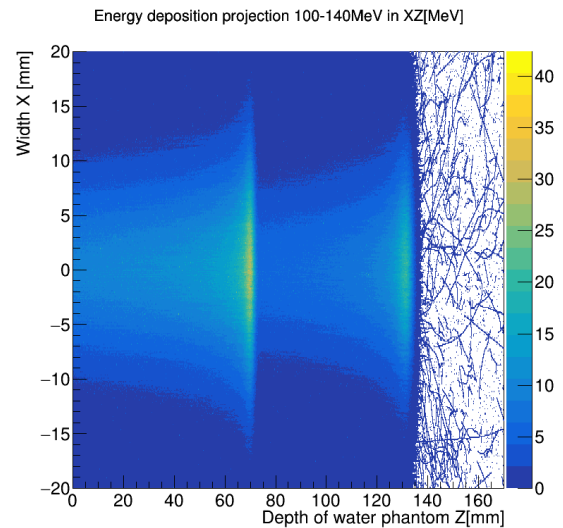


Figure A.2: 2D dose distribution for the superposition of proton beams at 100MeV and 140MeV

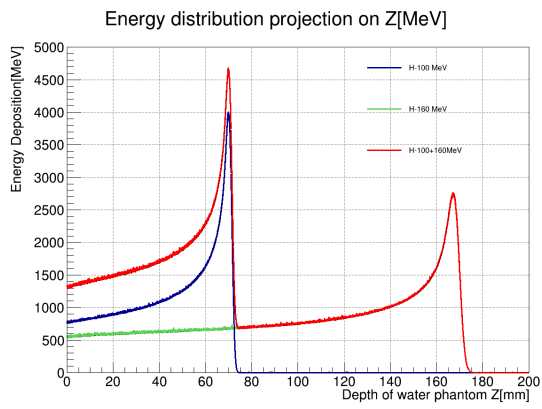


Figure A.3: 1D dose distribution for the superposition of proton beams at 100 MeV and 160 MeV

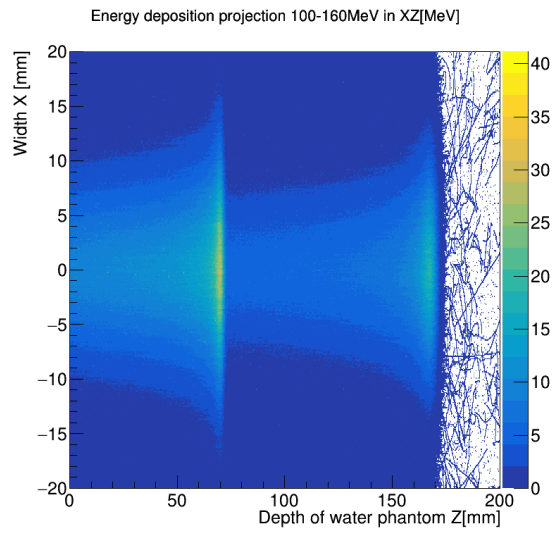


Figure A.4: 2D dose distribution for the superposition of proton beams at 100 MeV and 160 MeV

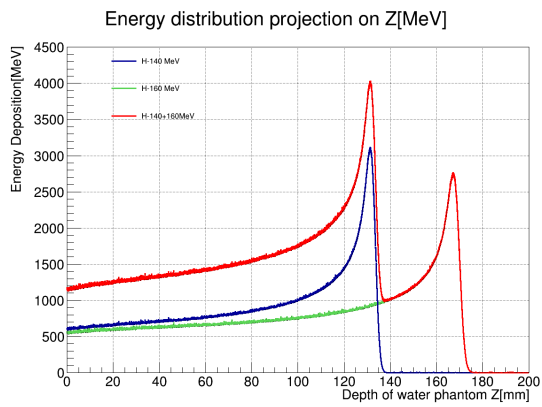


Figure A.5: 1D dose distribution for the superposition of proton beams at 140 MeV and 160 MeV

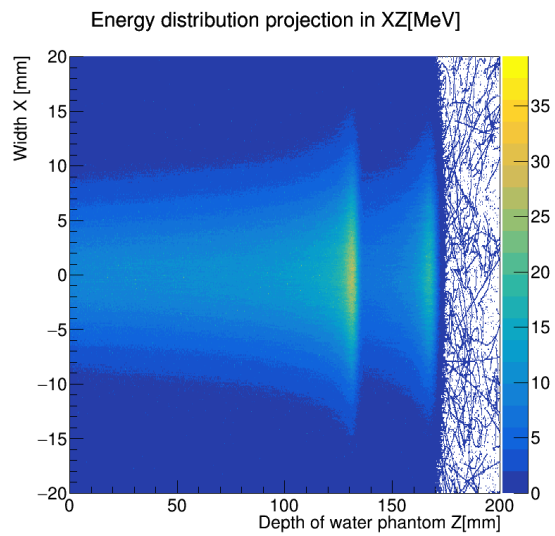


Figure A.6: 2D dose distribution for the superposition of proton beams at 140 MeV and 160 MeV

Appendix B

Fluence

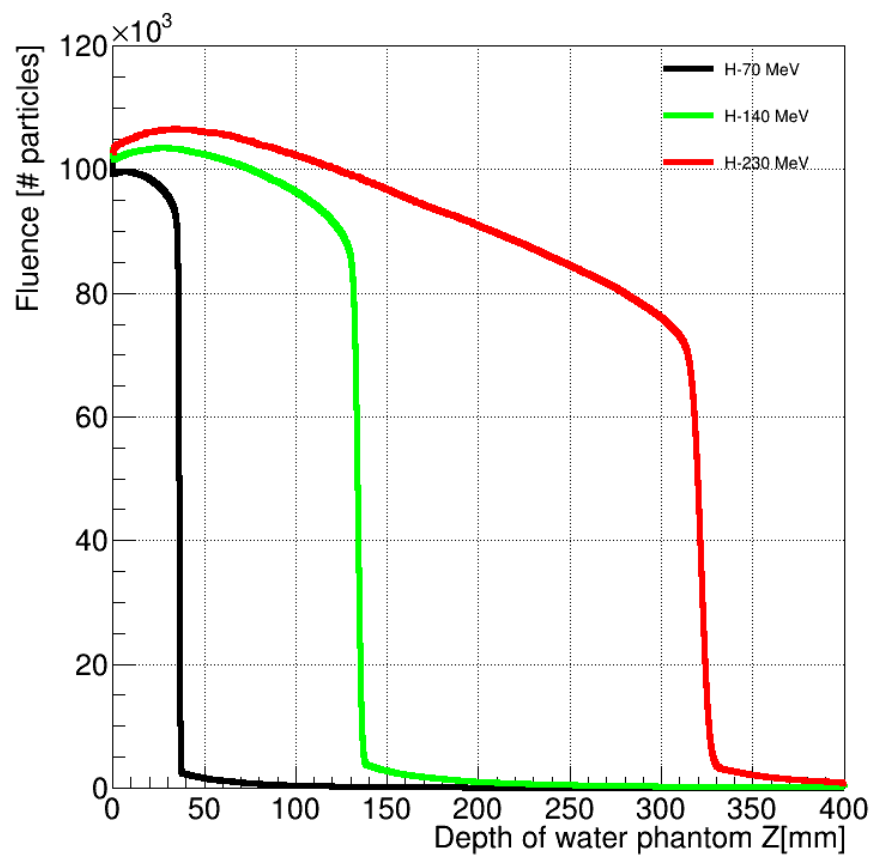


Figure B.1: Particle fluence for the database with no RF

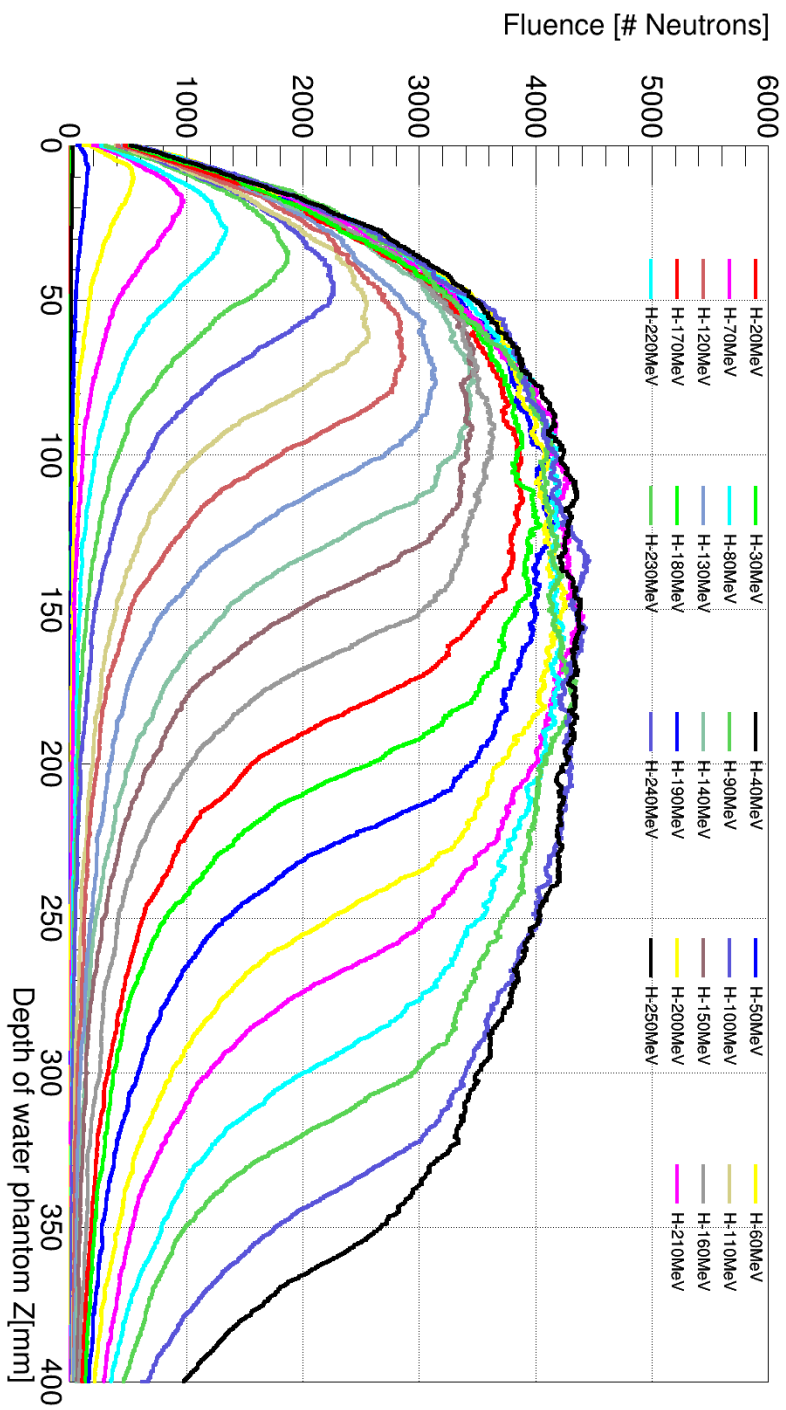


Figure B.2: Neutron fluence of all the simulations for the database with the Ripple Filter

Appendix C

Database with Ripple Filter

C.0.1 Profiles and projections for 70MeV proton beam

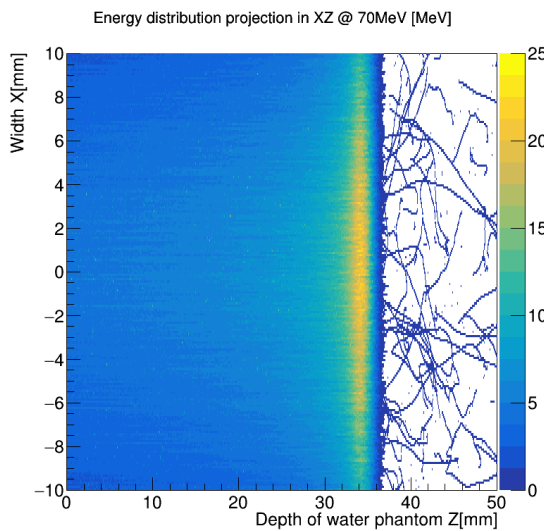


Figure C.1

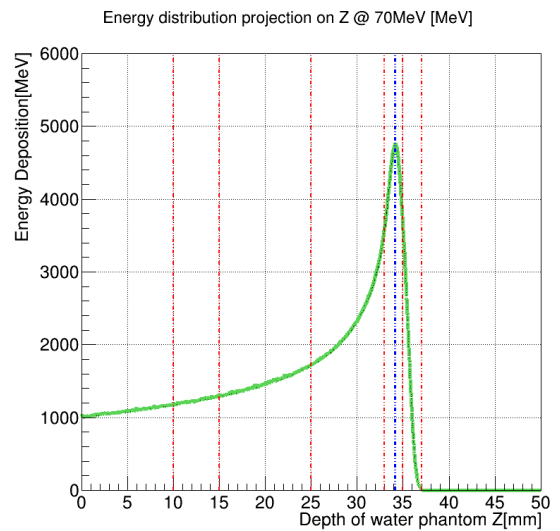


Figure C.2

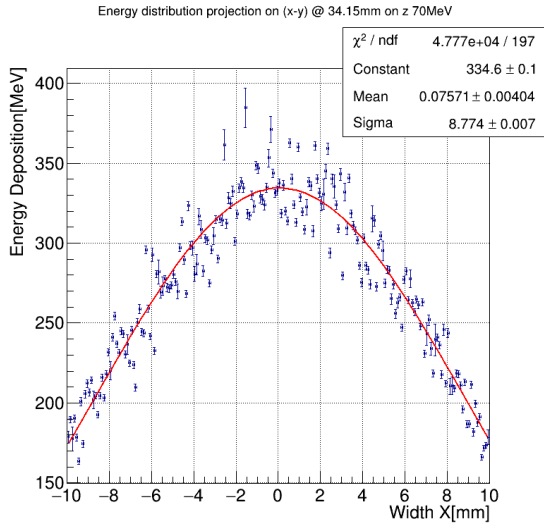


Figure C.3

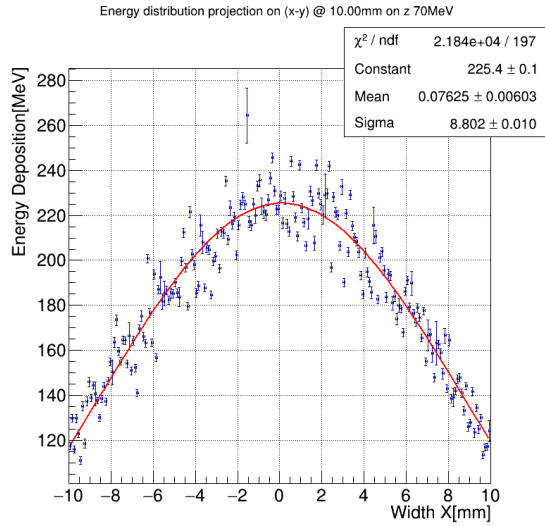


Figure C.4

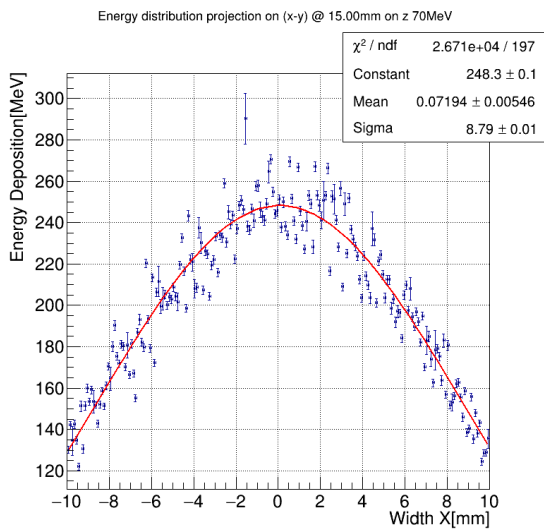


Figure C.5

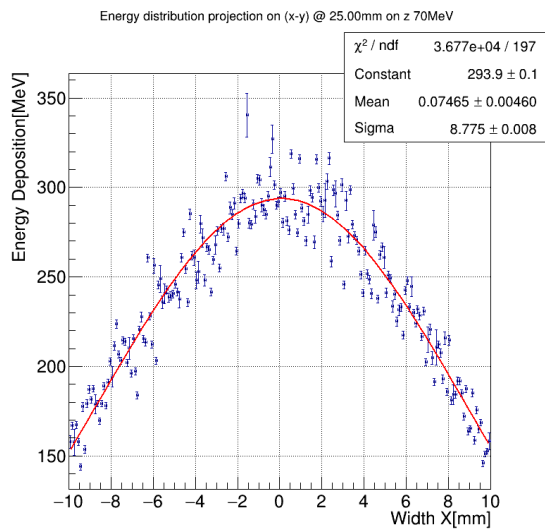


Figure C.6

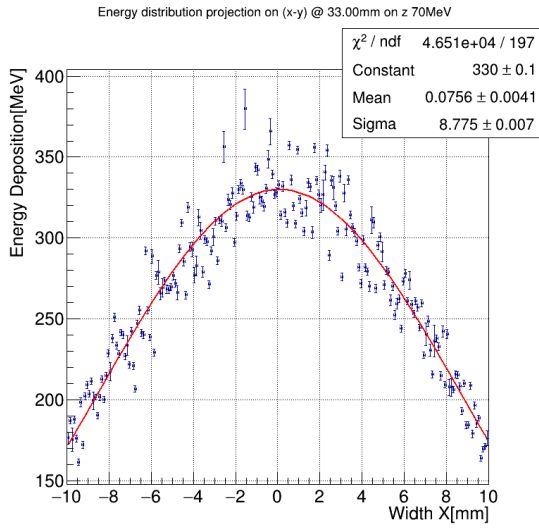


Figure C.7

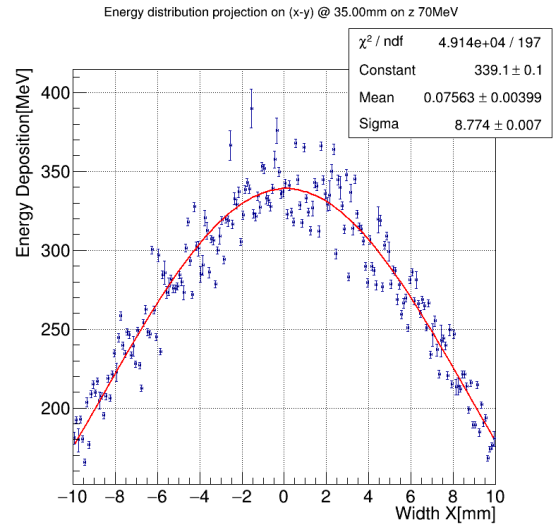


Figure C.8

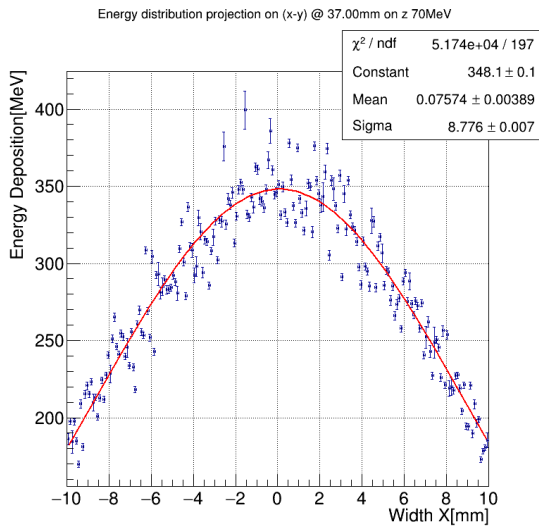


Figure C.9

C.0.2 Profiles and projections for 250MeV proton beam

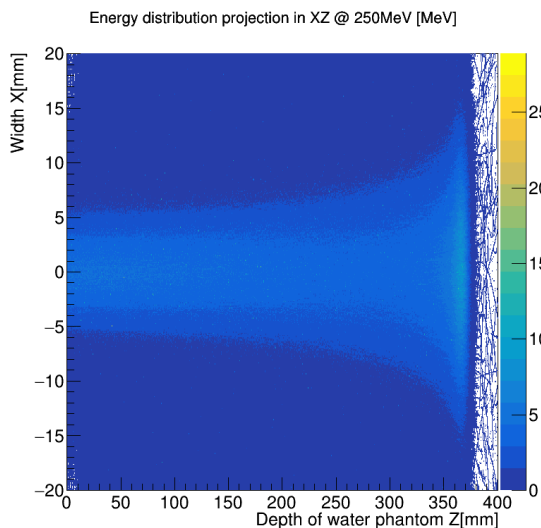


Figure C.10

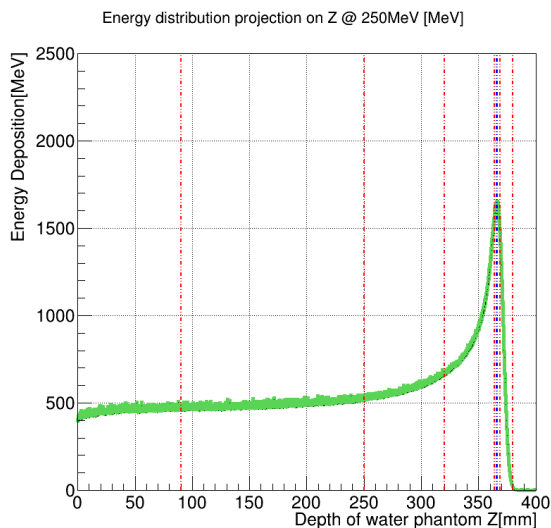


Figure C.11

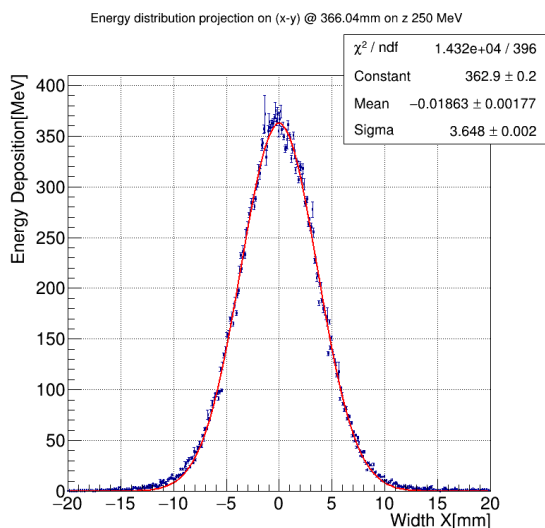


Figure C.12

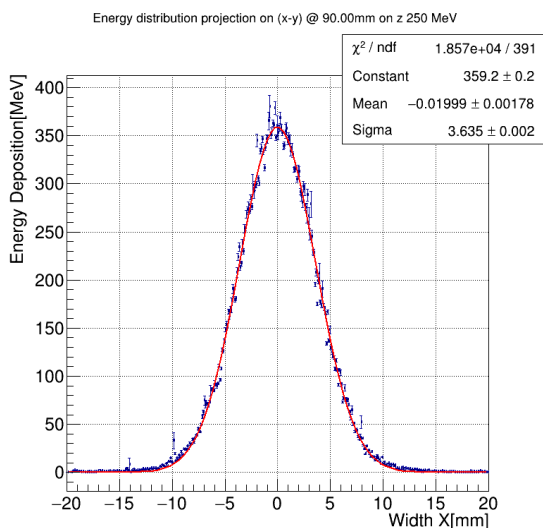


Figure C.13

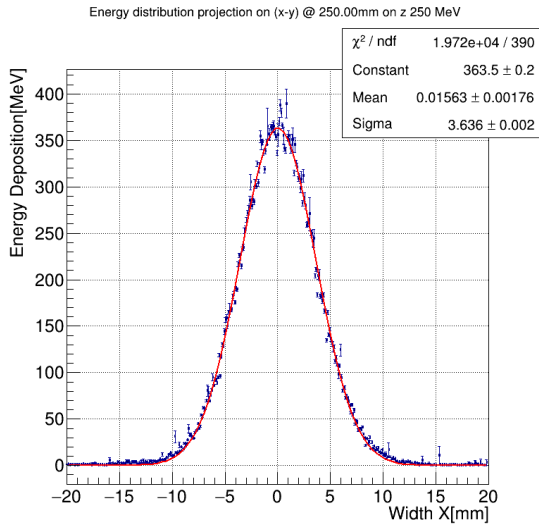


Figure C.14

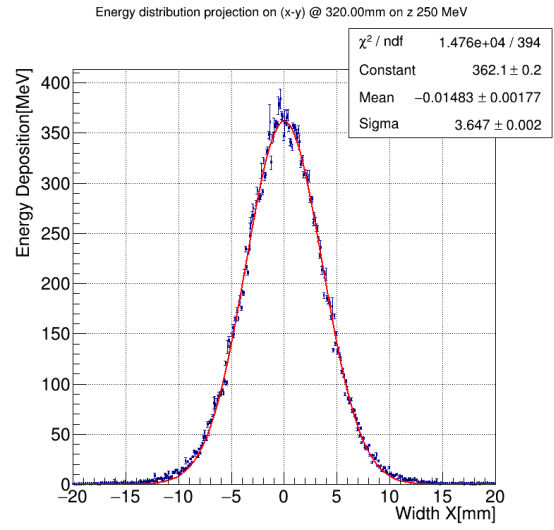


Figure C.15

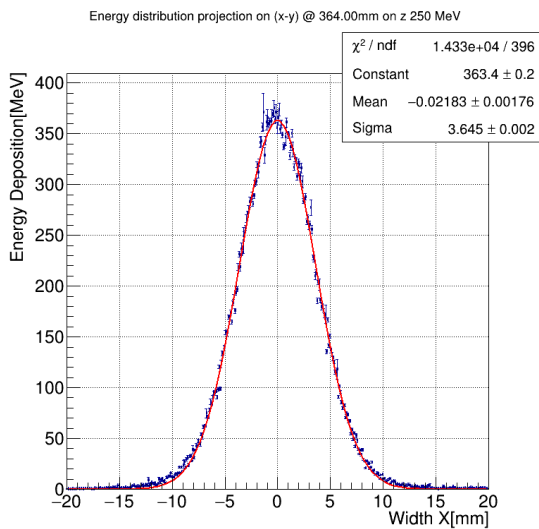


Figure C.16

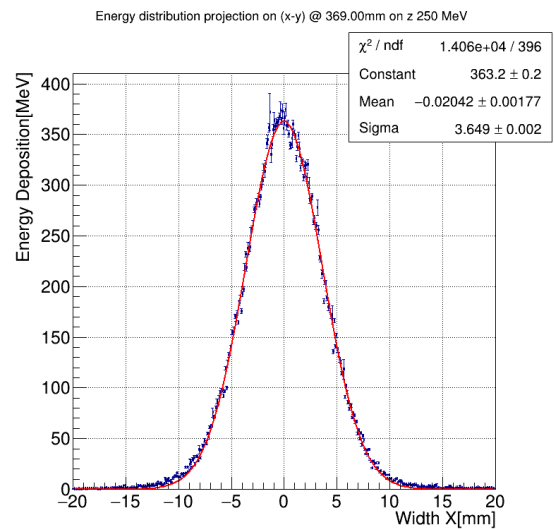


Figure C.17

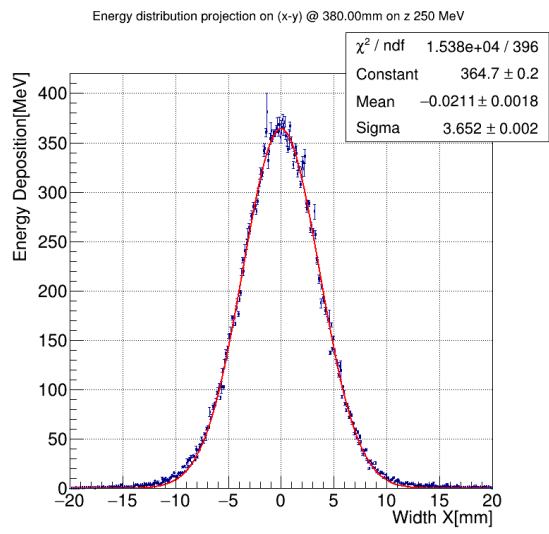


Figure C.18

Bibliography

- [1] S. Antoine et al. «Principle design of a protontherapy, rapid-cycling, variable energy spiral FFAG». In: *Nucl. Instrum. Methods Phys. Res., Sect. A* 602.2 (2009), pp. 293–305.
- [2] Wayne D Newhauser and Rui Zhang. «The physics of proton therapy». In: *Physics in Medicine & Biology* 60.8 (2015), R155.
- [3] Faiza Bourhaleb et al. «Monte Carlo Simulations for Beam Delivery Line Design in Radiation Therapy with Heavy Ion Beams». In: *Applications of Monte Carlo Methods in Biology, Medicine and Other Fields of Science*. InTech, 2011.
- [4] David J Brenner. «The linear-quadratic model is an appropriate methodology for determining isoeffective doses at large doses per fraction». In: *Seminars in radiation oncology*. Vol. 18. 4. Elsevier. 2008, pp. 234–239.
- [5] Rene Brun and Fons Rademakers. «ROOT—an object oriented data analysis framework». In: *Nuclear Instruments and Methods in Physics Research Section A: Accelerators, Spectrometers, Detectors and Associated Equipment* 389.1-2 (1997), pp. 81–86.
- [6] W Ralph Nelson et al. *The EGS4 code system*. Tech. rep. 1985.
- [7] *Lecture notes of the course on Biomedical and industrial application of radiation, Politecnico di Torino*.
- [8] Meng Xu-Welliver et al. «Imaging across the life span: Innovations in imaging and therapy for gynecologic cancer». In: *Radiographics* 34.4 (2014), pp. 1062–1081.
- [9] Boris Davison and John Bradbury Sykes. «Neutron transport theory». In: (1957).
- [10] Omar Desouky et al. «Targeted and non-targeted effects of ionizing radiation». In: *J. Radiat. Res. Appl. Sci.* 8.2 (2015), pp. 247–254.

-
- [11] James J Duderstadt and Louis J Hamilton. *Nuclear reactor analysis*. Vol. 1. Wiley New York, 1976.
- [12] D.P. Fontenla. *Forward Planning*. IAEA Collection. 2008.
- [13] GEANT Collaboration et al. «Physics reference manual». In: *Version: geant4* 10.9 (2016).
- [14] Geant Collaboration. «Introduction to Geant4». In: (2010).
- [15] Serena Gianfaldoni et al. «An Overview on Radiotherapy: From Its History to Its Current Applications in Dermatology». In: *Open access Macedonian journal of medical sciences* 5.4 (2017), p. 521.
- [16] Kent A Gifford et al. «Comparison of a finite-element multigroup discrete-ordinates code with Monte Carlo for radiotherapy calculations». In: *Physics in Medicine & Biology* 51.9 (2006), p. 2253.
- [17] Kang Jin Oh Park Seo Hyun. «Basics of particle therapy I: physics». In: *Radiat Oncol J* 29.3 (2011), pp. 135–146.
- [18] INFN Catania LNS. *V international Geant4 School*. Course. Oct. 2017.
- [19] IAEA. *Radiation Oncology Physics*. Vienna: International Atomic Energy Agency, 2005.
- [20] Xun Jia et al. «GPU-based fast Monte Carlo dose calculation for proton therapy». In: *Physics in Medicine & Biology* 57.23 (2012), p. 7783.
- [21] Elizabeth Koehler et al. «On the assessment of Monte Carlo error in simulation-based statistical analyses». In: *The American Statistician* 63.2 (2009), pp. 155–162.
- [22] R Kohno et al. «Clinical implementation of a GPU-based simplified Monte Carlo method for a treatment planning system of proton beam therapy». In: *Physics in Medicine & Biology* 56.22 (2011), N287.
- [23] Ken Ledingham et al. «Towards Laser Driven Hadron Cancer Radiotherapy: A Review of Progress». In: *Applied Sciences* 4.3 (2014), pp. 402–443.
- [24] CH Lin et al. «Beam profile monitoring system for proton therapy and Monte Carlo modeling of proton beam lateral development in water in 100–400MeV». In: *Nuclear Science Symposium and Medical Imaging Conference (NSS/MIC), 2012 IEEE*. IEEE. 2012, pp. 1268–1271.

- [25] Peter Linstrom. *NIST Chemistry WebBook, NIST Standard Reference Database 69*. eng. 1997.
- [26] Arabinda Kumar Rath and Narayan Sahoo. *Particle Radiotherapy: Emerging Technology for Treatment of Cancer*. Springer, 2016.
- [27] Omar Desouky and Guangming Zhou. «Biophysical and Radiobiological Aspects of Heavy Charged Particles». In: 10 (Apr. 2015).
- [28] Brita Singer Sorensen Jan Alsner. *Particle Radiobiology*. website. Website of Aarhus University Hospital. May 2017.
- [29] Patrícia Rebello and Mahir S Hussein. «Nuclear fragmentation in protontherapy». In: *Braz. J. Phys.* 34.3A (2004), pp. 942–943.
- [30] Adele Rimoldi et al. «Geant4 studies of the CNAO facility system for hadrontherapy treatment of uveal melanomas». In: *Journal of Physics: Conference Series*. Vol. 513. 2. IOP Publishing. 2014, p. 022028.
- [31] Marco Schwarz. «Treatment planning in proton therapy». In: *The European Physical Journal Plus* 126.7 (2011), p. 67.
- [32] Júlio Nepomuceno. «Antioxidants in Cancer Treatment». In: Dec. 2011.
- [33] Oleg Vassiliev. *Monte Carlo Methods for Radiation Transport*. Jan. 2017.
- [34] Wikimedia Commons. *File:Dose Depth Curves.svg* — *Wikimedia Commons, the free media repository*. [Online; accessed 6-June-2018]. 2017.